NANOSTRUCTURED MATERIALS FOR
BIOLOGICAL IMAGING AND CHEMICAL SENSING

A DISSERTATION SUBMITTED TO
MATERIALS SCIENCE AND NANOTECHNOLOGY PROGRAM
OF THE GRADUATE SCHOOL OF ENGINEERING AND SCIENCE
OF BILKENT UNIVERSITY
IN PARTIAL FULFILLMENT OF THE REQUIREMENTS
FOR THE DEGREE OF
DOCTOR OF PHILOSOPHY

By
Adem Yildirim
November, 2014

I certify that I have read this thesis and that in my opinion it is fully adequate, in scope and in quality, as a thesis of the degree of Doctor of Philosophy.

……………………………….

Prof. Dr. Mehmet Bayındır (Advisor)

I certify that I have read this thesis and that in my opinion it is fully adequate, in scope and in quality, as a thesis of the degree of Doctor of Philosophy.

……………………………….

Assoc. Prof. Dr. Hatice Duran

I certify that I have read this thesis and that in my opinion it is fully adequate, in scope and in quality, as a thesis of the degree of Doctor of Philosophy.

……………………………….

Assist. Prof. Dr. Ali Kemal Okyay

I certify that I have read this thesis and that in my opinion it is fully adequate, in scope and in quality, as a thesis of the degree of Doctor of Philosophy.

……………………………….

Prof. Dr. Adil Denizli

I certify that I have read this thesis and that in my opinion it is fully adequate, in scope and in quality, as a thesis of the degree of Doctor of Philosophy.

……………………………….

Assist. Prof. Dr. Bora Garipcan

Approved for the Graduate School of Engineering and Science:

……………………………….

Prof. Dr. Levent Onural

Director of the Graduate School of Engineering and Science

ABSTRACT

NANOSTRUCTURED MATERIALS FOR BIOLOGICAL IMAGING AND CHEMICAL SENSING

Adem Yildirim

Ph.D. in Materials Science and Nanotechnology

Supervisor: Prof. Dr. Mehmet Bayındır

November, 2014

In the recent years, the design and synthesis of fluorescent nanoparticles for biological and chemical sensing applications have received considerable attention due to the excellent photostability and emission intensity of fluorescent nanoparticles and the intrinsic sensitivity of fluorescence based methods. Although considerable progress has been made in their synthesis, there is still need for low-cost and high throughput methods for their widespread utilization in biological and chemical sensing applications. In addition, studies regarding their biocompatibility are necessary to identify the toxicological potential of these nanomaterials.

In this context, this thesis seeks new methods for multifunctional fluorescent nanoparticle synthesis and investigates their interactions with living organisms. In addition, it reports the applications of the fluorescent nanomaterials in biological imaging, therapy and chemical sensing applications.

First, we report a self-assembly method to prepare PEGylated or peptide functionalized mesoporous silica nanoparticles (MSNs) for cell labeling and drug delivery applications. The good cyto- and blood- compatibility of the functionalized nanoparticles were demonstrated. Next, we demonstrated a surfactant assisted method to synthesize ultrabright silica nanoparticles and studied their *in vitro*

cytocompatibility with several cell lines. We demonstrated the applications of ultrabright particles in cell labeling, chemo and photodynamic therapy and trace explosive sensing. Then, we discuss a template-free method (porosity difference based selective dissolution strategy) to prepare self-luminescent mesoporous hollow silica nanoparticles with tailored shapes. In addition, we studied the surface effects on blood compatibility of nanoparticles in detail using the MSNs possessing different surface functional groups (ionic, polar, neutral, and hydrophobic). Finally, we investigated the optical properties of polydopamine nanoparticles and showed that fluorescence of as-prepared polydopamine nanoparticles can be used for sensitive and selective detection of the dopamine neurotransmitter.

ÖZET

BİYOLOJİK GÖRÜNTÜLEME VE KİMYASAL SENSÖR UYGULAMALARI İÇİN NANOYAPILI MALZEMELERİN GELİŞTİRİLMESİ

Adem Yildirim

Malzeme Bilimi ve Nanoteknoloji, Doktora

Tez Yöneticisi: Prof. Dr. Mehmet Bayındır

Kasım, 2014

Son yıllarda, biyolojik görüntüleme ve kimyasal sensör uygulamalarında kullanılmak üzere floresan nanopartiküllerin sentezi, floresans yöntemlerin yüksek hassasiyetlerinden ve floresan nanopartiküllerin mükemmel fotokararlılık ve ışıma şiddetlerinden dolayı oldukça fazla ilgi çekmektedir. Bu partiküllerin sentezi konusunda bugüne kadar ciddi ilerlemeler gerçekleştirilmiş olsada, floresan nanopartiküllerin geniş uygulama alanları bulmaları için ucuz ve yüksek verimli yöntemlerin geliştirilmesine ihtiyaç vardır. Buna ek olarak, floresan nanopartiküllerin toksik potansiyellerin ayrıntılı olarak incelenmesi, bu partiküllerin kullanılmasından doğabilecek istenilmeyen etkilerin önüne geçilmesi açısından oldukça önemlidir.

Bu tez, asıl olarak çok fonksiyonlu floresans nanopartiküllerin sentezi için yeni ve basit yöntemlerin geliştirilmesi ve üretilen nanopartiküllerin biyolojik organizmalar ile uyumluluğunun araştırılması üzerine yoğunlaşmaktadır. Ayrıca, üretilen nanopartiküllerin biyolojik görüntüleme, terapi ve kimyasal teşhisi alanlarındaki uygulamalarıda rapor edilmektedir.

İlk olarak, kendiliğinden bir araya gelme yöntemi kullanılarak, polietilenglikol (PEG) veya kısa dizili peptitler ile fonksiyonalize edilmiş mezoboşluklu silika nanopartiküller (MSN) hücre işaretleme ve kontrollü ilaç salımı uygulamalarında kullanılmak üzere sentezlenmiştir. Hazırlanan partiküllerin hücre ve kan uyumlulukları gösterilmiştir. Daha sonra, yüzey arttırıcı moleküllerin yarıdımı ile

oldukça parlak silika nanopartiküllerin hazırlanması ve bu nanopartiküllerin değişik hücre çeşitleri ile olan uyumluluğu gösterilmiştir. Nanopartiküllerin hücre işaretleme, kemo- ve fotodinamik- terapi ve patlayıcı tespiti uygulamaları rapor edilmiştir. Bunlara ek olarak, nanopartiküllerin yüzey kimyasının nanopartiküllerin kan bileşenleri ile uyumluğu üzerine etkisi yüzeyleri değişik özelliklere sahip (iyonik, polar, nötür ve hidrofobik) fonksiyonel gruplarla modifiye edilmiş MSN' ler kullanılarak ayrıntılı olarak incelenmiştir. Son olarak, polidopamin nanopartiküllerin optik özellikleri incelenmiş ve yeni hazırlanmış polidopamin nanopartiküllerin floresan özellikte olduğu gösterilmiştir. Floresan polidopamin nanopartikül oluşumu, dopamine nörotransmitterinin hassas ve seçici bir şekilde tespit edilmesinde kullanılmıştır.

Acknowledgement

First and foremost, I would like to thank my advisor Prof. Mehmet Bayındır for his continuous guidance throughout my PhD. He always encouraged and supported me with the research projects. The seven years in Bayındır group was a great experience and will always be remembered.

I would like to thank Prof. Mecit Yaman who always encouraged me with my PhD and future career. We spent a lot of time with him by writing manuscripts, discussing about almost everything and planning about the future projects. I have learned a lot from him during these times.

I owe my sincere thanks to Prof. Bora Garipcan who I know since from my undergraduate years in Hacettepe University. He generously allowed me to use his cell culture facilities in Boğaziçi University where I gained an indispensable experience. I would like to thank Müge Türkaydın and other Garipcan group members for their support and friendship during my visits to Boğaziçi University.

Also, I would like to thank the people who contributed to this thesis; Prof. Mustafa Ö. Güler, Prof. Ayşe B. Tekinay, Prof. Turgay Tekinay, Prof. Gökçen Birlik Demirel, Prof. Adil Denizli, Prof. Hatice Duran, Prof. Ali Kemal Okyay, Erol Özgür, Pınar Beyazkılıç, Melis Şardan, Didem Mumcuoğlu, Rengin Erdem, Berna Şentürk. Without their helps this thesis would be incomplete.

I would like to thank all present and past members of Bayındır group and the friends in UNAM. It will be a long list if I thank all of them one by one, but I would like to thank some of them particularly. To Hulya, my first colleague and a valuable friend, with her we failed and succeed a lot. To the best colleague and loyal friend, Mert. To Erol for his valuable friendship and cheerful songs. To my best friends; Öner, Melis and Bihter. To my teammates and friends, Pınar, Emre, Urnaa and Yunusa; it is always fun to work with them. Also, I would like to thank all the staff and engineers of UNAM, especially Mustafa Güler, for their support and helps.

I would like to express my gratitude to The Scientific and Technological Research Council of Turkey, TÜBİTAK, for the Ph.D. Scholarship.

Contents

List of Figures

List of Tables

Chapter 1

Introduction

The design and synthesis of fluorescent nanoparticles is a rapidly growing research field and is promising for applications ranging from molecular and cellular bioimaging to chemical sensing of various molecules [1-3]. The most common method for the preparation of fluorescent nanoparticles is conjugating the fluorescent molecules with nanoparticles. In this context, various nanoparticles produced from a wide range of materials have been employed; silica, iron oxide, gold, silver, carbon, metal oxides, polymers and so on [4]. Conjugation of fluorescent materials into nanoparticles offers many advantages over their direct use, such as improved photostability, emission intensity and solubility in water [5]. Beside from conjugation method, another way to prepare fluorescent nanoparticles is to use intrinsically fluorescent materials in nanoparticle synthesis, such as conjugated polymers, quantum dots, metal nanoclusters *etc*. [6-8].

Additional features can be provided to the fluorescent nanoparticles using different material compositions. For instance, fluorescent mesoporous silica nanoparticles (MSNs) can be used for controlled delivery of drugs into the cells -owing to their high surface area and pore volume- and at the same time for imaging of the position of nanoparticles inside the cells. Another well-known example is the superparamagnetic iron oxide nanoparticle containing core/shell fluorescent nanoparticles, which can be used for dual fluorescent and magnetic imaging of tumors. Furthermore, such multifunctional fluorescent nanoparticles can be targeted to cancer cells by modifying

their surfaces with the molecules that are specific to the overexpressed receptors of cancer cells (*e. g.* antibodies, folic acid, and peptide sequences) in order to improve the efficiency of nanoparticle based therapies. In the last two decades, we witnessed many successful demonstrations of such multifunctional fluorescent nanoparticles in especially the field of biotechnology. More detailed information on this subject can be found in the previous reviews [9-11].

In this thesis, we focused on the design and synthesis of novel multifunctional fluorescent nanoparticles for bioimaging and chemical sensing applications. We also demonstrated the promising potential of the prepared materials in the chemo- and photodynamic- therapy of cancer and in drug delivery applications. In addition, we studied their biocompatibility in terms of cytotoxicity, hemolytic activity, non-specific protein adsorption, dispersibility in biological media and their blood coagulation initiation/inhibition ability.

This thesis is organized in eight chapters. Chapter 1 gives the motivation of this thesis and its organization. Chapter 2-7 reports the published or to be published outcomes of this thesis. Chapter 8 gives the general conclusions.

In Chapter 2, we describe a facile self-assembly method to prepare PEGylated or peptide functionalized fluorescent silica nanoagents using hydrophobic mesoporous silica nanoparticles and an amphiphilic PEG containing polymer or peptide amphiphiles. We used them for cellular labeling. In addition, we showed the excellent dispersibility in biological media, good cyto- and blood compatibilities and improved cellular uptake of these surface engineered fluorescent nanoparticles.

In Chapter 3, we report the synthesis of silica capped ultrabright MSNs with reduced cytotoxicity. We prepared the ultrabright MSNs by surfactant assisted encapsulation of Rose Bengal dye inside the pores of MSNs. Pores of the dye doped MSNs were capped with a dense silica layer to reduce the dye and surfactant leakage. We studied their optical properties in detail and demonstrated the cell-labeling applications of these particles. In addition, synergetic chemo- and photodynamic-therapy of cancer cells with ultrabright MSNs was showed. Furthermore, the compatibility of the particles with red blood cells were studied.

In Chapter 4, we describe the preparation of pyrene confined MSNs for the trace detection of trinitrotoluene (TNT) in aqueous phase. Pyrene confined MSNs were prepared using the surfactant assisted encapsulation method described in the previous chapter. We demonstrated that bright pyrene excimer emission of the particles exhibit a rapid, sensitive and visual quenching response against TNT.

In Chapter 5, we explain a templateless method to prepare self-luminescent hollow MSNs with tailored morphology. The method is based on the selective dissolution of porous cores of solid silica shell/mesoporous silica core nanoparticles in mild conditions (PBS or water). Using this method we prepared hollow and mesoporous silica nanospheres and nanorods with different shell thicknesses. Also, we described a general method to prepare self-luminescent hollow particles. In addition, we proposed a mechanism for selective dissolution of porous cores of the core/shell nanoparticles.

In Chapter 6, we systematically evaluate the impacts of surface chemistry on blood compatibility of MSNs. We investigated the interactions of a series of MSNs possessing different surface functional groups (ionic, polar and hydrophobic) with blood constituents, in terms of their hemolytic activity, thrombogenicity, and adsorption of blood proteins on their surfaces. Also, we prepared Rhodamine B dye conjugated fluorescent MSNs to observe the effect on fluorescent tagging on blood compatibility.

In Chapter 7, we propose a turn-on fluorescent method for rapid and facile detection of dopamine, which is the principle biomarker for diseases such as schizophrenia, Huntington's, and Parkinson's. The method is based on *in situ* formation of fluorescent polydopamine nanoparticles (demonstrated for the first time in this study) under basic conditions. We studied the *in situ* optical properties of polydopamine nanoparticles, in order to determine optimum experimental conditions. Under optimized conditions, we demonstrated the high sensitivity (40 nM) and excellent selectivity of the assay.

Finally, in Chapter 8, we give the general conclusions and major outcomes of this thesis and the potential future applications.

Chapter 2

A Facile Self-Assembly Method to Functionalize MSNs with PEG and Peptides

2.1 Introduction

The high surface area and pore volume, good chemical stability and ease of surface functionalization of mesoporous silica nanoparticles (MSNs) make them promising materials for biological applications as bioimaging, cell labeling and drug delivery agents [12, 13]. In addition, silica based materials are generally accepted as biocompatible materials by the U.S. Food and Drug Administration (FDA). However, recent studies demonstrated their potential *in vitro* and *in vivo* toxicity, especially when their size is reduced to the nano scale [14, 15]. Although the toxicity of silica based nanomaterials depends on several factors including particle size, shape, surface chemistry and porosity [16-18] there is a general consensus that chemical structure of the surface is the predominant factor which determines the interactions with biological systems [19]. The surface of bare silica is covered with negatively charged silanol groups, which can electrostatically interact with positively charged tetraalkyl ammonium moieties of the cell membrane and can lead to cytotoxicity by membranolysis or inhibition of cellular respiration [19, 20]. Also, rapid aggregation of silica based nanoparticles in biological media can result in mechanical obstruction in the capillary vessels of several vital organs, leading to organ failure and even death

[21, 22]. Therefore, replacing the surface silanol groups with biocompatible molecules is essential to improve the biocompatibility of MSNs.

Among numerous polymeric or organosilane surface modification ligands, polyethylene glycol (PEG) is the mostly used one due to its well established biocompatibility, hydrophilicity, and antifouling properties [23]. However, the PEGylation process has some limitations; (i) it mostly requires tedious organic synthesis and surface modification [24] and (ii) pores of MSNs may be closed by the long PEG polymer chains, which can hinder the drug loading process. Beside from biocompatibility, surface modification of MSNs is important in terms of improving the efficiency of MSN based therapies. Modification of the MSN surface with polymers [25, 26] (*e.g.* polyethyleneimine and zwitterionic copolymers) or biomolecules [27-29] (*e.g.* folic acid, antibodies, peptides) has been proved to be an effective way to improve the selective uptake of MSNs by cancer cells which is highly desired for cancer diagnosis and therapy applications. In particular, short peptide chains have attracted a great deal of attention in recent years because of their tunable functionality, biodegradability, and relative ease of synthesis [30-32]. It has been shown that short peptide sequences (*e.g.* RGD and IL-13) can be used for targeting nanoparticles to specific cancer cell lines [33-36]. In addition to targeting properties, some peptide sequences (*e.g.* TAT peptide) demonstrated cell penetrating and endosomal escape properties [37, 38]. Also, the biodegradability of peptides makes them suitable for being utilized as stimuli responsive gatekeepers in controlled drug release [39] and linkers in FRET based diagnostics [40, 41]. Conventionally, peptides are covalently attached to the silica surface by using additional cross-linking reagents and troublesome synthetic methods, which results in poor surface grafting density and costly synthesis of functionalized materials [34, 39, 42].

To overcome these limitations in both PEGylation and peptide modification, here we report a facile self-assembly method using octyl modified hydrophobic MSNs (OMSNs) with pluronic polymers (for PEGylation) of peptide amphiphiles (PAs) (for peptide modification). Pluronic F127, a FDA approved biocompatible polymer, contains two hydrophilic PEG blocks and a hydrophobic polypropylene oxide (PPO) between the two PEG blocks was used for PEGylation [43]. When the powder of hydrophobic MSNs is added into the F127 solution they are easily transferred into

water by self-assembly of F127 molecules onto the MSN surface through the hydrophobic interaction between the PPO block of F127 and surface octyl groups of the MSNs (Figure 2.1). Similarly, PAs spontaneous cover the surfaces of OMSNs (for peptide case nanoparticles are labelled with fluorescein dye for uptake studies) in aqueous media through hydrophobic interactions between octyl groups of OMSNs and alkyl chains of PAs (Figure 2.1).

In the first part of the study, we prepared cargo (dye or drug) loaded and PEGylated MSNs by loading the hydrophobic MSNs before the F127 capping process. The F127 capped particles are dispersible in both water and phosphate buffered saline (PBS), whereas uncapped MSNs are easily aggregated and precipitated. The improved biocompatibility of F127 capped MSNs was demonstrated using cytotoxicity, hemolytic activity and thrombogenicity assays. Lastly, cargo release kinetics of PEGylated MSNs was investigated. The cargo release from PEGylated MSNs was very slow which make them a promising candidate for bioimaging and cell labeling studies.

In the second part of the study, we selected two model PA molecules, with different charges, to functionalize MSNs with peptides. The glutamic acid and lysine residues on the PAs provide negative and positive charges to the hybrid system, respectively (Figure 2.2). The unmodified MSNs were synthesized in order to compare with peptide functionalized MSNs. The effect of peptide functionalization on cell viability and uptake was investigated by using human umbilical vein endothelial cells (HUVECs) and a vascular smooth muscle cell line (A10). All of the MSN systems demonstrated good cytocompatibility with both cell lines up to a concentration of 200 mg/mL. Interestingly, we observed a remarkable increase (1.8 to 6.3 fold) in the cellular uptake of peptide functionalized MSNs compared to bare MSNs depending on the surface charge of PAs as well as the cell type.

These works published on the Chemical Communications (2013, *49*, 9782-9784) and Journal of Materials Chemistry B (2014, *2*, 2168-2174) journals. Reproduced with permission from The Royal Society of Chemistry.
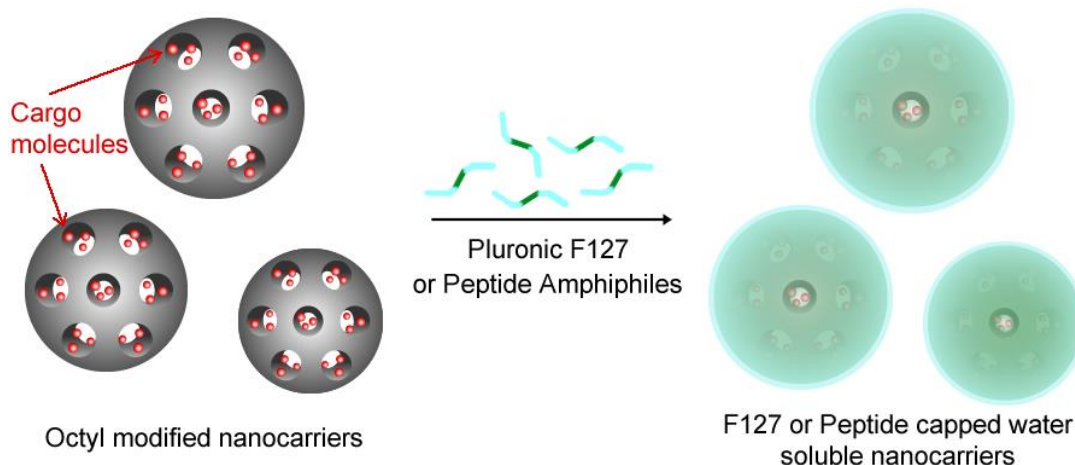
Figure 2.1: Schematic representation of cargo loaded and F127 or peptide amphiphile capped MSN preparation.

Lauryl-PPPPGK-Am (K-PA)

Lauryl-PPPPGE-OH (E-PA)
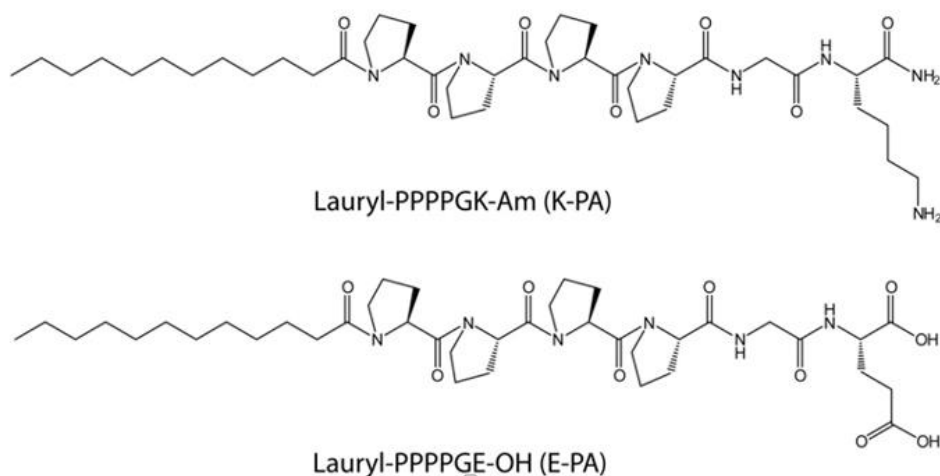
Figure 2.2: Chemical structures of the peptide amphiphile molecules used in this study.

2.2 Experimental Section

Materials: Tetraetyl orthosilicate (TEOS), octyltriethoxysilane (OTS), aminopropyl triethoxysilane (APTES), ammonium nitrate, and hydrofluoric acid (HF), sodium hydroxide, lauric acid were purchased from Merck. Fluorescein isothiocyanate (FITC), cetyltriammoniumbromide (CTAB) ethanol, pluronic polymer (F127), ethanol, hydrochloric acid (37%) (HCl), and doxorubicin hydrochloride (DOX) were purchased from Sigma-Aldrich. Dimethyl sulphoxide (DMSO), methanol, and

isopropanol (IPA) were purchased from Carlo-Erba. Tetrahydrofuran (THF) was purchased from Labkim. 9-Fluorenylmethoxycarbonyl (Fmoc) and *tert*-butoxycarbonyl (Boc) protected L-amino acids, [4-[α-(2',4'-dimethoxyphenyl) Fmocaminomethyl]phenoxy] acetamidonorleucyl-MBHA resin (Rink amide MBHA resin), and 2-(1*H*-Benzotriazol-1-yl)-1,1,3,3 tetramethyluronium hexafluorophosphate (HBTU) were purchased from NovaBiochem and ABCR. All reagents and solvents were used as provided.

Synthesis of MSNs: To synthesize OMSN, first 200 mg CTAB and 5 mg F127 were dissolved in 96 mL of deionized water and 0.7 mL of 2 M NaOH was added. Then the reaction mixture was heated to 80 °C while stirring vigorously (600 rpm) and 1 mL of TEOS was rapidly added under vigorous stirring (600 rpm). After 90 min, to prepare the octyl containing shell, 0.25 mL of OTS was dissolved in 10 mL THF and slowly added to the reaction mixture. The mixture was further stirred for 3 h. Finally, reaction mixture was cooled down to the room temperature, particles were collected by centrifugation at 9000 rpm for 20 min and washed with ethanol twice. Surfactant molecules were extracted by stirring the particles in 50 mL of 20 g/L ethanolic ammonium nitrate at 60 °C for 30 min. This treatment repeated twice to ensure complete surfactant removal. Particles were washed with methanol twice afterwards and dried at 50 °C overnight. MSN was synthesized without the addition of OTS; other parameters were same with the O-MSN synthesis.

Synthesis of FITC labelled MSNs: In order to synthesize FITC labelled MSNs, first 2 mg of FITC conjugated with 10 μL of APTES in 1 mL of EtOH by gently stirring for 24 h. This solution was added to the reaction mixture right after the TEOS addition. Other parameters were same with the MSN synthesis.

Synthesis and characterization of peptide amphiphile molecules: While positively charged peptide amphiphile was constructed on MHBA Rink Amide (0.59 mmol/g) resin, negatively charged peptide amphihpile was constructed on Fmoc-Glu-Wang (0.64 mmol/g) resin. All amino acid couplings were performed with 2 equivalents of Fmoc protected amino acid, 1.95 equivalents of HBTU and 3 equivalents of N,N-diisopropylethylamine (DIEA) in DMF for 2 h. Fmoc deprotections were performed with 20% piperidine/dimethylformamide (DMF) solution for 20 min. Cleavage of the peptides from the resin was carried out with a mixture of trifluoroacetic acid (TFA) :

triisoproplysilane (TIS) : water in the ratio of 95 : 2.5 : 2.5 for 2 h. Excess TFA was removed by rotary evaporation. The remaining viscous peptide solution was treated with ice-cold diethyl ether and the resulting white pellet was freeze-dried.

Characterization of MSNs: Transmission electron microscopy (TEM) images were taken using a Tecnai G2 F30 (FEI) microscope. Average particle sizes and zeta potentials of MSNs were measured with Zetasizer Nanoseries (Malvern Instruments). Surface area and pore volume of the particles were determined using iQ-C (Quantachrome). Before measurements, all samples were degassed at 150 ℃ for 24 h. Thermal gravimetric analyses (TGA) were performed with Q500, (TA Instruments). Fourier transform infrared (FTIR) spectra of particles were recorded by using a Fourier transform infrared spectrometer (FTIR, Vertex 70, Bruker). Optical absorption measurements in cytotoxicity and hemolysis assays were carried out using a Microplate reader (Spectramax M5, Molecular Devices). Fluorescence spectra of the particles were recorded by a Fluorescence Spectrophotometer (Eclipse, Varian).

Characterization of peptide amphiphile molecules: The peptide amphiphiles were identified and analyzed by reverse phase HPLC on an Agilent 6530 accurate-Mass Q-TOF LC/MS equipped with an Agilent 1200 HPLC. An phenomenex Luna 3µ C8 100A (50 x 3.00 mm) column as stationary phase and water/acetonitrile gradient with 0.1% volume of formic acid as mobile phase were used to identify positively charged peptide amphiphile. For negatively charged peptide amphiphile, an Agilent Zorbax Extend-C18 (2.1x50 mm) column as stationary phase and water/acetonitrile gradient with 0.1% volume of ammonium hydroxide as mobile phase were used. The positively and negatively charged peptide amphiphiles were purified by using 1200 Agilent HPLC on Zorbax 300SB C8 (21.2x150 mm) PrepHT and Zorbax-Extend C18 (21.2x150 mm) PrepHT column, respectively.

F127 capping of OMSN: 25 mg of OMSN was dispersed in 50 mL of F127 solution in water (5 mg/mL) by sonication and stirring. The dispersion sonicated for 15 min and afterwards stirred vigorously for 1 h. F127 capped particles were precipitated at 9000 rpm for 20 min and redispersed in 50 mL of F127 solution in water (5 mg/mL). Aforementioned sonication and stirring steps were repeated. Finally, particles were precipitated and washed with water or phosphate-buffered saline (PBS) twice to remove the excess F127 molecules.

Peptide amphiphile capping of OMSN: While 14 mg of each peptide amphiphile was sonicated in 12 mL deionized water, 2 mg of OMSN was slowly added to the system. Peptide amphiphiles and OMSN were mixed with a weight ratio of 1:7. They were sonicated and vortexed for 3 h at RT. Solution was centrifugated at 5000 rpm. After all portions were concentrated by centrifugation, they were rinsed with water and centrifugated twice.

DOX loading and release experiments: In order to load DOX into the pores of MSN or O-MSN, 10 mg of particles were dispersed in 1 mL of DOX solution (7.5 mg/mL) in ethanol and shook at 300 rpm for 24 h. Then the particles were collected by centrifugation. DOX loaded MSNs were washed with water twice to remove the non-adsorbed DOX molecules. For OMSN before precipitation 5 mg of F127 added into the solution. DOX loaded OMSN were transferred into the water as described above to produce DOX loaded F127-OMSN. The amounts of adsorbed DOX were determined by monitoring the fluorescence of DOX at 590 nm (excitation wavelength is 488 nm) after etching the silica in 1.2% HF solution for overnight.

DOX release profiles of MSN and F127-OMSN was determined by dispersing 5 mg of particles in 8 mL of PBS at pH 7.4 or pH 5.5 and each solution were separated to 10 Eppendorf tubes. The tubes were shaken at 37 °C for 12 h and at different time intervals one tube removed and centrifuged. The volumes of supernatants were completed to 20 mL and fluorescence peak of DOX at 590 nm was monitored using a fluorescence spectrophotometer in order to determine the released DOX amount.

R6G loading and release experiments: In order to load R6G into the pores of MSN or O-MSN, 30 mg of particles were dispersed in 15 mL of R6G solution (7.5 mg/mL) in IPA and stirred at 60 °C for 2 days. Then the particles were collected by centrifugation at 9000 rpm for 20 min. R6G loaded MSNs were washed with water to remove the non-adsorbed R6G molecules. On the other hand, R6G loaded OMSNs were washed with water after capping with F127 since OMSN is insoluble in water. R6G loaded F127-OMSN was prepared as described above using R6G loaded O-MSNs and washed with water before using in release experiments. The amounts of adsorbed R6G were determined by monitoring the absorption peak of R6G at 526 nm after etching the silica in 1.2% HF solution for overnight.

Cargo release profiles of the R6G loaded MSN and F127-OMSN was determined

by dispersing 10 mg of particles in 25 mL PBS (pH 7.4). The dispersions were stirred at 37 °C for 48 h and at different time intervals small amount of samples were taken and centrifuged. Then, amount of released R6G in the supernatants were calculated using a UV-Vis spectrophotometer from the absorption peak of R6G at 526 nm.

Cell culture for PEGylated OMSN: Human breast adenocarcinoma cells (MCF-7) were grown to confluence at 37 °C under 5% CO_2 in Dulbecco's Modified Eagle Serum (DMEM) containing 1% penicillin/streptomycin, 10% fetal bovine serum (FBS) and 2 mM L-glutamine.

Cell viability tests for PEGylated OMSN: Cells in the logarithmic growth phase were washed once with PBS, trypsinized and resuspended in fresh medium. The cells were seeded in 96-well plates at 5×10^3 cells/well. After 24 h of culture, the medium was removed by aspiration and replaced with 100 μL of fresh medium containing MSN or F127-OMSN at concentrations of 100, 250, 500 or 1000 μg/mL and incubated for 24 or 48 h. The cytotoxicity of particles was determined by the 3-(4,5-dimethyl-2-thiazolyl)-2,5-diphenyltetrazolium bromide (MTT) reduction assay (Sigma, Aldrich). At least two well columns containing cells without the particles were used as a negative control. MTT reagent (5 mg/mL) containing medium was added to each well, and the plates were incubated in the dark for 4 h at 37°C. After incubation, medium was removed and the resulting purple formazan crystals were dissolved by adding medium. Then the optical density was measured at 570 and 680 nm by using a microplate reader (SpectraMax, M5). The optical density of wells containing untreated cells was considered as 100%. All the experiments were performed in triplicate.

Cell culture for peptide coated OMSN: Viability and uptake experiments were performed by using human umbilical vein endothelial cells (HUVECs) and A10 rat aortic smooth muscle cells (ATCC® Cat# CRL-1476™). HUVECs were donated by Yeditepe University, Istanbul, Turkey. HUVECs were purified as described [44, 45] and characterized by staining with CD34, CD31, and CD90 surface markers. These cells were found to be positive for CD31 and CD34 but negative for CD90. A10 and HUVEC cells were cultured in 75 cm^2 polystyrene cell culture flasks with standard medium, containing Dulbecco's modified eagle medium (DMEM) with 10% fetal bovine serum (FBS), and 1% penicillin–streptomycin and passaged at cell confluency between 80 and 90% using trypsin-EDTA. In all experiments, particles were

administered in serum free medium (1% penicillin-streptomycin containing DMEM) to avoid any influence of serum proteins on the uptake mechanism.

Cell viability tests for peptide coated OMSN: The cell viability assay was performed using Alamar Blue Assay (Invitrogen). 5000 cells per well (HUVECs or A10) were seeded on a 96-well plate in 100 mL of standard medium. After 24 h, the medium was removed and 100 mL of serum free medium was added. 25 mL of freshly prepared nanoparticle solutions in water at different concentrations were administered to have final concentrations of 200, 100, 50, and 10 µg/mL. For cell viability tests, cells were exposed to particles for 4 h, then the medium was changed to standard medium and the cells were further incubated for 20 h. Then, Alamar Blue reagent diluted to 10% in DMEM was added. After 3 h, fluorescence at 570/612 nm (Ex/Em) was measured using a microplate reader (SpectraMax, M5).

Hemolysis assay: EDTA stabilized human blood samples were collected from volunteers at Bilkent University Health Center (Ankara, Turkey). Fresh blood samples (3 mL) were centrifuged at 1600 rpm for 5 min and RBCs were obtained after removing the blood plasma. Precipitated RBC pellet was washed five times with 6 mL of PBS and RBCs were dispersed in 25 mL of PBS. 0.2 mL of RBCs were placed in plastic vials and 0.8 mL of MSN or F127-OMSN solutions in PBS at different concentrations were added. Also, positive and negative control samples were prepared by adding 0.8 mL of water and PBS, respectively. The samples were incubated at room temperature for 2 h. Samples were slightly shaken once for every 30 min to resuspend the RBCs and MSNs. After incubation, RBC were precipitated at 1600 rpm and 200 µL of supernatants was transferred to a 96-well plate to measure the absorbance of released hemoglobin, from damaged RBCs, with a microplate reader at 570 nm. Absorbance at 655 nm was recorded as reference. Hemolysis percentages of the RBCs were calculated using the following formula;

% Hemolysis = (abs of sample-abs of negative control) / (abs of positive control-abs of negative control)

Percent hemolysis values were calculated from three separate experiments.

Blood clotting assay: For PT and aPTT measurements, human blood samples were collected to citrate stabilized vials from volunteers. Plasma samples were freshly prepared from the blood samples and immediately used in the experiments. 50 µL of

MSN or F127-OMSN solutions in PBS were added to the 450 µL of plasma samples, and incubated for 5 min at 37 °C. Final particle concentrations in the resulting solutions were 0.1 and 1 mg/mL. After incubation, particles were removed by centrifugation and 50 µL portions of supernatants were used to measure PT and aPTT values using a semi-automatic blood coagulation analyzer (Tokra Medikal, Ankara, Turkey). Also, control measurements were performed using 50 µL PBS. All PT and aPTT values were calculated from three separate measurements.

Uptake studies: 13 mm glass coverslips were placed in 24 well plate, 40000 cells (HUVEC or A10) in standard medium (DMEM with 10% FBS, 1% PS) were seeded in each well on coverslips. After 24 h medium was discarded, 400 µL of serum free medium was added to each well. 100 µL of bare or functionalized MSN particles were administered to have a 200 µg/mL final concentration of MSN. After 4 h of administration medium was changed to standard medium. After 20 h cells were washed with PBS several times and fixed with 4% paraformaldehyde for 15 min. Then, cells were permeabilized with 0.1% TritonX-100 (Sigma-Aldrich) for 12 min and actin proteins were stained with Phalloidin-TRITC (Sigma-Aldrich) for 20 min. Coverslips were mounted on slides with Antifade (Invitrogen). Samples were visualized under laser scanning confocal microscopy (Zeiss, LSM 510).

Flow Cytometer Analysis: 100000 HUVEC or A10 cells were seeded in each well of 6 well plate in standard medium (DMEM with 10% FBS, 1% PS). After 24 h medium was discarded, 1600 µL of serum free medium was added in each well. 400 µL of bare or functionalized MSN particles were administered to have a 200 µg/mL final concentration of MSN. After 4h of administration, medium was changed to standard medium and cells were incubated for 20 h, then washed with PBS and trypsinized. Cells were collected by centrifugation and washed twice with PBS. Cells were resuspended in 1 mL PBS and kept on ice before analysis. FITC channel is used to analyze MSN particle uptake in flow cytometer (BD, FACS Aria III). Student's t-test was applied to all datasets and the difference between them was accepted to be statistically significant when $p < 0.05$.

2.3 Synthesis and Characterization of PEGylated MSNs

Octyl modified MSNs (OMSN) were prepared via respective condensation of tetraethyl orthosilicate (TEOS) and octyltriethoxy silane (OTS) monomers in a one-pot reaction [45-47]. After polymerization of TEOS and formation of initial MSNs, OTS monomers were added in order to obtain hydrophobic coatings on MSNs. Also, for control experiments bare MSNs were synthesized without the addition of OTS. Figure 2.3 shows TEM images of the prepared MSNs. The MCM-41 type ordered hexagonal porous structure was observed for bare MSN (Figure 2.3a). Interestingly, OMSN revealed bimodal pore structure; a randomly porous shell was observed over the MCM-41 type porous core (Figure 2.3b). The shell thickness was calculated to be 12 ± 3 nm from the TEM images. Also, average particles sizes and particle size distributions for both particles were determined from TEM images and given in Figure 2.4.
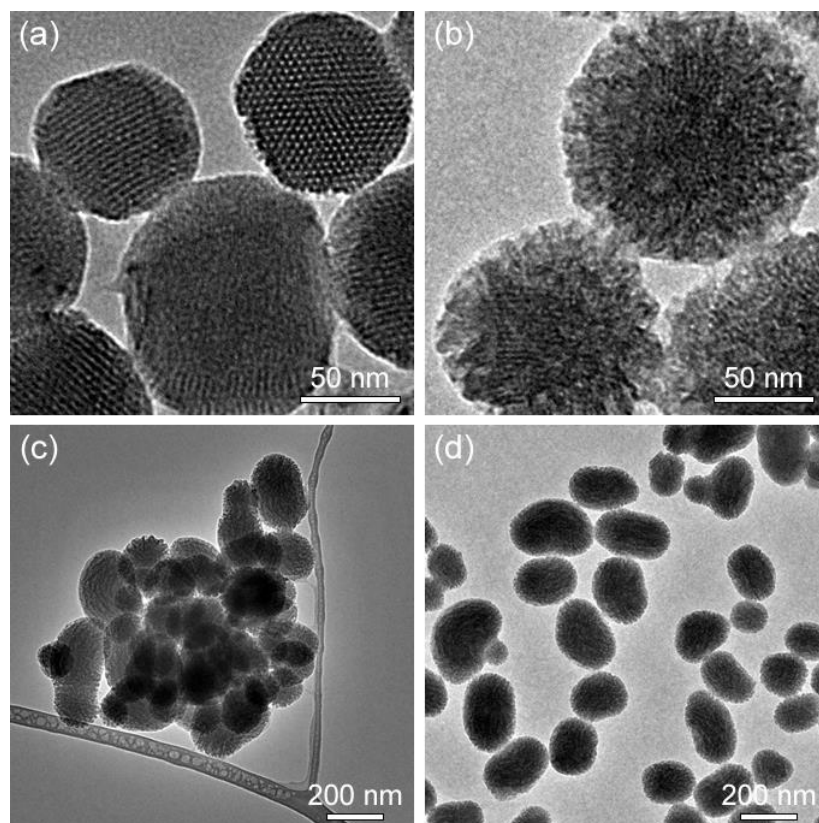
Figure 2.3: TEM images of mesoporous silica nanoparticles. (a) Bare MSN, (b) and (c) OMSN, and (d) F127-OMSN.
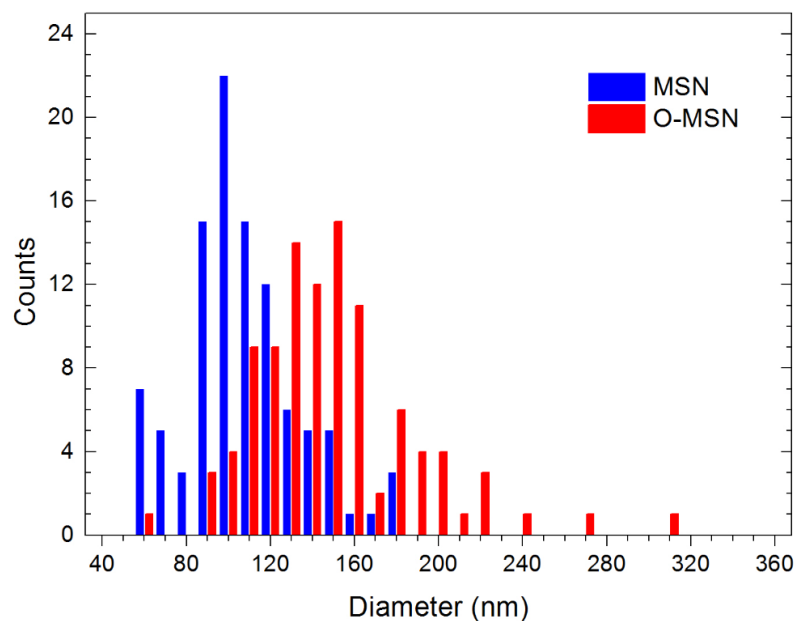
Figure 2.4: Particle size distributions of MSN and OMSN which were calculated according to the TEM images. Octyl modification significantly increased particle size indicating octyl containing shell formation.

Surface area and pore volume of the particles were calculated from the adsorption/desorption data (Figure 2.5). OMSN revealed slightly lower surface area (961.2 m^2/g) and pore volume (1.01 cm^3/g) compared to MSN (1115.7 m^2/g and 1.25 cm^3/g). The decrease in the surface area and pore volume is the result of pore narrowing after octyl modification [45]. OMSN formed aggregates while drying on the TEM grid, due to the hydrophobic interactions between particles (Figure 2.3c). On the other hand, after coating with the pluronic polymer (F127-OMSN), particles are well dispersed on the grid (Figure 2.3d) indicating the formation of F127 coating on particles.

15
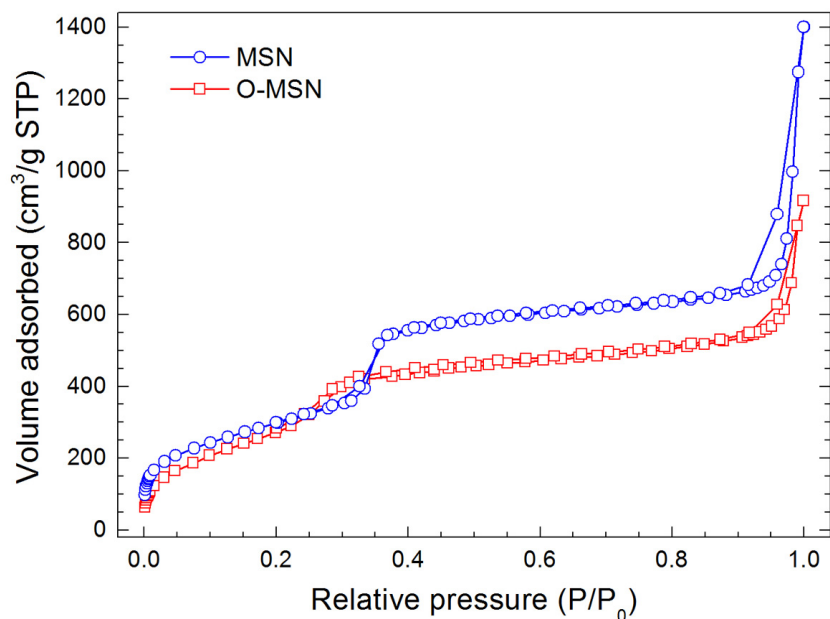
Figure 2.5: Nitrogen adsorption and desorption curves of MSN and OMSN. Octyl addition slightly reduced the surface area and pore volume of the particles.

The formation of F127 layer on particles was further confirmed by TGA (Figure 2.6). For MSN, weight loss at 800 °C was only 8.3% which is due to residual surfactant molecules and dehydroxylation of silica surface [48]. For OMSN, weight loss reached to 18.8% due to the decomposition of octyl groups. On the other hand, a large weight loss (47.1%) was observed for F127-OMSN. There are two sharp decreases in the TGA spectrum of F127-OMSN, which are corresponding to decomposition of F127 and octyl groups. In addition, FTIR spectra (Figure 2.7) of the particles clearly demonstrated the successful octyl modification and F127 capping of MSNs.
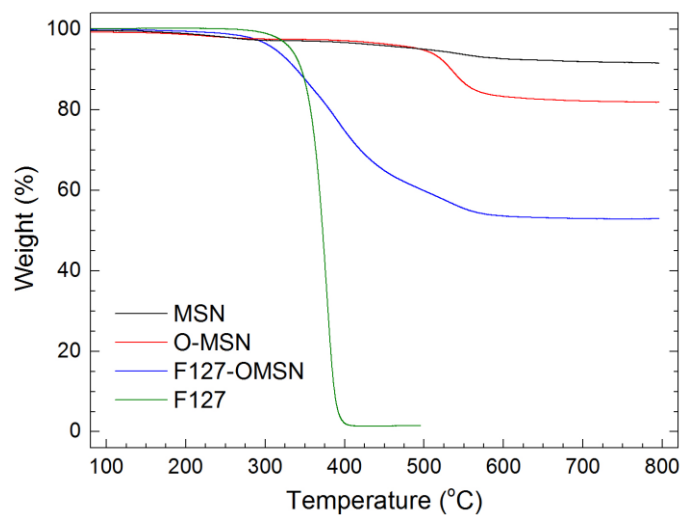
Figure 2.6: TGA spectra of MSN, OMSN, F127-OMSN and F127 polymer. After octyl addition and F127 capping weight loss of the particles gradually increased proving the formation of octyl and F127 layer around MSNs.
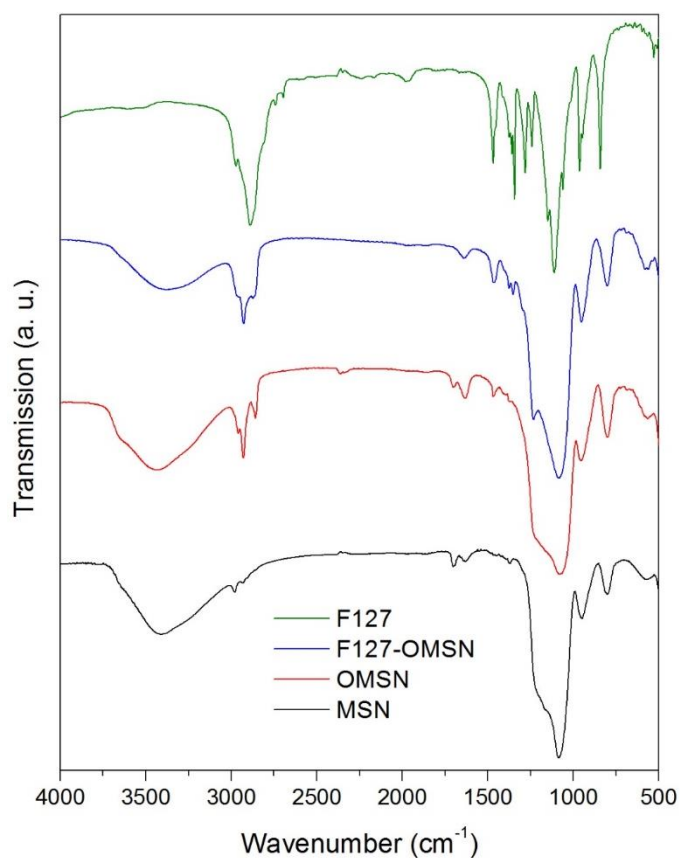
Figure 2.7: FTIR spectra of MSN, O-MSN, F127-OMSN and F127 polymer showing successful octyl modification and F127 capping of particles.

Good dispersity in biological media is vitally important for developing biocompatible and effective nanomaterials for biological applications, since aggregated particles can induce toxicity in several organs and result in poor pharmacokinetics [49]. The F127-OMSN showed excellent dispersity in both water and PBS (pH = 7.4) at a high concentration (1 mg/mL). The particle size distribution in both media was almost identical and average particle size was around 280 nm (Figure 2.8). The good aqueous dispersity of F127-OMSN in highly salted media is attained by and non-ionic and hydrophilic PEG blocks. On the other hand, MSN was fairly dispersible in water at 1 mg/mL, with slightly broader size distribution than F127-OMSN and an average particle size around 235 nm (Figure 2.8). However, MSN easily aggregated and precipitated in highly salted PBS media in a couple of minutes at the same concentration (Figure 2.8 inset). Therefore, a more dilute solution (0.1 mg/mL) was used to retard the particle precipitation and particle size distribution of MSN in PBS was determined. Even at this low concentration MSN formed large aggregates and exhibited a broad particle size distribution with a large average particle size of ~2 μm (Figure 2.8).
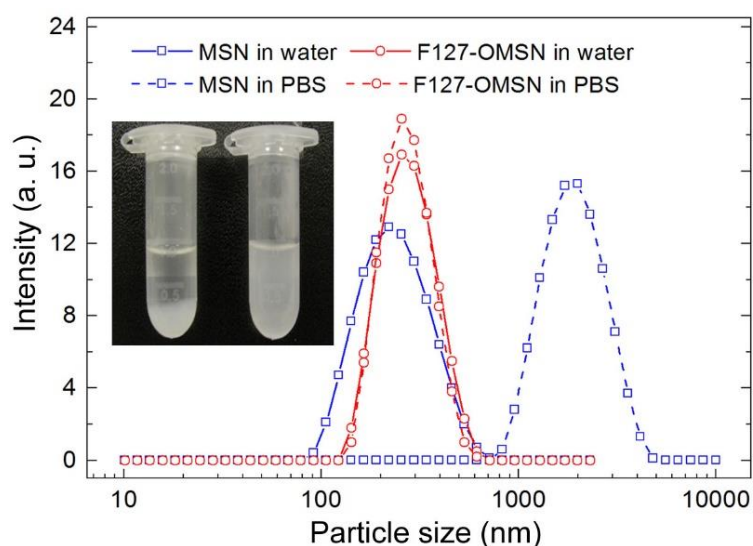
Figure 2.8: Dispersibility of MSN particles in aqueous media. Size distributions of MSN and F127-OMSN in water and PBS. Inset show the photograph of MSN (left) and F127-OMSN (right) dispersions in PBS showing the colloidal stability of PEGylated MSNs.

To test the stability of F127 coating, we precipitated the particles, removed the supernatant and re-dispersed them in PBS; this cycle was repeated for ten times. Average particle size almost remained intact after the washing cycles (Figure 2.9). The good stability of the F127 layer is due to the strong hydrophobic interaction between octyl groups of OMSN and hydrophobic PPO block of the F127, which is stronger than either hydrogen bonding or electrostatic interactions in highly salted solutions [21].
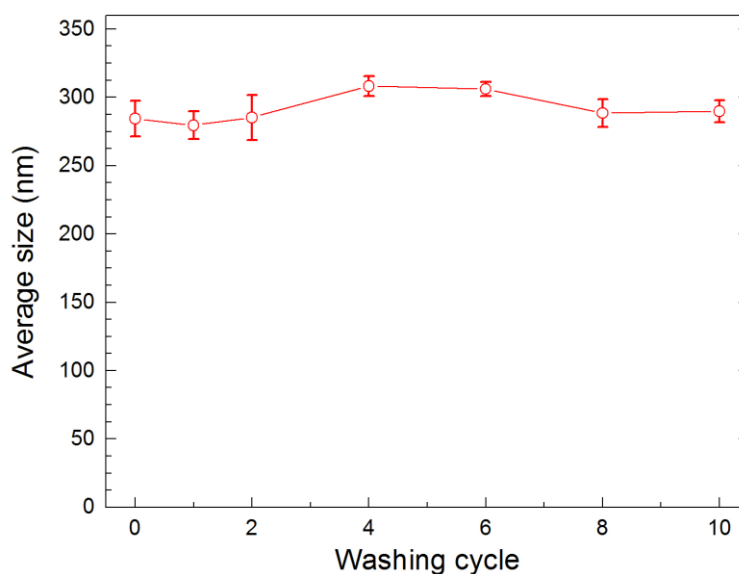
Figure 2.9: The average zeta size of F127-OMSN in PBS after several washing cycles. Even after 10 washing cycles average particle size remained almost intact indicating the good stability of self-assembled pluronic layer.

2.4 Biocompatibility of PEGylated MSNs

In order to evaluate the *in vitro* cytocompatibility of the particles 3-(4,5-dimethylthiazol-2-yl)-2,5-diphenyl-tetrazolium bromide (MTT) cytotoxicity assay was used between particle concentrations of 0.1 and 1 mg/mL. Figure 2.10 indicates that both MSN and F127-OMSN are highly compatible with MCF-7 (human breast cancer cell line) cells after incubation times of 24 or 48 h.
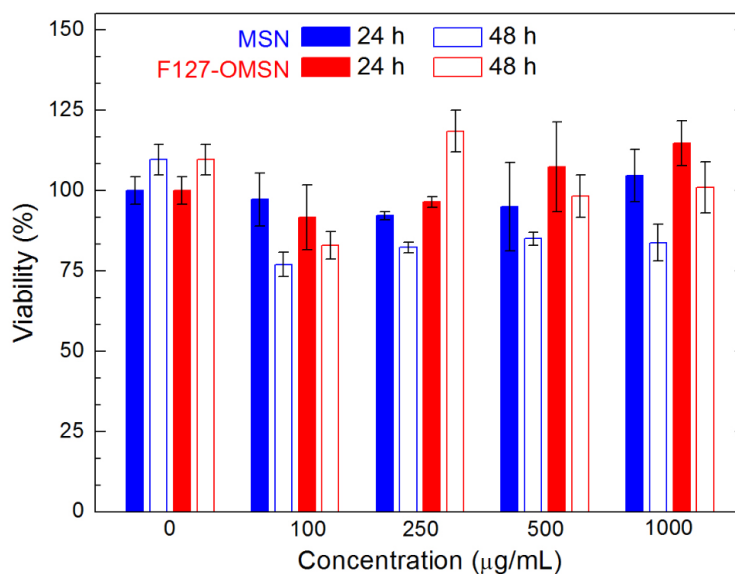
Figure 2.10: Cell viability results of MSN and F127-OMSN after 24 and 48 h.

Blood compatibility of nanomaterials is a crucial issue when they are applied by intravenous injection, a commonly applied route for drug delivery [18, 50]. It is well known that interaction of MSNs with blood constituents may cause serious toxicity such as hemolysis of red blood cells (RBCs) and blood clot formation (thrombogenicity) [17, 51]. Therefore, we investigated the hemolytic activity and thrombogenicity of MSNs and F127-OMSN using a hemolysis assay [17] and measuring their activated partial thromboplastin time (aPTT) and prothrombin time (PT) [51]. Hemolytic activity of the particles was monitored by measuring light absorption (at 570 nm) of released hemoglobin from the lysed RBCs. MSN revealed significant hemolytic activities of 5.8% at 0.25 mg/mL and 56.8% at 1 mg/mL (Figure 2.11a). Strong electrostatic interaction between negatively charged silanol groups and positively charged trimethyl-ammonium head groups of the membrane lipids can cause membranolysis of RBCs [50]. Capping the MSNs with uncharged F127 molecules completely prevented the hemolytic activity even at high particle concentration (1 mg/mL) by blocking the electrostatic interaction of silanol groups with the RBC membrane (Figure 2.11a). Also, photograph of the MSN treated RBCs show the released hemoglobin (red colour) to the supernatant, whereas no red colour was observed for F127-OMSN treated cells (Figure 2.11a, inset). PT and aPTT test are

applied to investigate extrinsic and intrinsic blood coagulation pathways, respectively. The PT and aPTT results of the particles at low (0.1 mg/mL) and high (1 mg/mL) concentrations revealed that all the values are in their normal range (Figure 2.11b) [50]. It is well known that some dry and porous silica materials can activate the coagulation cascade due to their high absorption capacities [51]. On the other hand, the pores of the MSN and F127-OMSN are already filled with PBS, which significantly decreases the absorption capacity of particles and results in the observed non-coagulant behaviour of the particles [50, 51].
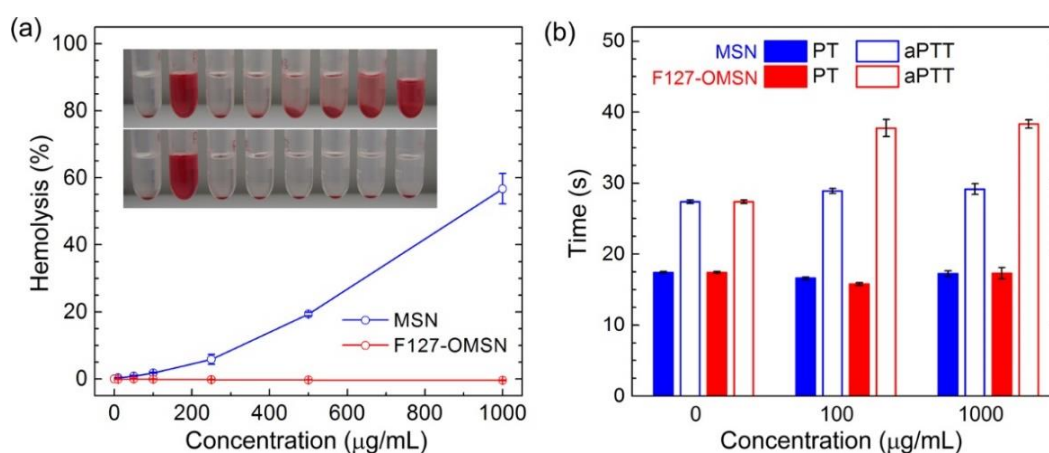
Figure 2.11: (a) Hemolysis results of MSN and F127-OMSN. Inset shows photographs of RBCs treated with MSN (up) and F127-OMSN (down) at different concentrations. (b) PT and aPTT values of particles.

2.5 Fluorescent Dye or Drug Loaded PEGylated MSNs

To prepare fluorescent PEGylated MSNs, we loaded Rhodamine 6G (R6G) dye to OMSN [52]. Also, for control experiments we loaded R6G to MSN. We calculated a R6G loading capacity of 6.21 wt % for MSN. For O-MSN, we observed a lower loading efficiency (2.74 wt %) at same conditions which is due to the lower surface area and pore volume of octyl modified particles. Also, blocking of the negatively charged silanol groups, which are expected to interact electrostatically with the positively charged R6G molecules, by octyl groups may contribute to the lower drug absorption capacity of the OMSN. Powder of R6G loaded OMSNs were directly capped with F127 in PBS. Figure 2.12a shows the fluorescence spectrum of R6G

loaded F127-OMSN. We observed very slow release of R6G for R6G loaded F127-OMSN which makes it promising for cell labelling and bioimaging applications. It is important to note that same strategy can be applied almost any dye molecule. After 48 h F127-OMSN released only 20.1% of its load, as the R6G loaded pores are closed with F127 layer (Figure 2.12b). The dense polymer layer slows down the R6G release by acting as a diffusion barrier. On the other hand, a typical burst release profile was observed for MSN; 78% of the R6G molecules were released after 12 h.
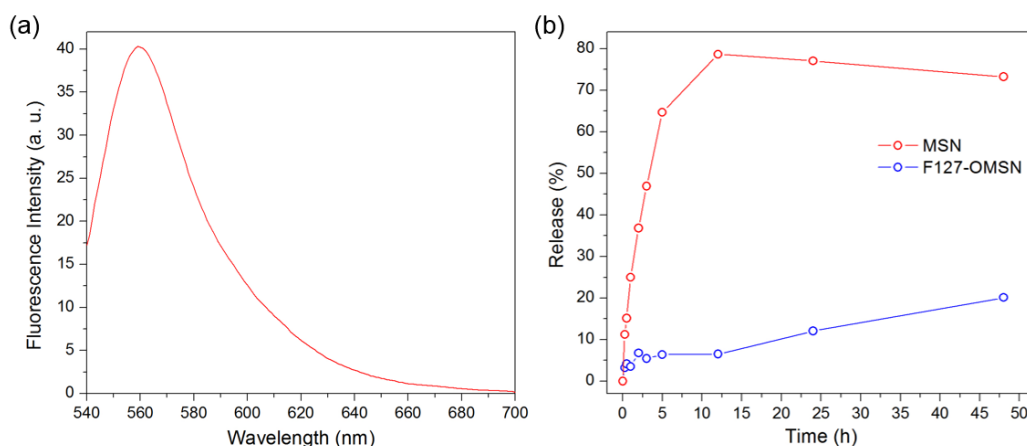
Figure 2.12: (a) Fluorescence spectrum of R6G loaded F127-OMSN. (b)) R6G release profiles of MSN and F127-OMSN.

Drug loading and release studies were performed using a cancer drug, doxorubicin (DOX). We calculated a DOX loading capacity of 15.3 µg/mg for MSN. For OMSN, we observed a slightly lower loading efficiency (11.5 µg/mg) at same conditions which is most likely due to the lower surface area and pore volume of octyl modified particles. Powder of DOX loaded OMSNs were directly capped with F127 in PBS (pH 7.4) and used in drug release studies. We observed slower release profiles for F127-OMSN at both acidic (pH 5.5) and neutral (pH 7.4) conditions compared to MSN (Figure 2.13). For instance, at pH 5.5 MSN released 93.9% of its load in 12 hours, on the other hand, 64.2% DOX release was observed for F127-OMSN at same conditions. The F127 polymer layer around the particles slows down the DOX release rate by acting as a diffusion barrier against cargo release from the pores. Also, at pH 5.5 faster DOX release was observed for both particles compared to pH 7.4, which is in good

accordance with the previous reports [52]. The slow rate of DOX release from F127-OMSN can provide more effective therapy by preserving desired drug concentration in the body for longer times.
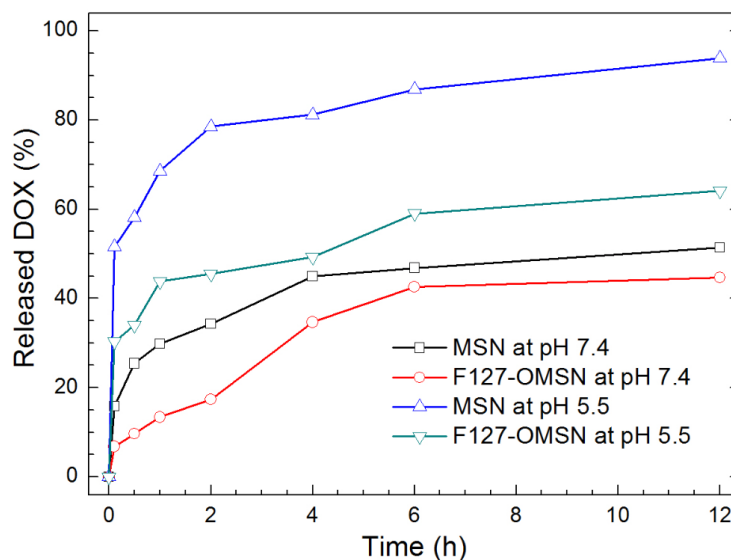
Figure 2.13: DOX release profiles of MSN and F127-OMSN in different pH values.

2.6 Synthesis and Characterization of Peptide Functionalized MSNs

Octyl modified water insoluble MSNs (OMSNs) were synthesized according to our previous reports [46, 53] by using a one-pot respective condensation method [45]. Tetraethyl orthosilicate (TEOS) molecules were condensed under basic conditions and initial MSNs were formed. Then, octyl triethoxysilane (OTS) molecules were added to the reaction mixture to coat the MSNs with a hydrophobic octyl layer. The fluorescein isothiocyanate (FITC) molecules were conjugated to the MSNs in the first step of the synthesis to track the uptake of particles by using confocal imaging and flow cytometry methods [54]. Successful conjugation of FITC to the silica network was demonstrated by using fluorescence spectroscopy, where emission bands of FITC molecules were clearly observed (Figure 2.14). Bare MSNs were prepared for control experiments under the same experimental conditions without the OTS addition.
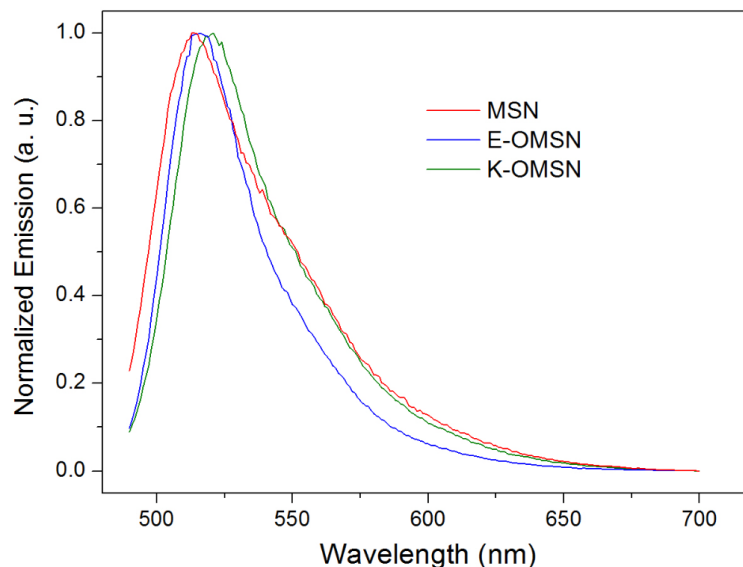
Figure 2.14: Fluorescence spectra of MSNs showing the successful FITC conjugation to the silica network.

Peptide amphiphiles (PAs) were synthesized by solid phase peptide synthesis method based on orthogonal protection and verified by liquid chromatography and mass spectrometry (data not shown). OMSNs were coated with PA molecules by simple sonication in E-PA or K-PA solutions (Figure 2.15a). As-prepared OMSNs are insoluble in water (Figure 2.15a, left) because their surface is covered with hydrophobic octyl groups. After the addition of PA solution and ultrasonication, PA molecules self-assembled on the OMSNs due to hydrophobic interactions between alkyl chains of both OMSNs and PAs. Functionalization with PAs renders the MSNs water dispersible by providing either positively or negatively charged water soluble moieties on their surfaces (Figure 2.15a, right). Photographs of MSNs dispersed in water are shown in Figure 2.15b. Both dispersions have light green color due to the covalently conjugated FITC molecules.
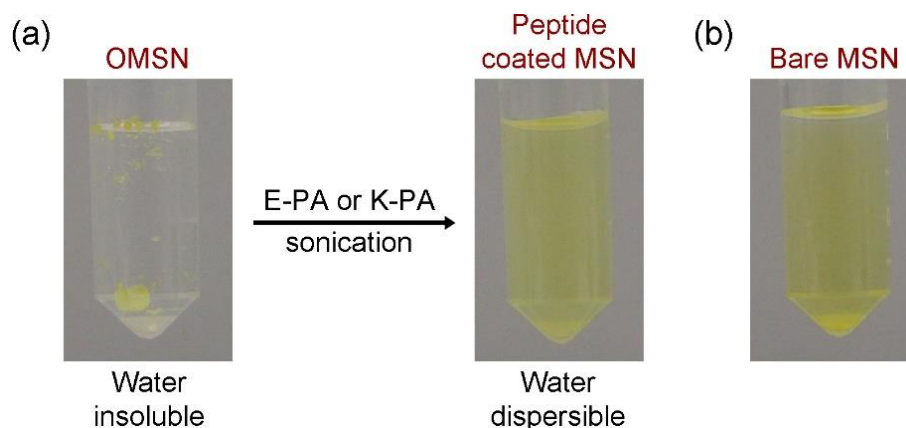
Figure 2.15: (a) Photograph showing the water dispersion of OMSNs before and after coating with peptide amphiphiles and (b) photographs of MSN dispersion in water.

Figure 2.16 shows the TEM images of the particles. Bare MSNs exhibited an MCM-41 type highly ordered hexagonal porous structure (Figure 2.16a). On the other hand, for OMSNs, a randomly porous thin shell was observed over an MCM-41 type porous core (Figure 2.16b) [53]. After coating the OMSNs with E-PAs, a thin organic layer was observed around the particles (Figure 2.16c).
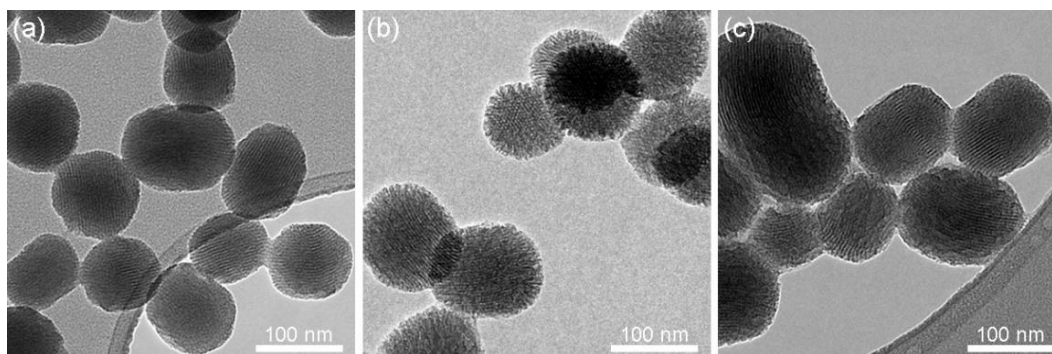
Figure 2.16: Characterization of the mesoporous silica nanoparticles. TEM images of (a) MSNs, (b) OMSNs and (c) E-OMSNs.

The formation of a peptide coating over OMSNs was further proved by using FTIR and TGA methods. Figure 2.17a shows the FTIR spectra of the particles. The -CH peaks between 2800 cm^{-1} and 3000 cm^{-1} were observed in the spectrum of OMSNs indicating the successful octyl modification. These absorption bands became stronger for PA modified particles (E-OMSNs and K-OMSNs) due to the -CH bonds of the

PAs. In addition, new absorption bands between 1400 cm^{-1} and 1800 cm^{-1} appeared, which are in good agreement with FTIR spectra of the PAs. The amide I (1600-1690 cm^{-1}, C=O stretching) and amide II (1480-1575 cm^{-1}, CN stretching, NH bending) bands of PAs were observed for PA functionalized MSNs. Another C=O stretching vibration was also observed for glutamic acid containing particles at around 1725 cm^{-1} which corresponds to the side chain of the glutamic acid. Figure 2.17b shows the TGA analysis of the particles. For MSNs, a small weight loss of 7.8% was observed between 100 °C and 800 °C due to the dehydroxylation of the silica surface [48]. The weight loss increased to 11.9% for OMSNs and most of the weight loss occurred at around 500 °C indicating the decomposition of octyl moieties [53]. For E-OMSNs and K-OMSNs large weight loss values of 19.6% and 32.5% were recorded, respectively. Also, two sharp decreases were observed in the spectra of peptide coated particles around 400 °C and 500 °C, which correspond to the decomposition of PAs and octyl groups, respectively. For bare peptide amphiphiles, almost all weight was lost at 800 °C. Based on the TGA results, we calculated grafting densities of the PA molecules on the OMSN surfaces [55, 56]. The grafting densities of E-OMSNs and K-OMSNs were 0.94 and 2.95 PA/nm^2, respectively, indicating that the surface of OMSNs was densely covered by the peptide molecules. A higher grafting density of K-OMSNs was observed due to the electrostatic interactions between positively charged K-PAs and unreacted surface silanol groups of OMSNs.
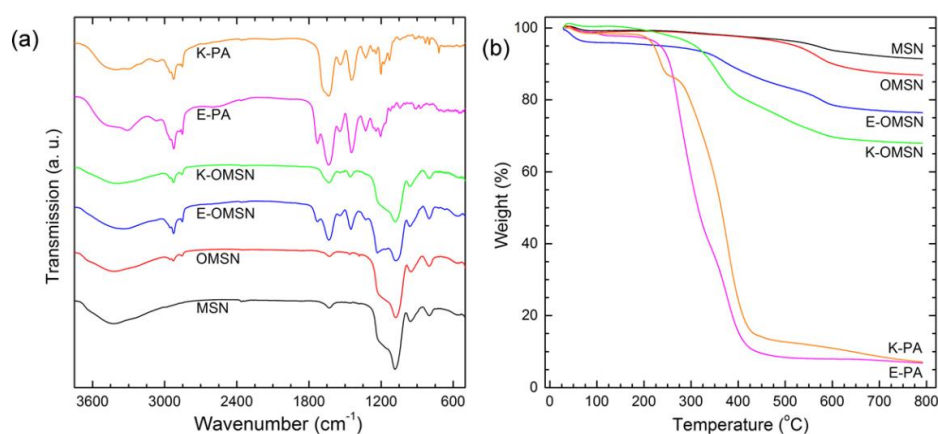
Figure 2.17: FTIR spectra (a) and TGA spectra (b) of particles and peptide amphiphiles, respectively.

Particle sizes of the MSNs and OMSNs were calculated to be 100 nm and 104 nm, respectively from the TEM images (Table 2.1). The 4 nm increase in the particle size after octyl addition shows the ~2 nm shell formation around the particles. Hydrodynamic sizes of the MSN, E-MSN and K-MSN were measured by using the dynamic light scattering technique (Table 2.1). The OMSNs are water insoluble and it is not possible to measure their hydrodynamic size. Hydrodynamic sizes of the peptide coated particles are slightly larger (around 40 nm) than their primary particle sizes (size of OMSNs) due to the slight aggregation in aqueous media for these particles. On the other hand, aggregation becomes more pronounced for bare MSNs with a 67 nm difference between hydrodynamic and primary particle sizes. This difference could be explained by the fact that two different techniques, TEM and DLS, were used for the measurements. While dried samples were used for TEM imaging, the hydrodynamic size of particles was measured using DLS where interactions with solvent molecules are also taken into account. The surfaces of the particles were characterized by measuring their zeta potentials (Table 2.1). The bare MSN surface is negatively charged (-37 mV) due to the surface silanol groups [50]. Modifying the MSN surface with a negatively charged E-PA did not significantly affect the zeta potential of the surface (-38 mV) since both silanol and E-PA groups are negatively charged. Coating the MSN surface with a positively charged K-PA, on the other hand, resulted in a remarkable increase in the zeta potential (-25 mV).

Sample	TEM siz (nm)	DLS size (nm)	Zeta potential (mV)
MSN	99.8 ± 20.7	166.5 ± 8	-36.6 ± 1.1
OMSN	104.3 ± 21.5	N/A	N/A
E-OMSN	N/A	143.8 19.8	-38.0 ± 0.8
K-MSN	N/A	145.2 1.6	-25.1 ± 0.7

Table 2.1: Physical properties of bare, octyl modified and peptide functionalized MSNs

2.7 Cellular Uptake of Peptide Functionalized Fluorescent MSNs

A good compatibility of therapeutic nanoparticles with biological organisms is necessary to prevent possible side effects of these therapies. Accordingly, the *in vitro* cytocompatibilities of the peptide coated and bare MSNs were evaluated by using HUVEC and A10 cell lines. The viability of the cells treated with different particle concentrations (10 to 200 mg/mL) was studied by using the Alamar blue assay. First, cells were treated with particles for 4 h and then incubated for additional 20 h in particle free media. None of the particles showed decrease in the viability of both cell lines even at a very high particle concentration of 200 mg/mL (Figure 2.18).
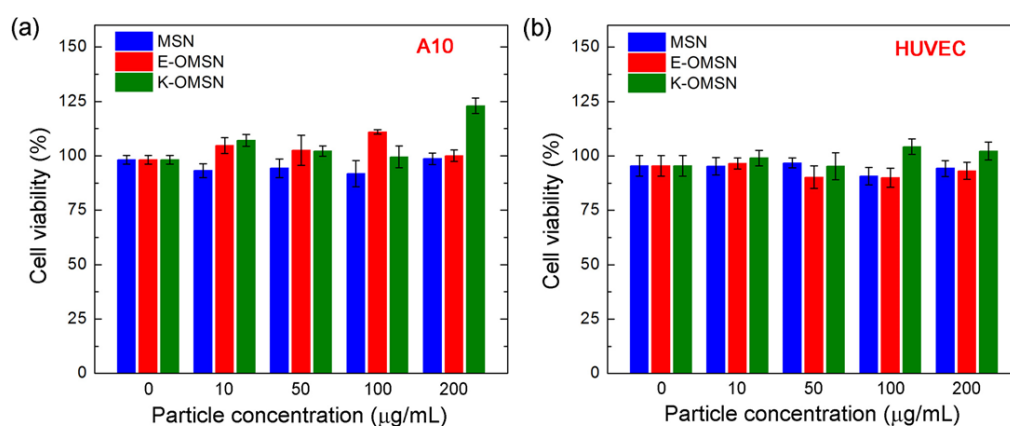
Figure 2.18: Cytotoxicity results of bare and peptide functionalized MSNs. (a) A10 cells incubated for 4 h with particles and 20 h in particle free media and (b) HUVEC cells incubated for 4 h with particles and 20 h in particle free media.

Improving the cellular uptake of the therapeutic nanoparticles is essential for enhancing their efficacy. Therefore, we studied the uptake of the particles by A10 cells and HUVEC by using confocal microscopy and flow cytometry techniques. Both A10 cells and HUVEC were treated with 200 mg/mL nanoparticles for 4 h and the cells were analyzed after 20 h of further incubation. As shown in Figure 2.19, confocal microscopy revealed that the peptide coated particles were internalized remarkably more than the bare MSNs by both cell lines.
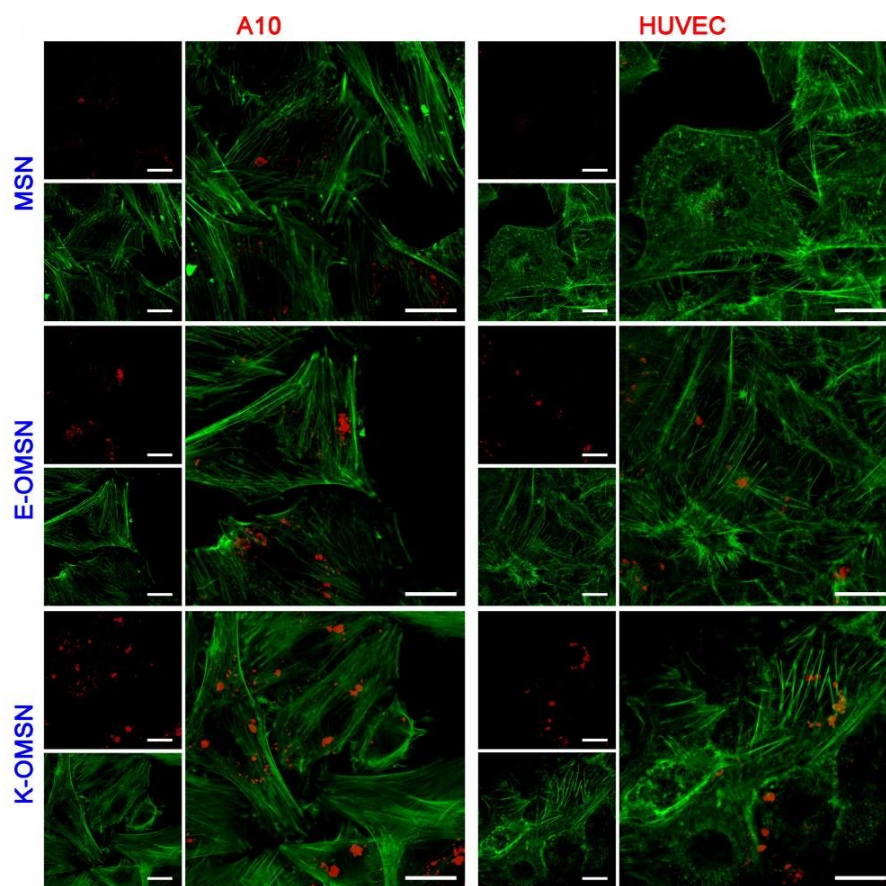
Figure 2.19: Uptake results of bare and peptide functionalized MSNs. Confocal results showing that peptide functionalized particles were internalized more both A10 and HUVEC cell lines. Upper images at left show the fluorescence of particles, lower images at left show the fluorescence of actin filaments stained by Phalloidin-TRITC and panels on right show the merged images. Scale bars: 20 μm.

In order to compare the uptake amount of the particles, the fluorescence of the internalized particles was quantified by using a flow cytometer (Figure 2.20). More uptake was observed for K-OMSNs in both cell lines. The amount of internalized fluorescent E-OMSNs was less than that of K-OMSNs, however, they were internalized more than bare particles. The uptake of K-OMSNs by A10 cells and HUVEC was 2.3 and 6.3 fold larger than the uptake of MSNs, respectively. Also, E-OMSNs demonstrated 1.8 and 3.1 fold increased uptake by A10 cells and HUVEC, respectively, compared to bare MSNs. It is well known that positively charged surfaces can electrostatically interact with the slightly negatively charged cell membrane [57]. Therefore, the highest cellular internalization was observed for positively charged K-

PA functionalized K-OMSNs. Although, both MSN and E-OMSN samples have about the same zeta potential values, around -40 mV, the cellular uptake of E-OMSNs was significantly higher than that of the MSNs. This observation indicates that the uptake rate and the amount of the nanoparticles cannot be simply correlated with the net surface charge of the surface; instead, it is more related to the chemical structure of the surface functional groups.
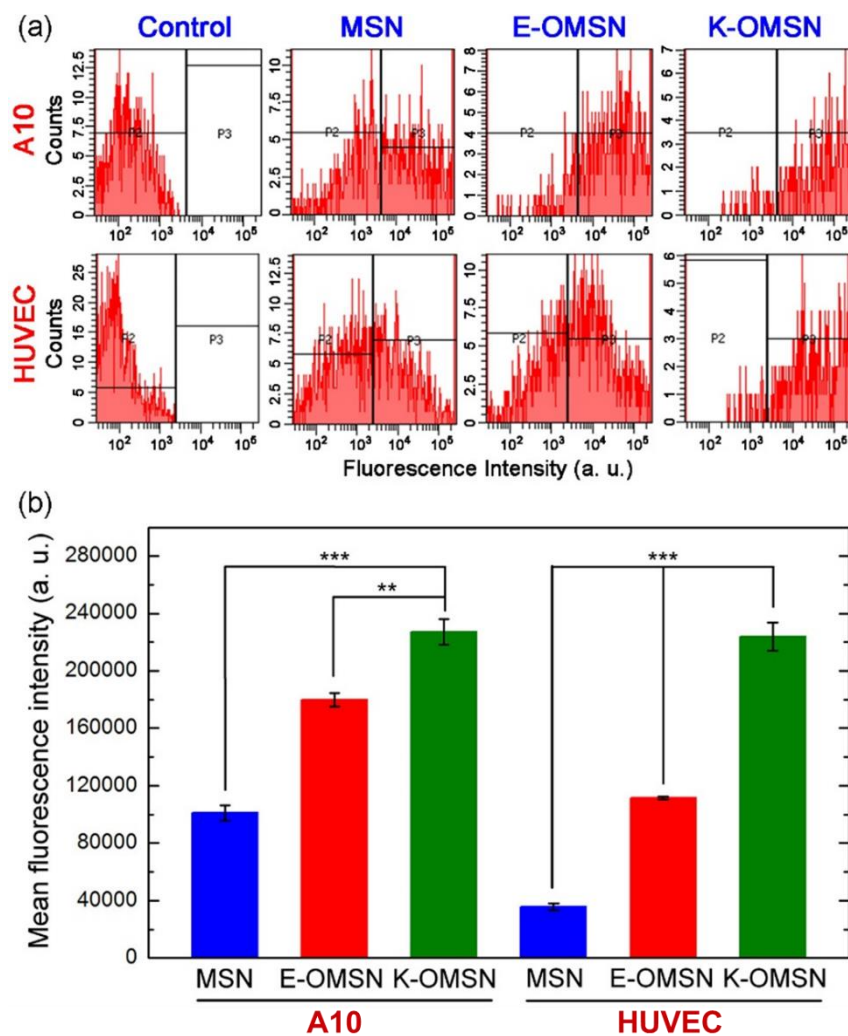
Figure 2.20: Flow cytometry analysis of A10 cells and HUVECs treated with bare and peptide functionalized MSNs. (a) Flow cytometry histograms. (b) Graph demonstrates the improved uptake of peptide functionalized MSNs. Data were generated from at least three independent experiments. According to Student's t-test, **$p < 0.001$ and ***$p < 0.0001$.

Chapter 3

Ultrabright Tri-Functional MSNs with Reduced Non-Specific Toxicity

3.1 Introduction

Recently, ultrabright fluorescent mesoporous silica nanoparticles (MSNs) were prepared by physically entrapping the dye molecules inside nano-channels of MSNs [58-64]. This method enables efficient and facile confinement of dyes inside pores of MSNs. Dye molecules entrapped through their hydrophobic interaction with the surfactant molecules, which are normally used to generate pores and extracted after synthesis to open the pores. For ultrabright MSNs extraction of surfactant molecules results loss of fluorescence due to the extraction of physically entrapped dye molecules. Therefore the particles must be used as they prepared with surfactant molecules. However, it is known that surfactant molecules such as Cetyl trimethylammonium bromide (CTAB) are very toxic to the cells [65, 66]. Cytotoxicity of the ultrabright particles restricts their use in bioimaging. This limitation of CTAB containing MSNs can be turn into a benefit in therapy of cancer due to the high toxicity of CTAB against several cancer cell lines [66]. However, CTAB molecules immediately released from the open pores of MSNs and show non-selective toxicity against both normal and cancer cells. Therefore, new approaches are needed for slow down the release of CTAB molecules from pores of MSNs to develop nanoagents with both diagnosis and therapy capabilities and low non-specific toxicity.

In this context, we prepared silica capped multifunctional MSNs using Rose Bengal (RB) dye as a fluorescent probe and PDT agent and CTAB surfactant as both structure directing and chemotherapy agent (Figure 3.1). Thin silica layer around the particles reduce the CTAB release by closing the mesopores and accordingly decrease the non-specific toxicity of nanoparticles. RB dye encapsulated to the particles through CTAB surfactant molecules and resulting particles are ultrabrightly fluorescent. In addition, RB molecules produces singlet oxygen under illumination of green light which can be used for photodynamic therapy cancer cells.
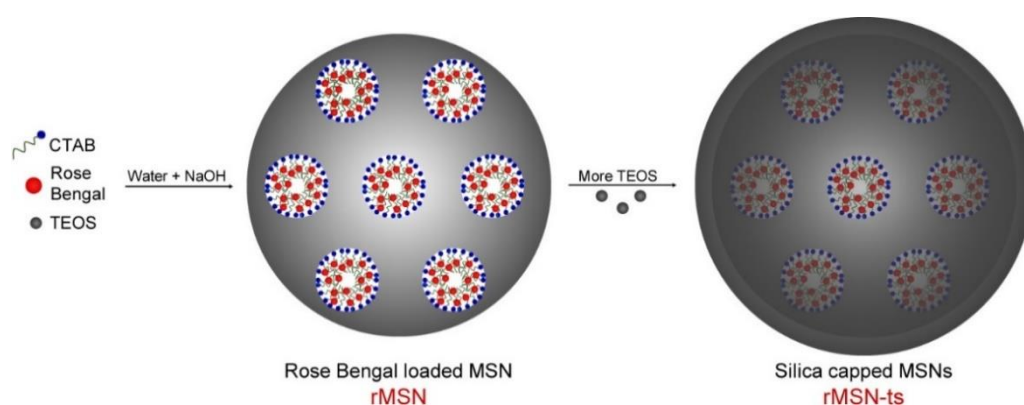
Figure 3.1: Schematic representation of synthesis of silica capped and dye loaded ultrabright MSNs.

First, we showed the improved biocompatibility of silica capped MSNs (rMSN-ts) compared to the uncapped particles (rMSN) using red blood cells (RBCs) and L2929 and MCF7 cell lines. Then, we demonstrated that silica capped particles are more suitable for cancer cell labeling applications with their reduced toxicity and increased cellular uptake using MCF7 cancer cells. Lastly, we studied the *in vitro* photodynamic therapy efficiencies of both capped and uncapped particles.

3.2 Experimental Section

Materials: Cetyltriammoniumbromide (CTAB), F127 pluronic polymer, 3-(Trihydroxysilyl) propyl methylphosphonate (TSPMP), Rose Bengal 3-(4,5-dimethyl-2-thiazolyl)-2,5-diphenyltetrazolium bromide (MTT) were purchased from Sigma

Aldrich (USA). Tetraethyl orthosilicate (TEOS) and Methyltrimethoxysilane (MTMS) were purchased from Merck (Germany). All chemicals were used as purchased.

Preparation of ultrabright MSNs: To synthesize rMSN, 200 mg CTAB and 10 mg of F127 were dissolved in 95 mL of water and 0.8 mL RB solution in water (5 mg/mL) and 0.7 mL of NaOH (2 M) were added to this solution. Then the reaction mixture was heated to 80 °C while stirring vigorously (600 rpm). After temperature fixed at 80 °C, 1 mL of TEOS was rapidly added to the reaction mixture. After 15 min, 60 μL of MTMS was slowly added. After 45 min, 250 μL of TSPMP was slowly added and reaction mixture further stirred for 90 min. Finally, particles were collected by centrifugation at 9000 rpm for 20 min and washed with water twice. To synthesize rMSN-ts, 1 mL of TEOS was slowly added to reaction mixture before TSPMP addition. TSPMP was added 20 min later then second TEOS addition. Other parameters were same with the rMSN synthesis. To extract surfactant and RB molecules from rMSN for control experiments, particles were dispersed in 50 mL of 20 g/L ammonium nitrate solution in ethanol and stirred vigorously at 60 °C for 30 min. This treatment was repeated twice. Then the particles were washed with water twice and dried at 60 °C.

Hemolysis assay: Hemolysis experiments were performed according to a previous report [17]. EDTA stabilized human blood samples were freshly obtained from volunteers at Bilkent University Health Center (Ankara, Turkey). First, 2 mL of blood was centrifuged at 1600 rpm for 5 min and blood plasma and surface layer was removed. Remaining RBC pellet was washed five times with 5 mL of PBS solution and RBCs were diluted in 20 mL of PBS solution. Then, 0.8 mL of nanoparticle solutions or supernatants in PBS at different concentrations were added to 0.2 mL of RBC suspension. Also, positive and negative control samples were prepared by adding 0.8 mL of water and PBS, respectively to 0.2 mL of RBC solution. Then, samples were incubated at 25 °C for 2 h. The samples were slightly shaken once for every 30 min to resuspend the RBCs and MSNs. After 2 h, samples were centrifuged at 1600 rpm and 150 μL of supernatants was transferred to a 96-well plate. Absorbance of hemoglobin in supernatants was measured with a microplate reader at 570 nm. Also, absorbance at 655 nm was recorded as reference. Percent hemolysis values were calculated from

three separate experiments. A Student's t-test was applied to all data sets and the difference between them accepted to be statistically significant when $p < 0.05$.

Cell culture: Human breast adenocarcinoma cells (MCF-7) and murine fibroblast cells (L2929) were grown to confluence at 37 °C under 5% CO_2 in Dulbecco's Modified Eagle Serum (DMEM) containing 1% penicillin/streptomycin, 10% fetal bovine serum (FBS) and 2 mM L-glutamine.

Cell viability tests: 10^4 cells/well were seeded to 96-well plates for both cell lines. After overnight of culture, MSNs in 11 µL of PBS were added to the wells to give final nanoparticle concentrations between 10 and 200 µg/mL. Then the cells were incubated for 4, 24 or 72 h. The cytotoxicity of particles was determined by the MTT reduction assay. First MSN containing medium was removed and 100 µL of fresh medium was gently added. Then filter-sterilized 20 µL of MTT reagent (5 mg/mL in PBS) was added to each well, and the plates were incubated for 4 h at 37 °C. After incubation, medium was removed and the precipitated formazan crystals were dissolved by adding acidic IPA. Optical density of dissolved formazan crystals was measured at 570 and 655 nm using a microplate reader. The optical density of wells containing untreated cells was considered as 100%. All the experiments were performed in triplicate.

Fluorescence microscopy: 5×10^4 MCF7 cells/well were seeded to 24-well plates and cultured for 48 h. After culture, nanoparticles in 55 µL of PBS were added to the wells to give final nanoparticle concentrations of 100 µg/mL. After 4h of incubation, nanoparticle containing mediums were removed, cells were washed with PBS three times. Finally, optical and fluorescence images of cells were taken in PBS.

PDT experiments: 10^4 MCF7 cells/well were seeded to 96-well plates and cultured for 48 h. After culture, nanoparticles in 11 µL of PBS were added to the wells to give final nanoparticle concentrations of 100 µg/mL. After 4h of incubation, nanoparticle containing mediums were removed, cells were washed with PBS, fresh medium was added and cells were further incubated for 16 h. Then, cells were illuminated with a 5 mV green laser for 30 s and incubated for 1 h. Finally, cell viabilities were determined using a MTT assay.

Characterization: Transmission electron microscopy (TEM) images were taken using a Tecnai G2 F30 (FEI) microscope. Zeta potentials of nanoparticles were measured with Zetasizer Nanoseries (Malvern Instruments). Optical absorption

measurements in cytotoxicity and hemolysis assays were carried out using a Microplate reader (Spectramax M5, Molecular Devices). Absorption spectra of nanoparticles were recorded using a UV-Vis absorption (Cary 100, Varian) spectrophotometer. Fluorescence spectra of the nanoparticles were recorded by a Fluorescence Spectrophotometer (Eclipse, Varian).

3.3 Synthesis and Characterization of Ultrabright Fluorescent MSNs

Synthesis steps of RB containing uncapped and silica capped MSNs are outlined in Figure 3.1. RB loaded surfactant containing MSNs (named as rMSN) were prepared using the surfactant (CTAB) assistant loading method. To cap the pores of rMSN, excess silica precursor (TEOS) was added after the formation of rMSN in a one-pot reaction, which yields a thin and uniform silica shell around the particles. The silica capped particles were named as rMSN-ts. Also, a surfactant-free MSN (rMSN-ex) was prepared by extracting the CTAB -and accordingly the encapsulated RB- of rMSN for control experiments.

Figure 3.2 shows the TEM images of the rMSN and rMSN-ts which have fairly monodisperse particle size distribution with a short rod-like shape. Close up TEM image of rMSN (Figure 3.2a, the column) shows the hexagonally ordered mesostructure of these particles. Formation of a uniform silica shell (~8.5 nm) around the rMSN-ts can be easily observed from Figure 3.2b. Importantly, silica capping process did not cause a significant change in the morphology of the particles; hexagonally ordered mesostructured core was still observable. Particle length, width and aspect ratio of the particles were summarized in the Table 3.1. As expected, length and width of the particles slightly increased after formation of the silica shell. Also, aspect ratio was slightly decreased after silica shell formation due to the uniform size increase in both directions.
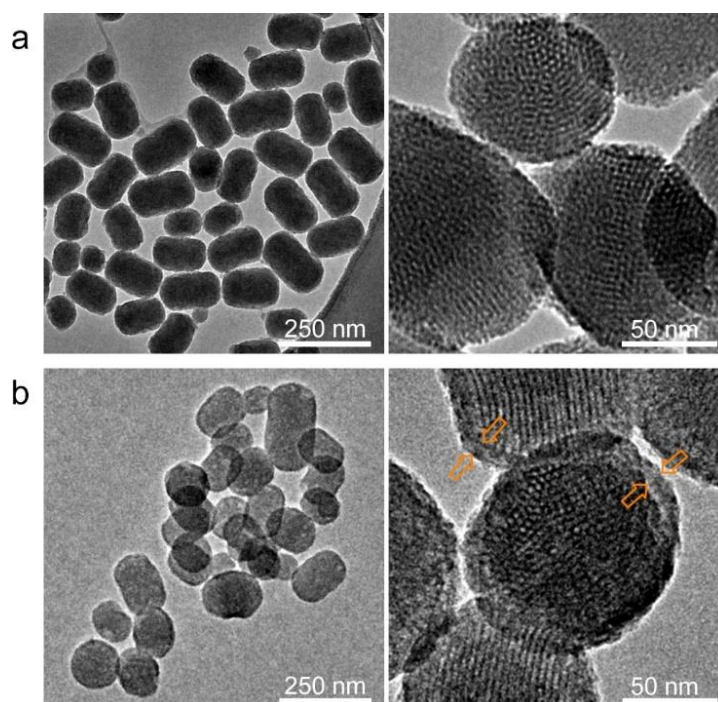
Figure 3.2: TEM images of the ultrabright MSNs; (a) rMSN and (b) rMSN-ts. Left and right panels shows the low and high magnification images of the particles, respectively. Both particles have short rod-like shape and fairly monodisperse in size. Uniform silica layer around rMSN-ts can be easily observed from the images. Orange arrows in (b) indicate the nonporous shells formed around the porous cores of rMSN-ts.

Sample	CTAB exchange	Aspect ratio	Length (nm)	Width (nm)	Shell Thickness (nm)	RB content (mg/g)	Zeta Potential in PBS (mV)
rMSN	no	1.38	119 ± 30	86 ± 14	N/A	8.6	3.3 ± 0.9
rMSN-ts	no	1.29	133 ± 27	103 ± 15	8.4 ± 1.5	5.1	-13.1 ± 0.2
rMSN-ex	yes	1.38	119 ± 30	86 ± 14	N/A	N/A	-6.3 ± 0.3

Table 3.1: Physical properties of ultrabright MSNs.

To determine the RB content of nanocarriers, we extracted encapsulated RB molecules using ethanol and measured the absorption spectra of the extracted RB.

Accordingly, dye contents were calculated to be 8.6 and 5.1 mg/g of MSN for rMSN and rMSN-ts, respectively (Table 3.1). The lower RB content of rMSN-ts is due to the formation of dye-free shell after second TEOS addition, which decreases the dye amount per gram of silica. However, it can be assumed that core of the rMSN-ts contains approximately same amount of RB with rMSN since the synthesis conditions are the same. It should be noted that, the alcohols like ethanol can penetrate into the hydrophobic cores of CTAB micelles, where they can easily dissolve and extract the RB molecules. On the other hand, water cannot penetrate into the hydrophobic micelles and RB molecules stay in the pores in aqueous media.

3.4   Optical Properties of Ultrabright Fluorescent MSNs

Optical properties of the ultrabright particles were studied and compared with free RB molecules at same dye concentration. Figure 3.3a reveals that the absorption maxima of rose Bengal (RB) molecules confined in the pores of rMSN and rMSN-ts were approximately 10 nm red shifted compared to the free RB molecules, which may be due to the interactions between close proximity RB molecules inside the nanochannels and also the absence of water molecules in the hydrophobic cores of CTAB micelles. Similarly, we observed a red shift of around 15 nm in the fluorescence spectra of both rMSN and rMSN-ts (Figure 3.3b).

To explore the brightness of particles, we collected the fluorescence spectra of particles and free RB molecules at same dye concentration (5 µg/mL) and at various excitation wavelengths. Figure 3.3c clearly shows that when the RB molecules are confined in the pores of MSNs their fluorescence enhanced up to 20 fold. It is important to note that rMSN and rMSN-ts demonstrated almost same fluorescence intensity at all excitation wavelengths indicating that the silica capping process has no effect on the fluorescence of the particles. In addition, for better visualization we produced a 2D color map showing the fluorescence intensity of free RB and rMSN-ts depending on the excitation wavelength (Figure 3.4). At the same fluorescence scale, fluorescence of free RB was hardly distinguishable from the background. On the other hand, strong fluorescence of rMSN-ts was clearly observable.
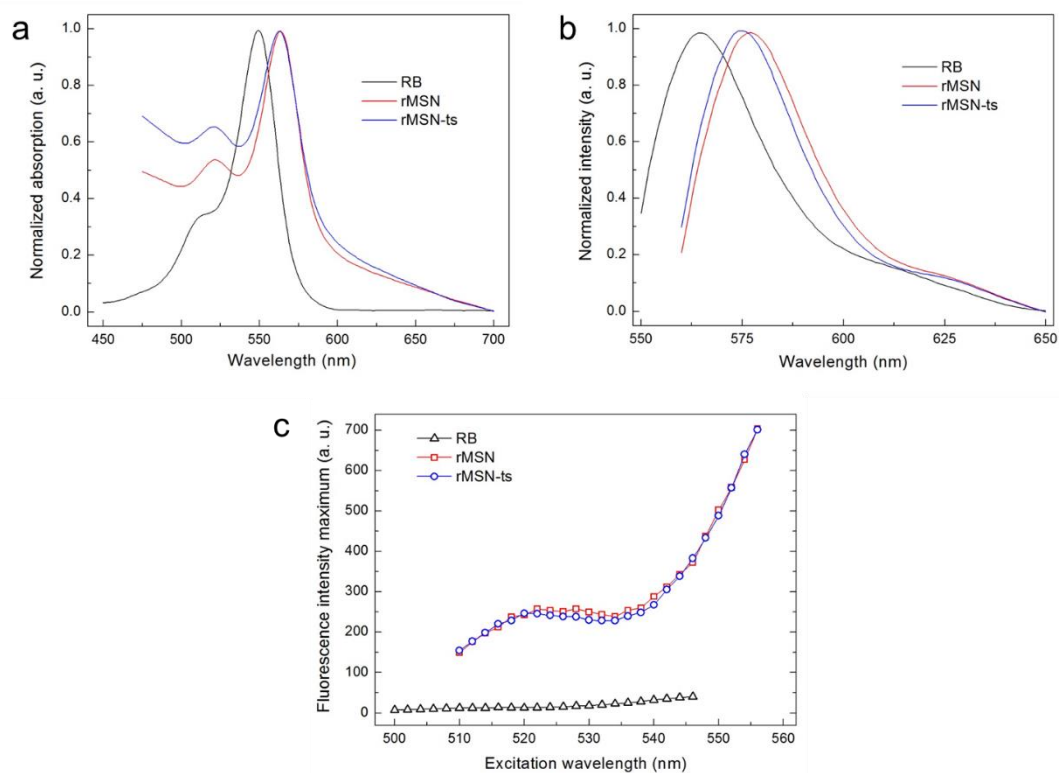
Figure 3.3: (a) Normalized UV-Vis spectra of free RB molecules and ultrabright particles, (b) Normalized fluorescence spectra of free RB molecules and ultrabright particles, (c) Fluorescence maxima of free RB molecules and ultrabright particles at different excitation wavelength.
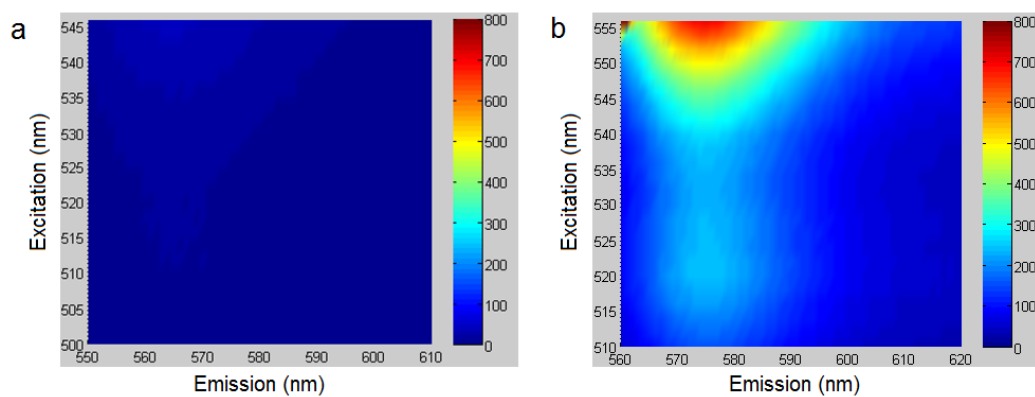
Figure 3.4: 2D color maps showing the excitation wavelength dependent fluorescence intensities of (a) free RB molecules and (b) rMSN-ts at same dye concentration.

3.5 Hemolytic Activity of Ultrabright Fluorescent MSNs

A hemolysis assay was used to determine the toxicity of ultrabright MSNs on red blood cells (RBCs) [17]. 0.2 mL of isolated RBCs were mixed with 0.8 mL of nanoparticles in PBS to give desired MSN concentration, at a range of 10 to 200 µg/mL, and incubated at 25 ℃ for 2 hours. Figure 3.5a shows the concentration dependent hemolytic activity of the ultrabright MSNs. rMSN demonstrated a high hemolytic activity; at 200 µg/mL 35.8% and at 100 µg/mL 7.1% of RBCs were hemolyzed. Capping the particles with a thin silica layer drastically decreased the hemolytic activity; rMSN-ts showed low hemolytic activity of 3.1% and 1.4% at 200 and 100 µg/mL concentrations, respectively. In addition, hemolytic activity of the rMSN was investigated after surfactant extraction (Figure 3.5a). rMSN did not reveal any detectable hemolysis of RBCs in the studied concentration region after surfactant extraction due to the phosphonate functional group on its surface (see Chapter 6 for more detailed information on hemolytic activity of phosphonate modified MSNs).

In order to further investigate the origin of the hemolytic activity of ultrabright MSNs, we also incubated the RBCs with the supernatants of rMSN and rMSN-ts which are incubated in PBS for 2 h (Figure 3.5b). It is well known that released surfactant molecules (CTAB) can cause hemolysis [17]. However, we did not observe any supernatant originated hemolytic activity at either low (25 µg/mL) or high particle (200 µg/mL) concentrations. These results revealed that the hemolytic activity of the ultrabright MSNs is related with the surface immobilized CTAB molecules which is positively charged and may strongly interact with the RBC membrane. Capping the particles with a thin silica layer significantly reduce the hemolytic activity of ultrabright MSNs by preventing the interactions between positively charged CTAB surfactant molecules and RBC membrane.
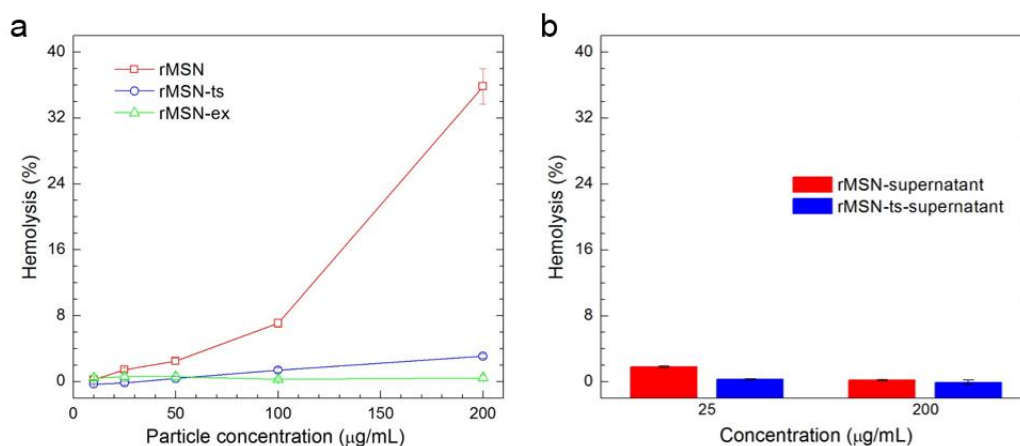
Figure 3.5: (a) Hemolytic activity of ultrabright and extracted MSNs. (b) Hemolytic activity of supernatants of ultrabright particles.

3.6 Cytotoxicity of Ultrabright Fluorescent MSNs

Cytotoxic effects of surfactant containing MSNs were studied using two different cell lines; as normal and cancer cells, we used murine fibroblast L2929 and MCF-7 human breast cancer cell lines, respectively. Figure 3.6 shows the 3-(4,5-dimethylthiazol-2-yl)-2,5-diphenyl-tetrazolium bromide (MTT) results for both cell lines after short (4 h), moderate (24 h) and long (72 h) incubation with rMSN, rMSN-ts and rMSN-ex in the particle concentration range of 10 to 200 µg/mL. rMSN showed immediate toxicity against both cell lines; even after 4 h of incubation cell viabilities were significantly reduced. This extreme toxicity of rMSN is due to the release of toxic CTAB surfactant from the open pores of the particles [67]. On the other hand, a delayed toxicity profile was observed for rMSN-ts for both cell lines thanks to the slow release of CTAB molecules from silica capped pores. After 4 h, no cytotoxicity was observed even at the high particle concentration of 200 µg/mL, which makes the rMSN-ts suitable for cell labelling applications. After 24 h of incubation, rMSN-ts was decreased the viability of both cell lines especially at high particle concentrations, yet cellular viabilities are larger for rMSN-ts than rMSN for all cases. After 72 h, both rMSN and rMSN-ts largely reduced to the cell viabilities around 10% for both cell lines. We also studied the effect of surfactant extracted particles (rMSN-ex) on cell viability as negative control of CTAB induced cytotoxicity. We observed that rMSN-

40

ex decreased the cellular viability at only high particle concentrations after especially 72 h of incubation which may be due to the intrinsic toxicity of this mesoporous silica material or the residual CTAB molecules remained in the particles after surfactant extraction. This also indicates that the cytotoxicity of ultrabright MSNs mainly originated from the CTAB molecules adsorbed in the pores. In addition, it should be noted that for all cases toxicity of particles against cancer cell is larger than that of normal cells.
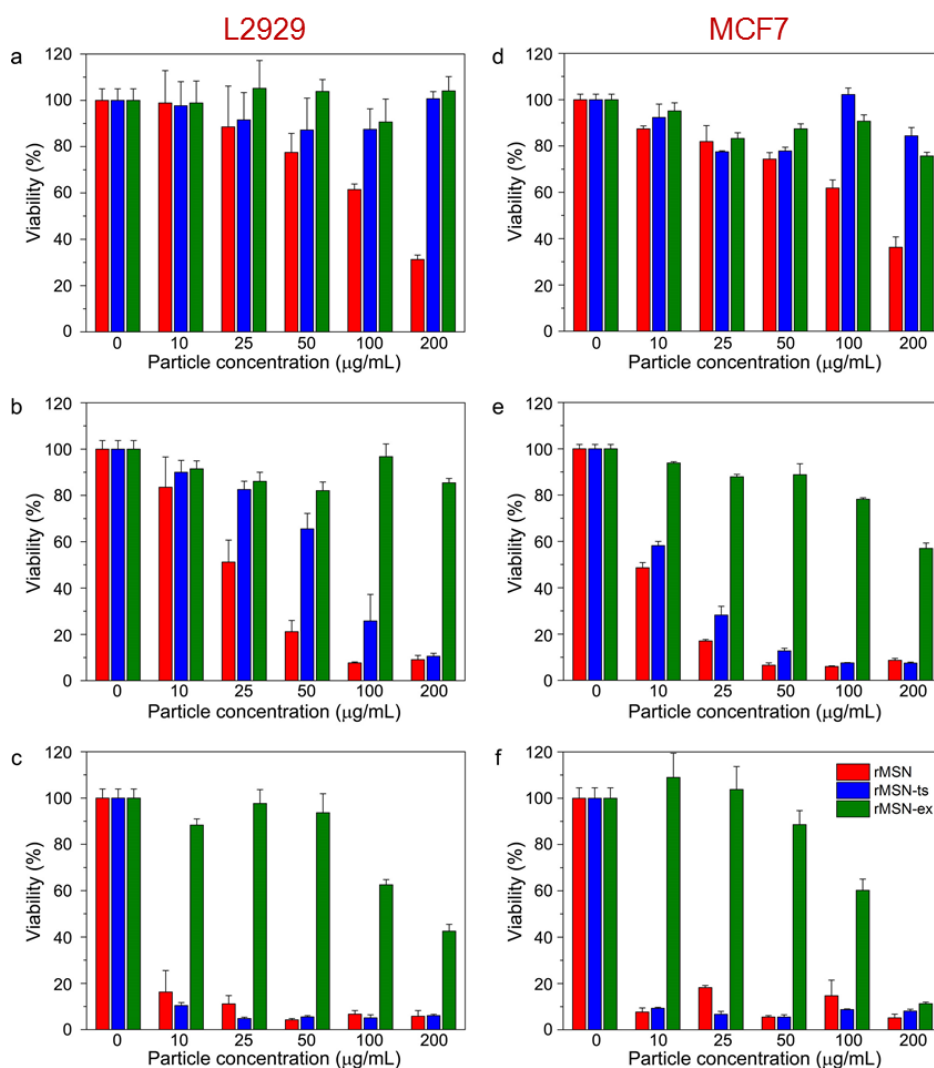
Figure 3.6: Cytotoxicity results of ultrabright MSNs against normal (L2929) and cancer (MCF7) cell lines. (a-c) viability of L2929 cells after (a) 4 h, (b) 24 h and (c) 72 h of incubation with particles. (d-f) viability of MCF7 cells after (d) 4 h, (e) 24 h and (f) 72 h of incubation with particles.

41

3.7   Fluorescent Imaging with Ultrabright MSNs

Figure 3.7 shows the fluorescence and bright field optical microscope images of the MCF7 cells that were incubated or not incubated with ultrabright MSNs for 4 h. Less fluorescence was observed for rMSN compared to the rMSN-ts indicating that rMSN-ts was more effectively uptaken by MCF7 cells. Also, the fluorescence signal of rMSN mainly concentrated on the edges of the cells showing that most of the positively charged rMSNs attached to the cell membrane instead of uptaken by the cells. On the other hand, fluorescence signal homogeneously distributed inside the cells for rMSN-ts indicating that the particles were uptaken by the cells and dispersed in the cytoplasm of the cells.
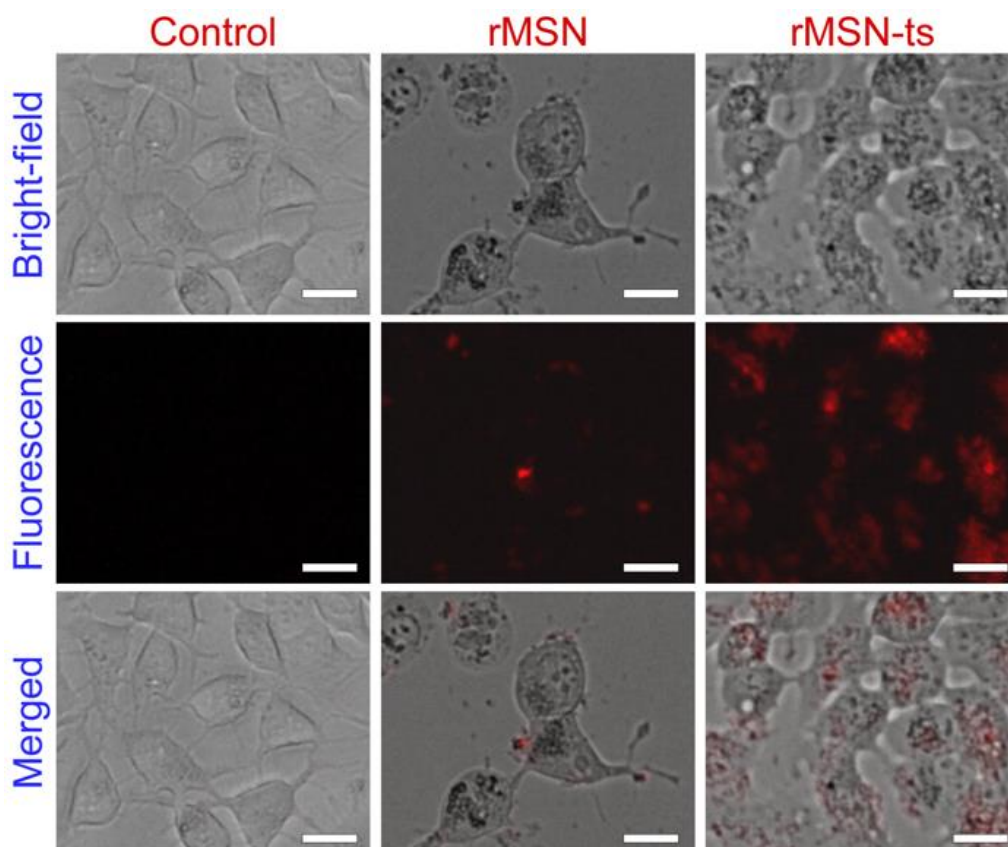
Figure 3.7: Fluorescence, bright field and merged images of MCF7 cells untreated or treated with 100 µg/mL of particles for 4 h. rMSN-ts revealed significantly higher cellular uptake compared to rMSN. Scale bars: 20 µm.

3.8 Phototoxicity of Ultrabright MSNs

In addition to their chemotoxicity, ultrabright MSNs are expected to be phototoxic to the cells because RB is a well-known photosensitizer that produces singlet oxygen when illuminated with green light [68]. Therefore we investigated the phototoxicity of ultrabright MSNs using MCF7 cells (Figure 3.8). We first incubated the cell with particles for 4 h at the 100 µg/mL of particle concentration and then we removed the particle containing medium and further incubated the cells for 16 h in a particle-free medium. After incubation, we illuminated half of the wells with a green laser (5 mV) for 30 s and other half not. In the absence of light both rMSN and rMSN-ts reduced the viability of MCF7 cells due to their chemotoxicity which is proved in the previous section. Also, as expected more reduction in cell viability was observed for rMSN. In the presence of light, the cell viabilities were further reduced to around 20%. The photo-induced reduction in the viability was more pronounced for rMSN-ts than rMSN which may be due to its higher uptake capacity by MCF7 cells. These results indicates that rMSN-ts is very promising for synergetic chemo- and photodynamic- therapy of cancer with reduced toxicity to normal cells and RBCs.
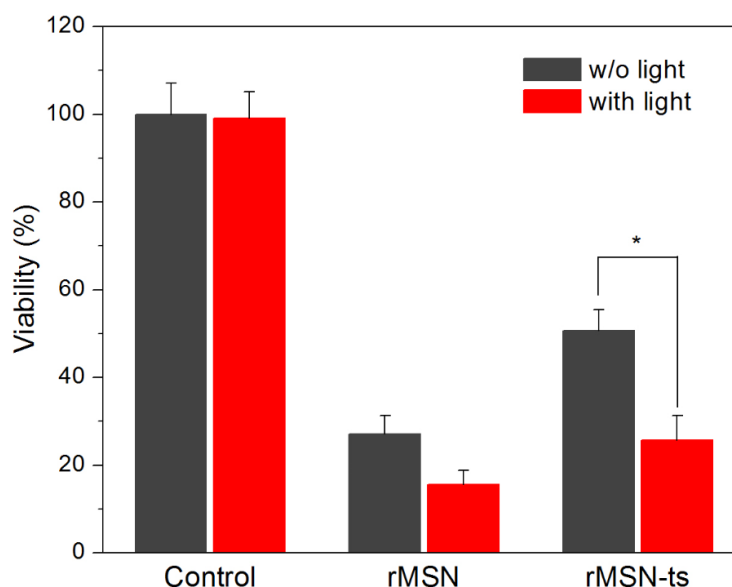
Figure 3.8: Photodynamic therapy results of MCF7 cells. Viability of the cells treated with 100 µg/mL of particles for 4 h after illuminated or not illuminated with a green laser for 30 s. * indicates p <0.05 according to the student's t-test.

Chapter 4

Nanoconfinement of Pyrene in MSNs for Detection of Trace TNT in Aqueous Phase

4.1 Introduction

Contamination of water resources by nitroaromatic explosives, particularly trinitrotoluene (TNT), is a major global concern since these molecules are highly toxic to the biological organisms [69, 70]. Therefore, sensitive and selective detection of nitroaromatic explosives in water has attracted a great deal of interest in recent years [71, 72]. Currently employed methods for their detection include ion mobility spectroscopy (IMS), mass spectrometry, gas chromatography (GC), and infrared absorption spectroscopy [73-76]. Although these methods are usually sensitive, they are limited by their time-consuming and complicated procedures and costly and bulky instrumentation [75]. In this context, fluorescence based sensors are very promising for the development of cost-effective and portable explosive sensing devices with high sensitivity and selectivity [71, 72]. For instance, using quantum dots [77-79] fluorescent dyes, [80-82] metal organic frameworks (MOFs), [83-85] and conjugated polymers [86-89] nitroaromatic molecules were detected in aqueous phase. However, these methods generally have some drawbacks such as high detection limit, interference from non-nitroaromatic compounds, laborious and costly synthesis and poor stability of fluorescent probes in the atmospheric conditions. Therefore, facile

and cost-effective development of robust nitro-explosive sensing platforms with good sensitivity and selectivity is still needed.

In this context, we report the preparation of pyrene confined MSNs for rapid and reliable detection of TNT in water. It is well known that fluorescence of pyrene (a π-conjugated fluorophore with high quantum yield and long life time) is quenched by nitroaromatic explosives through photoinduced electron transfer (PET) [90, 91]. Particularly, excimer emission of pyrene, which is observed in the presence of π-π^* stacking interaction between excited and ground state pyrene molecules, is very sensitive towards nitroaromatics. Recently, we and others used pyrene excimer fluorescence for the detection of nitroaromatic molecules utilizing nanomaterials that contains chemically attached or more simply physically encapsulated pyrene molecules [82, 92-100]. However, most of these studies aimed to detect nitroaromatic explosives in vapor phase or in organic solvents and studies for the determination of nitroaromatic explosive contaminated water is very rare [94-97]. In addition, for the materials with pyrene excimer emission, the detection limit in aqueous phase is generally poor (at μM level). Herein, we demonstrated the trace (nM level) detection of TNT in aqueous phase using pyrene confined MSNs. In order to confine pyrene molecules in MSNs, we firstly dissolved hydrophobic pyrene molecules in water using cetyltriamonium bromide (CTAB) surfactant. Pyrene molecules were encapsulated in the hydrophobic inner parts of the rod-shaped surfactant micelles. Then, we polymerized a silica precursor (tetraethyl orthosilicate; TEOS) around these micelles in basic conditions to obtain organic/inorganic hybrid nanoparticles that contain confined pyrene molecules inside their 2-3 nm sized mesostructures. Nano-confinement of pyrene inside these mesostructures resulted in a bright and visible excimer emission. Recently, we reported that excimer emission of the pyrene doped materials can easily diminish overtime due to the dissociation of close proximity pyrene molecules [92]. To our surprise, we observed that pyrene excimer emission of these hybrid nanoparticles is stable for at least six months.

We studied TNT sensing performance of the nanoparticles in water for TNT concentration varying from 10 nM to 10 μM based on quenching of excimer emission. We observed that the quenching of excimer emission is very selective and sensitive to TNT. In addition, emission quenching can be visually observed under UV-light

enabling the naked-eye detection of TNT contaminated water. Pyrene confined MSNs with their easy synthesis, high stability, high sensitivity and cost-effectiveness can be potentially used for the detection of TNT contaminated water.

This work published on the Nanoscale (2014, *6*, 15203-15209) journal. Reproduced with permission from The Royal Society of Chemistry.

4.2 Experimental Section

Materials: Tetraethyl orthosilicate (TEOS), chloroform, and sodium hydroxide were purchased from Merck (Germany). Pluronic® F127, cetyltrimethylammoniumbromide (CTAB) and pyrene were purchased from Sigma-Aldrich (USA). All chemicals were used as received without any purification.

Synthesis of pyrene confined MSNs: Pyrene confined MSNs (pMSNs) were synthesized by slightly modifying previous methods [46, 54, 101]. Certain amount of pyrene (6, 12, 22, and 40 mg) was dissolved in 500 μL of chloroform and 200 mg of CTAB was dissolved in 30 mL of deionized water. Then, pyrene solution was added to the CTAB solution and the mixture was stirred at 60 °C for 20 min. During stirring, chloroform evaporated and pyrene homogeneously dispersed in the CTAB solution. For the reaction mixture, 20 mg of F127 was dissolved in 66 mL of deionized water and 0.7 mL of 2.0 M sodium hydroxide solution was added. CTAB solution was added to the reaction mixture, and the mixture was heated to 80 °C. Then, 1 mL of TEOS was rapidly added under stirring at 600 rpm. The reaction mixture was refluxed for 2 h. Finally, particles were collected by centrifugation at 9000 rpm for 20 min and washed with deionized water twice. Then, particles were dispersed in 80 mL of deionized water. Final particle concentration in the dispersion was 5.1 mg/mL.

Characterization of nanoparticles: Structure of pMSNs was investigated with transmission electron microscope (TEM) (Tecnai G2-F30, FEI) and scanning electron microscope (SEM) (Quanta 200 FEG, FEI). Absorption spectrum of pMSNs was recorded with UV-Visible spectrophotometer (Cary 100, Varian). Fluorescence spectra of pMSNs were recorded with fluorescence spectrophotometer (Eclipse, Varian). Size distribution of the nanoparticles were analysed using a zetasizer (Malvern Instruments).

Fluorescence quenching experiments: Fluorescence quenching based sensing experiments were performed in a quartz cuvette. 3 mL of 0.02 mg/mL pMSNs dispersion were used for each sensing measurement. Fluorescence spectrum of pMSNs dispersion was recorded before analyte addition (excitation wavelength was 340 nm). Then, TNT aqueous solutions were added in order to adjust the TNT concentrations between 10 nM and 10 μM and then, fluorescence spectrum of the dispersion was recorded again. Selectivity experiments were performed using aqueous solutions of trinitrotoluene, dinitrotoluene, nitrobenzene, benzoic acid, aniline, chloroform, methanol, hydrochloric acid, sodium hydroxide, and sodium chloride. Final concentration of all interfering analytes was 10.0 μM in the fluorescence assay.

4.3 Synthesis and Characterization of Pyrene Confined MSNs

Pyrene confined MSNs (pMSNs) were synthesized via polymerization of TEOS monomer in the presence of CTAB surfactant under basic conditions. Basic condition prevents the complete hydration of TEOS and increases the residual ethoxy groups to promote the self-assembly of negatively charged silicates with positively charged cetyltrimethylammonium (CTA) micelles [47, 102]. Therefore, the ordered mesostructure formed through the self-assembly of CTA micelles and silicates. Pyrene was added to the reaction mixture before the polymerization of silica and encapsulated by the hydrophobic parts of the CTA micelles (Figure 4.1). Therefore, CTA micelles performed as both the templating agent for the formation of mesostructures and nanocontainers for pyrene confinement. In addition, we used a second surfactant (a pluronic block copolymer; F127) in order to prevent particle aggregation during the synthesis and to provide the particles colloidal stability. (Figure 4.1).
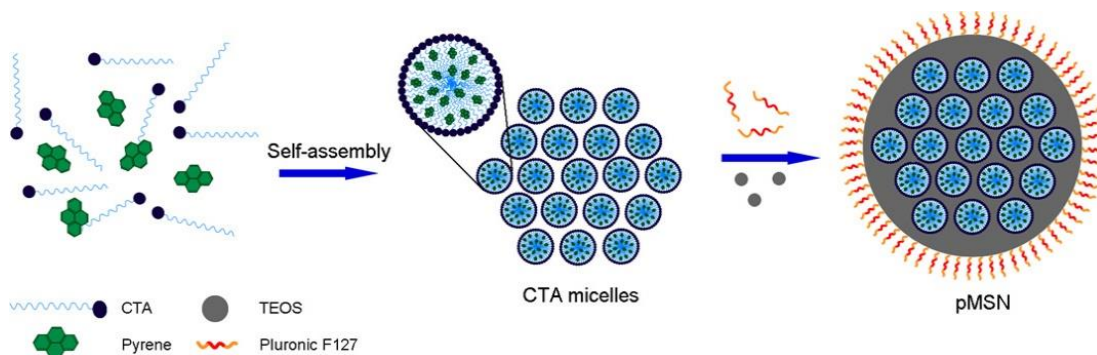
Figure 4.1: Schematic representation for the formation of pMSNs. Pyrene is confined in CTA micelles through hydrophobic-hydrophobic interactions. After the addition of TEOS, silica grows around the self-assembled pyrene confined CTA micelles. F127 pluronic polymer prevents particle aggregation during the silica growth.

Fig. 2 shows TEM and SEM images of the pMSNs prepared using 40 mg of pyrene. pMSNs have mesostructures with sizes of approximately 2-3 nm. pMSNs are spherical in shape and their average particle size is 74 ± 9 nm (Figure 4.2a). Also, particle size distribution of pMSNs is fairly narrow (Figure 4.2b). In addition, we synthesized pMSNs using different amounts of pyrene; 6, 12, and 22 mg. We observed that pyrene concentration significantly affects the size and shape of the silica nanoparticles. For instance, pMSNs prepared using 6 and 22 mg of pyrene have rod-like shapes with high polydispersity. Furthermore, pMSNs prepared using 12 mg of pyrene were interconnected during the synthesis which may cause poor colloidal stability in water (Figure 4.3).
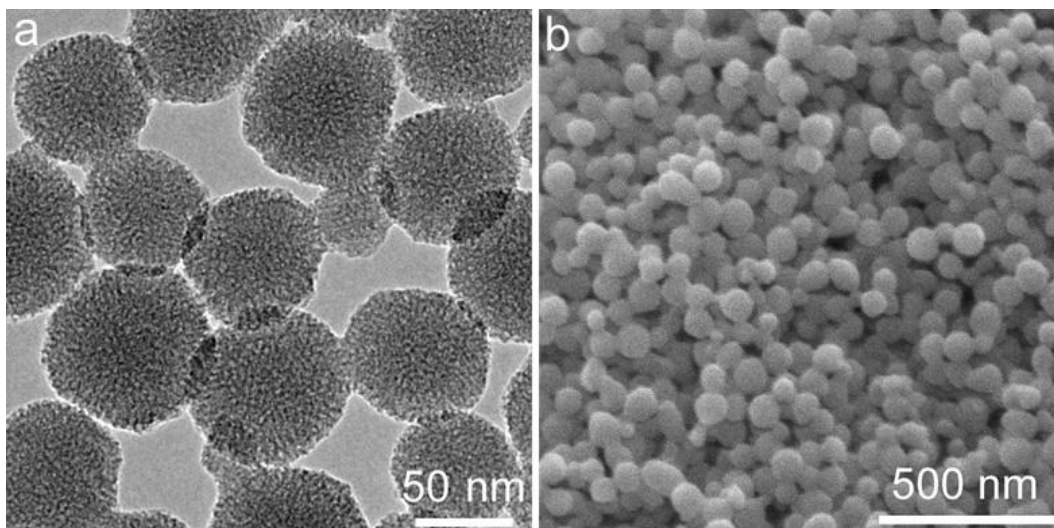
Figure 4.2: Morphology of pMSNs. (a) TEM, and (b) SEM images of the pMSNs prepared using 40 mg of pyrene indicating the uniform size and shape distribution of the nanoparticles.
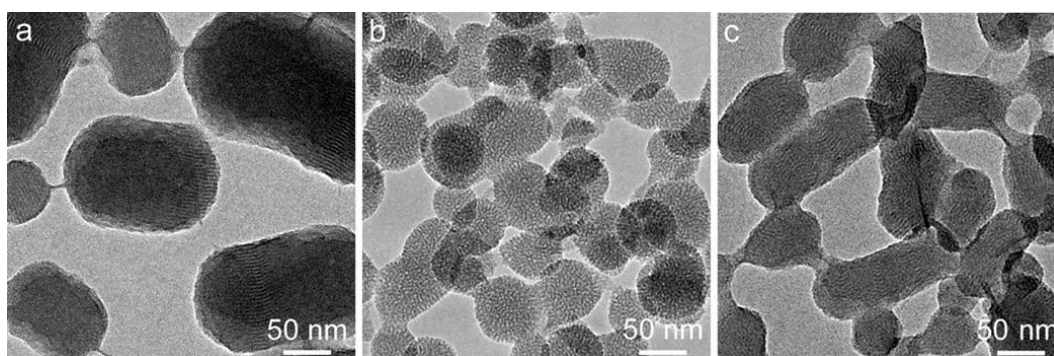
Figure 4.3: TEM images of pMSNs prepared using (a) 6 mg, (b) 12 mg, and (c) 22 mg of pyrene.

Figure 4.4 shows the UV-Visible absorption and fluorescence spectra of pMSNs prepared using 40 mg of pyrene. Three individual peaks at 304, 321, and 336 nm in the UV-Vis spectrum are the absorption bands of pyrene. The emission bands around 370-400 nm in the fluorescence spectrum correspond to the monomer emission which is formed by the relaxation of singlet excited pyrene [103]. The broad emission peak centered at 475 nm, on the other hand, is the excimer emission that occurs when an excited state pyrene makes π-π* stacking interaction with a ground state pyrene. High excimer emission intensity to monomer emission intensity (I_{exc}/I_{mon}) ratio (2.2) was observed for these nanoparticles (calculated using the intensities at 394 nm and 475

nm for monomer and excimer emission, respectively). I_{exc}/I_{mon} ratios were determined to be 0.4, 0.8, and 1.8, for the pMSNs prepared using 6 mg, 12 mg, and 22 mg of pyrene, respectively (Figure 4.5). Since more pyrene molecules form more dimers through π-interaction, excimer emission intensity and I_{exc}/I_{mon} ratios increased with increasing pyrene concentration. Accordingly, we used pMSNs prepared using 40 mg of pyrene in the rest of the study owing to their more uniformly distributed particle size and higher I_{exc}/I_{mon} ratio.
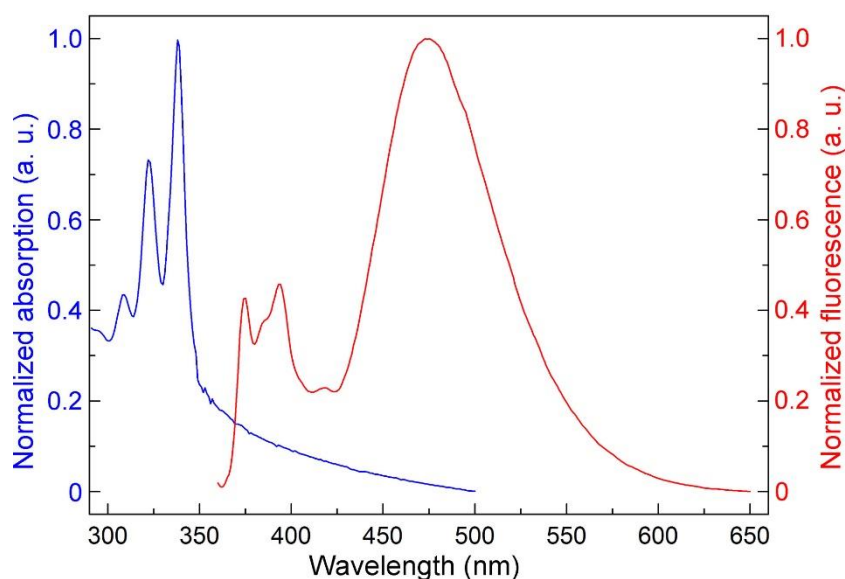
Figure 4.4: UV-Vis absorption spectrum (blue) and fluorescence emission spectrum (red) (excitation wavelength was 340 nm) of pMSNs prepared using 40 mg of pyrene. Three peaks observed at 304, 321, and 336 nm are the absorption bands of pyrene. The peaks at 370-400 nm are the monomer emission of pyrene. The broad emission band centered at 475 nm is the excimer emission.
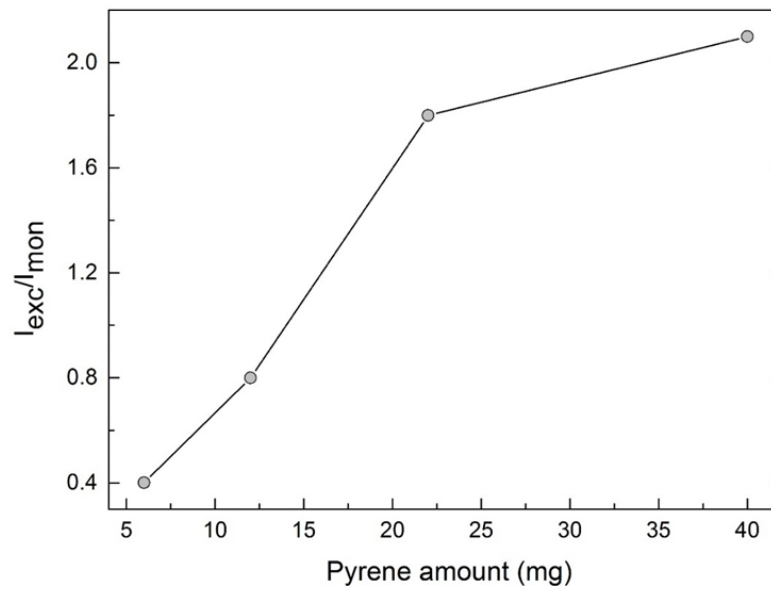
Figure 4.5: I_{exc}/I_{mon} ratios of pMSNs prepared using various amounts of pyrene.

To determine the amount of pyrene that was encapsulated in pMSNs, we extracted pyrene using tetrahydrofuran (THF) and measured the absorbance of the extracted pyrene using a UV-Visible absorption spectrophotometer. Pyrene content in the particles was calculated to be 0.038 mg/mg of pMSNs. Considering that the total amount of synthesized pMSNs was 410 mg, it can be calculated that almost 40% of pyrene used in the synthesis was encapsulated in the nanoparticles. Leakage of pyrene from CTA micelles of the mesostructured silica may cause decay of the excimer emission due to decreasing pyrene concentration in the pMSNs. To check the confinement stability of pyrene in the mesostructure, we centrifuged the pMSNs dispersion (stored for six months at ambient conditions) and measured the emission of the supernatant. There was almost no emission signal in the supernatant indicating the stability of pyrene confined micelles inside the MSNs (Figure 4.6). More importantly, after six months, pMSNs exhibited a bright excimer emission similar to that of the as-prepared particles (Figure 4.7). Also, I_{exc}/I_{mon} ratio of the stored pMSNs was calculated to be 2.0 suggesting the long-term storability of these nanoparticles (Figure 4.7, inset).
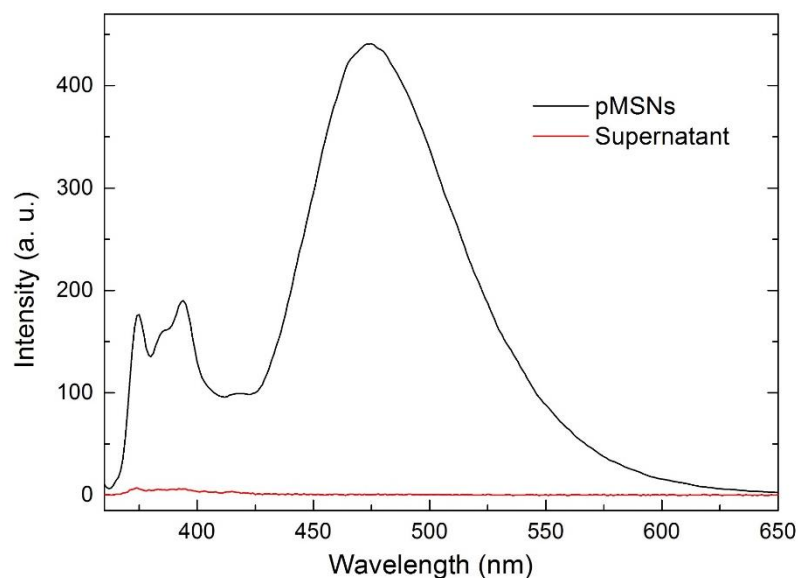
Figure 4.6: Fluorescence spectra of pMSNs (black) and supernatant (red) of pMSNs which was obtained after centrifuging the pMSNs.
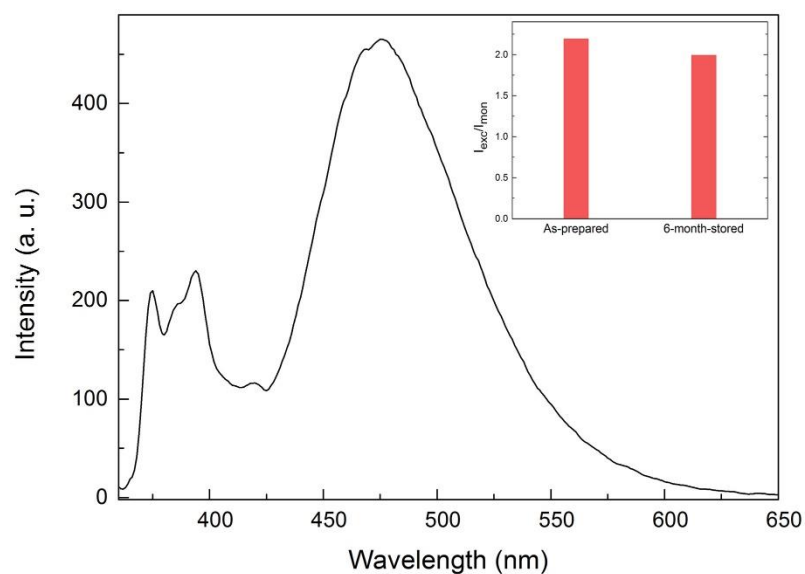
Figure 4.7: Fluorescence spectrum of pMSNs which was stored for six months at ambient conditions. Inset shows the I_{exc}/I_{mon} ratios of as-prepared and stored pMSNs.

Particle size distribution of pMSNs in water was determined using dynamic light scattering (DLS) technique. Average particle size was measured as 84.8 nm (Figure 4.8), which is very close to the size calculated from the TEM images, indicating the good dispersibility of the nanoparticles in water. Besides of dispersibility, colloidal

stability of the nanoparticles is very important for reliable and repeatable fluorescence measurements. To investigate the stability of the particles, we measured the time-dependent size distribution of the pMSNs. Average particle size remained almost constant for at least 1.5 h which is far longer than the duration of a single sensing measurement (Figure 4.8, inset).
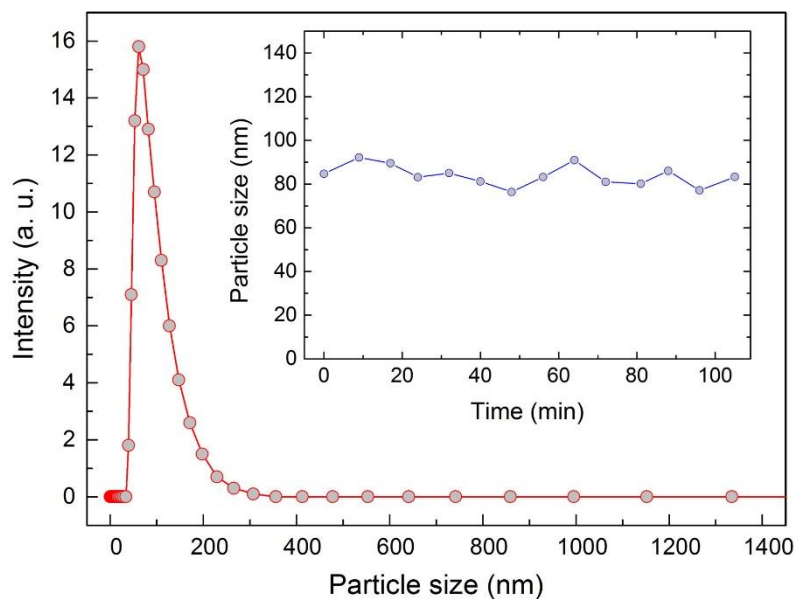
Figure 4.8: Particle size distribution of the pMSNs measured using dynamic light scattering technique. Inset shows the average particle size of pMSNs with respect to time.

4.4 TNT Sensing Performance of the pMSNs

pMSNs exhibit strong excimer emission in the absence of TNT molecules. When TNT binds to pyrene through π-π* interaction, emission of pyrene is quenched through photoinduced electron transfer (PET) from excited pyrene molecule to TNT [91]. To investigate TNT sensing performance of the pMSNs, we recorded fluorescence spectra of pMSNs dispersion before and after the addition of TNT with concentrations ranging from 10 nM to 10 μM. Both monomer and excimer emission intensities of pyrene were quenched gradually with increasing TNT concentration (Figure 4.9a). After the addition of 10 μM of TNT, excimer emission was completely quenched, on the other hand, significant monomer emission still can be observed. Figure 4.9b shows the rapid

quenching of the excimer emission upon addition of 500 nM of TNT. Excimer emission quenching reaches its maximum within only 45 seconds and remains constant up to five minutes. It is important to note that in the absence of TNT, excimer emission is constant within the same time interval (Figure 4.9b).
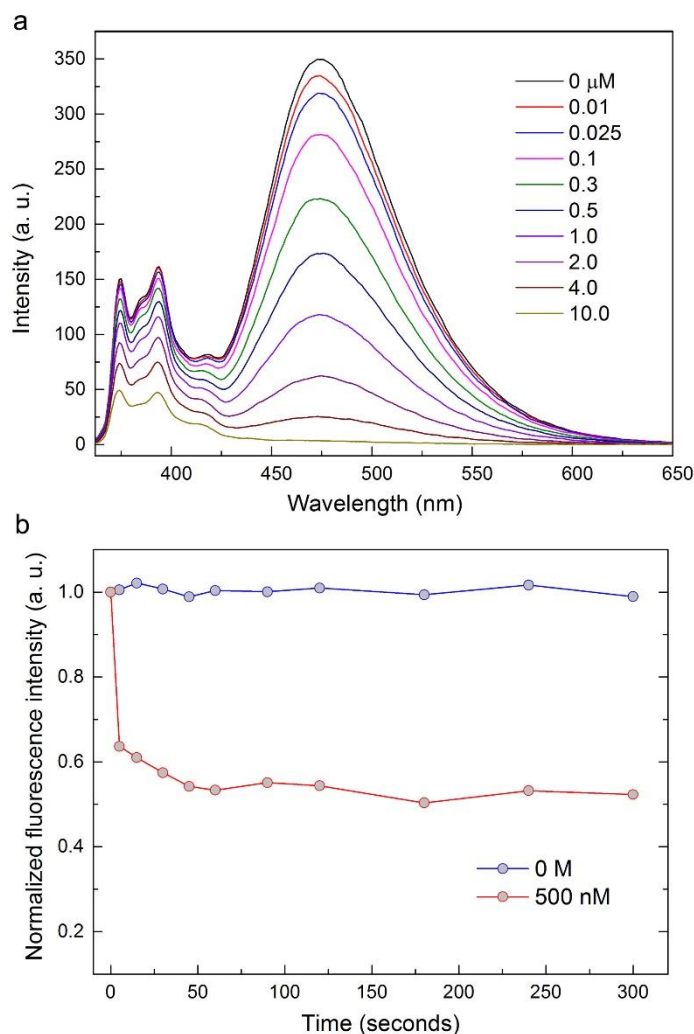
Figure 4.9: (a) Fluorescence emission spectra of the pMSNs with increasing TNT concentrations. Excitation wavelength was set at 340 nm for the measurements. (b) Time-dependent excimer emission intensity of the pMSNs in the absence and in the presence of 500 nM of TNT.

Figure 4.10 shows quenching efficiencies of the excimer and monomer emission of pMSNs depending on the TNT concentration. Quenching efficiency of the excimer emission at 475 nm was 3.1% for 10 nM of TNT and reached to 67.2% and 98.9%,

when 1.0 µM and 10 µM of TNT were added, respectively. On the other hand, for all concentrations, quenching efficiency of the monomer emission at 394 nm was lower than that of the excimer emission which indicates the higher sensitivity of the excimer emission against TNT (Figure 4.10a). Figure 4.10b shows the exponential fit to quenching data in the range from 10 nM to 1.0 µM (regression constant is 0.99). Using this calibration curve, we calculated the detection limit of the fluorescent sensor to be 12 nM against TNT.
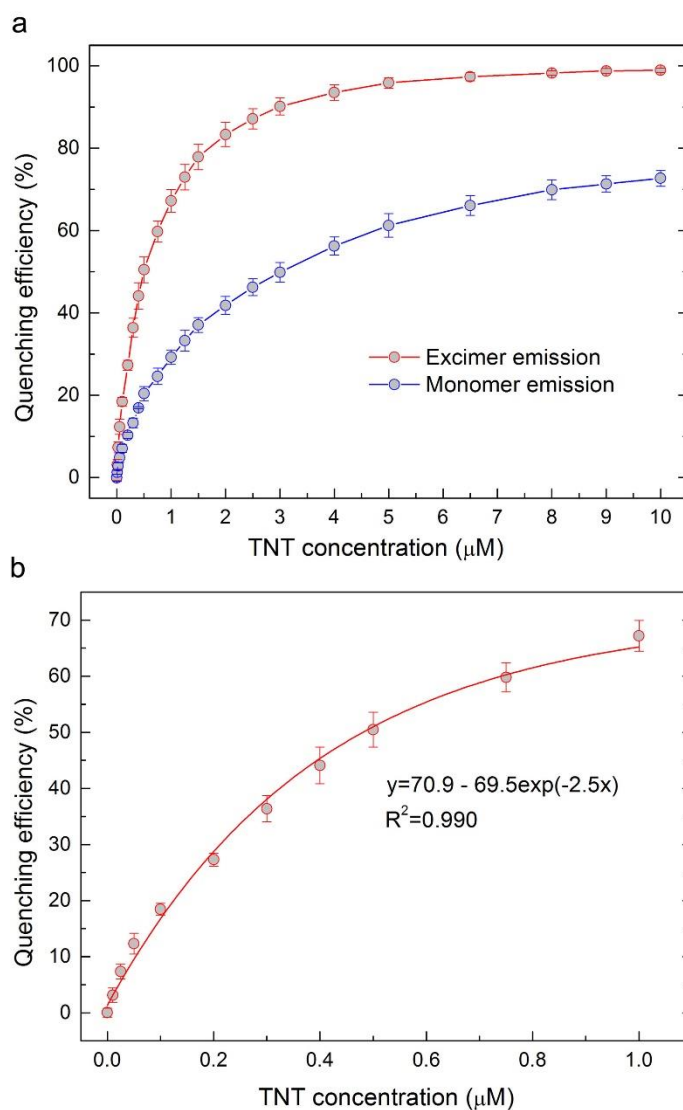
Figure 4.10: (a) Quenching efficiencies of the pMSNs depending on the TNT concentration based on the excimer emission (at 475 nm) and monomer emission (at 394 nm). (b) Calibration curve for TNT concentration in the range from 10 nM to 1.0 µM.

In addition to the higher quenching efficiency of excimer emission, its bright blue colour enables the naked-eye detection of TNT. Accordingly, quenching of the excimer emission of pMSNs was visually observed under the UV-light illumination. Figure 4.11 shows the photographs of pMSNs taken before and after the addition of 0.4 µM, 1.0 µM, 4.0 µM, and 8.0 µM of TNT. Excimer emission intensity significantly reduced when 0.4 µM of TNT was added. Emission was further quenched with the increasing TNT concentration and almost no excimer emission remained with the addition of 8.0 µM of TNT.
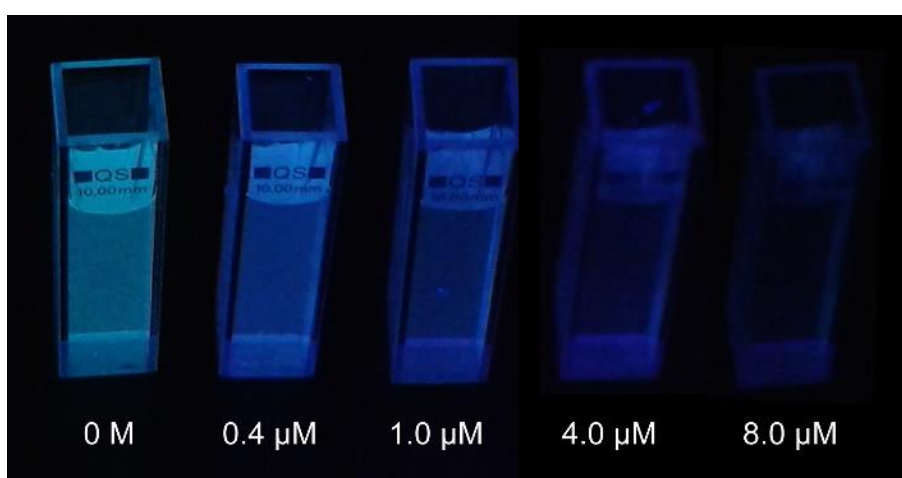
Figure 4.11: Optical photographs of pMSNs dispersions under UV-light before and after the addition of 0.4 µM, 1.0 µM, 4.0 µM, and 8.0 µM of TNT. Quenching of the excimer emission is clearly visible for the increasing TNT concentration.

To demonstrate the selectivity of pMSNs against TNT, we measured the fluorescence of pMSNs after addition of 10.0 µM aqueous solutions of various aromatic and non-aromatic substances. Figure 4.12 shows the quenching efficiencies of excimer emission observed for the tested analytes. Quenching efficiency for TNT was 98.9% whereas quenching efficiencies for other nitroaromatic compounds were 40% and 25% for dinitrotoluene (DNT) nitrobenzene (NB), respectively. On the other hand, chloroform, sodium hydroxide, benzoic acid, aniline, sodium chloride, methanol, and hydrochloric acid did not quenched excimer emission significantly indicating the sensitivity of the excimer emission for nitroaromatic explosives. Lower quenching efficiencies for DNT and NB compared to that for TNT were due to their

fewer nitro (NO$_2$) groups; DNT has two NO$_2$ groups and NB has one NO$_2$ group. Since the driving force for the electron transfer is low reduction potential, TNT with its three NO$_2$ groups has the lowest reduction potential and higher electron accepting ability [104]. Therefore, excimer emission was quenched more in the presence of TNT compared to DNT and NB at the same conditions.
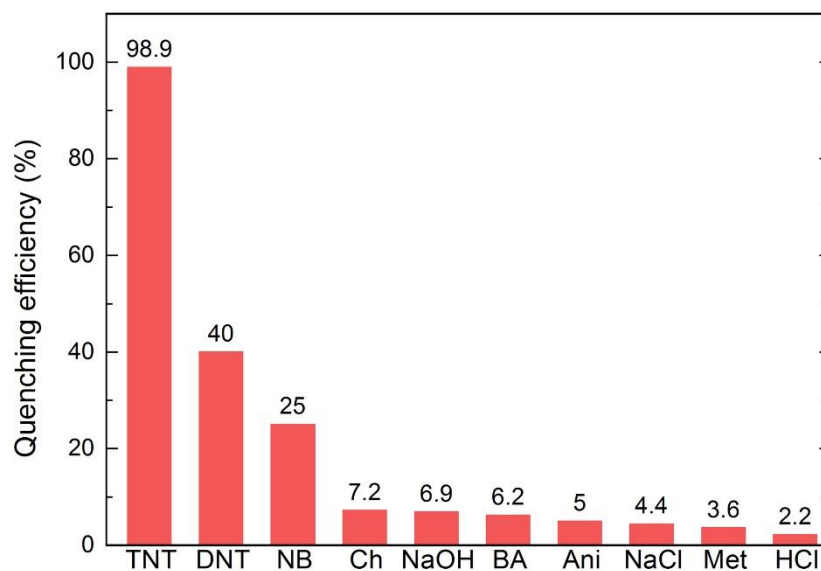
Figure 4.12: Fluorescence quenching efficiencies of excimer emission for 10.0 μM aqueous solutions of various analytes (TNT: trinitrotoluene, DNT: dinitrotoluene, NB: nitrobenzene, Ch: chloroform, NaOH: sodium hydroxide, BA: benzoic acid, Ani: aniline, NaCl: sodium chloride, Met: methanol, and HCl: hydrochloric acid).

Chapter 5

A Porosity Difference Based Selective Dissolution Strategy to Prepare Hollow MSNs

5.1 Introduction

Hollow silica nanostructures are attracting a great deal of interest in many research areas including controlled drug delivery, catalysis, bioimaging, optical coatings and absorbents due to their unique properties such as high surface area and pore volume, ease surface functionalization, chemical stability and low toxicity [105-107]. They are often prepared using template based methods in which a variety of hard [108-115] (polymer or inorganic micro/nano-particles) or soft [116-123] templates (droplets, bubbles, micelles *etc.*) can be applied. However, template based methods have some drawbacks which prevent their widespread applications. For instance, hard templating methods have tedious multistep and time-consuming procedures including core synthesis, surface functionalization of core, silica deposition and core etching. Soft template methods, on the other hand, involves less synthesis steps; however products of these methods are often have ill-defined shapes and polydisperse in size due to deformability of soft-templates [105]. Recently, templateless (or self-templating) methods such as surface protected etching [124-126] and selective etching [127-130] have emerged to fulfil the need for simple, effective and scalable synthesis of hollow silica nanostructures. However, these templateless methods usually require corrosive and toxic etching agents (strong alkaline or HF solutions) to selectively etch cores of

solid silica particles. A few recent works reported that under the mild conditions (water or slightly acidic solutions) silica nano/microparticles can go spontaneous structural change from solid spheres into hollow particles [131-136]. Unfortunately, in these methods a special care must be taken to control the shell thickness and particles morphology since they are very dependent to the reaction conditions such as pH, temperature, and etch time. Also, the shells of resulting hollow particles usually do not have accessible mesopores which restricts their applications in many fields such as controlled drug release, catalysis and pollutant adsorption. In addition, the shape of the hollow particles prepared through spontaneous structural change process are limited with spheres since their synthesis often started with spherical Stöber silica nanoparticles. Other than spheres, rods or tubes can be more desired for some applications. For example, rod shaped particles are proved to be more effective in biological applications than their spherical counterparts due to their higher cellular uptake [137]. Overall, facile and scalable preparation of hollow silica nanostructures with tailored shape and porosity is still a great challenge.

Here, we report a distinct templateless method (*i. e.* porosity difference based selective dissolution strategy) to prepare hollow silica nanospheres and nanorods with mesopores on their shells using a mild etching agent; phosphate buffered saline (PBS) (Figure 5.1). The method is based on the selective dissolution of mesoporous silica cores of solid silica shell/mesoporous silica core nanoparticles, which gives a good control over particle size, shell thickness, porosity and particle shape (sphere or rod). The method involves two steps; (i) synthesis of core/shell nanospheres or nanorods in a one pot reaction and (ii) selective etching of mesoporous cores in PBS. The particle morphology can be controlled using rose Bengal (RB) dye. Rod-shaped mesoporous silica nanoparticles (MSNs) with controllable aspect ratio can be prepared in the presence of RB; in the absence of RB particles are spherical. Solid silica shells can be coated over these particles by simply addition of excess silica precursor during the synthesis. To our surprise, during the hollowing process, mesopores developed on the solid silica shells which provides accessibility to the hollow interior of the particles. In addition, we proposed a dissolution mechanism to the observed porosity difference based dissolution of core/shell nanoparticles. Furthermore, we prepared self-luminescent hollow MSNs using organosilane-modified core/shell particles.
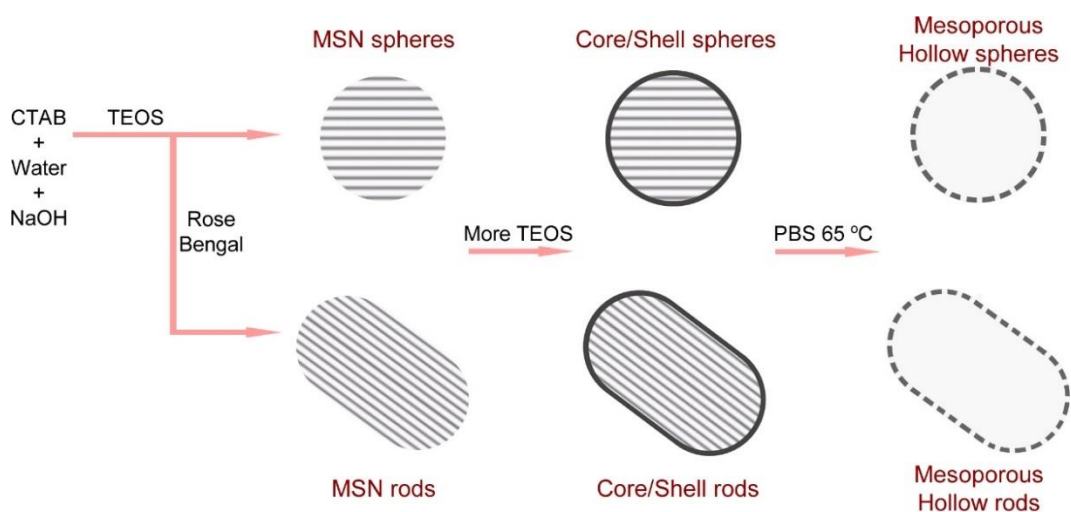
Figure 5.1: Schematic representation of synthesis of hollow nanospheres and nanorods. In the presence of RB dye rod-shaped particles are formed. Addition of excess TEOS during the reaction produces uniform silica shell around particles. During the incubation in PBS, core shell.

5.2 Experimental Section

Materials: Cetyltriammoniumbromide (CTAB), F127 pluronic polymer, and Rose Bengal were purchased from Sigma-Aldrich (USA). Tetraethyl orthosilicate (TEOS) and aminopropyl triethoxysilane (APTES) were purchased from Merck (Germany). All chemicals were used as purchased.

Preparation of mesoporous silica nanospheres and nanorods: Nanospheres were prepared by modifying previous reports [46, 47, 101]. Briefly, 200 mg CTAB was dissolved in 95 mL of water and 1 mL of F127 solution (5 mg/mL in water) and 0.7 mL of 2 M NaOH were added onto this solution. Then the reaction mixture was heated to 80 °C while stirring vigorously (600 rpm). After temperature was fixed at 80 °C, 1.2 mL of TEOS was rapidly added and reaction mixture was further stirred for 2 h. Finally, reaction solution was cooled down to the room temperature and particles were collected by centrifugation at 9000 rpm for 20 min and washed with water twice. To synthesize nanorods, we added appropriate amount of RB (for example 10 mg for the particles with the aspect ratio of 1.9) dissolved in 2 mL of water to the reaction mixture after addition of TEOS; other parameters were same with the nanosphere synthesis.

60

To remove the surfactant and RB molecules, we calcined the particles at 550 °C for 5 hours (ramp rate was 5 °C/min).

Preparation of core/shell nanoparticles: To prepare core/shell particles we added appropriate amount of TEOS after 1 h of first TEOS addition. Other parameters were kept constant.

Preparation of hollow nanoparticles: Cores of the core/shell particles were dissolved by incubating the particles in PBS (10 mM, pH 7.4) at 65 °C for 1 d under gentle stirring. Particle concentration in PBS solution was 0.5 mg/mL for nanospheres and 1 mg/mL for nanorods. Particles were collected by centrifugation at 9000 rpm for 20 min and washed with water twice. Finally, particles were calcined at 550 °C for 5 hours (ramp rate was 5 °C/min) to remove the CTAB surfactant and RB molecules.

Preparation of self-luminescent hollow nanoparticles: In this case, 100 μL of APTES was added during the shell growth step. Other parameters were kept same with the core/shell nanosphere preparation. To obtain self-luminescence property and remove the surfactant molecules, particles were calcined at 400 °C for 3 hours (ramp rate was 5 °C/min). Finally, cores of the core/shell particles were dissolved by incubating the particles in PBS (10 mM, pH 7.4) at 65 °C for 1 d under gentle stirring. Particle concentration was 0.5 mg/mL.

Characterization: Transmission electron microscopy (TEM) images were obtained using a Tecnai G2 F30 (FEI) microscope. The scanning electron microscopy (SEM) images of particles were obtained using an E-SEM; Quanta 200F (FEI). Surface area, pore volume and pore size distribution of the particles were determined using an iQ-C (Quantachrome). X-ray powder diffraction (XRD) spectra of the particles were taken using an X'Pert Pro (Panalytical). Fluorescence spectrum of the particles was recorded by a Fluorescence Spectrophotometer (Eclipse, Varian).

5.3 Synthesis and Characterization of MSNs

Figure 5.2 shows the effect of RB on the morphology of MSNs. In the absence of RB, particles are almost spherical (Figure 5.2a,d) which is typical for MCM-41 type MSNs [101]. Average particle size of spherical MSNs was calculated to be around 120 nm from TEM images. Interestingly, in the presence of 5 mg of RB (Figure 5.2b,e)

rod-shaped MSNs (aspect ratio is ~1.5) was obtained. Doubling of the RB amount (10 mg) increases the aspect ratio of particles to ~1.9 (Figure 5.2c,f). Average particle width and length for rod-like MSNs prepared using 10 mg of RB were determined to be around 75 nm and 145 nm, respectively from TEM images.
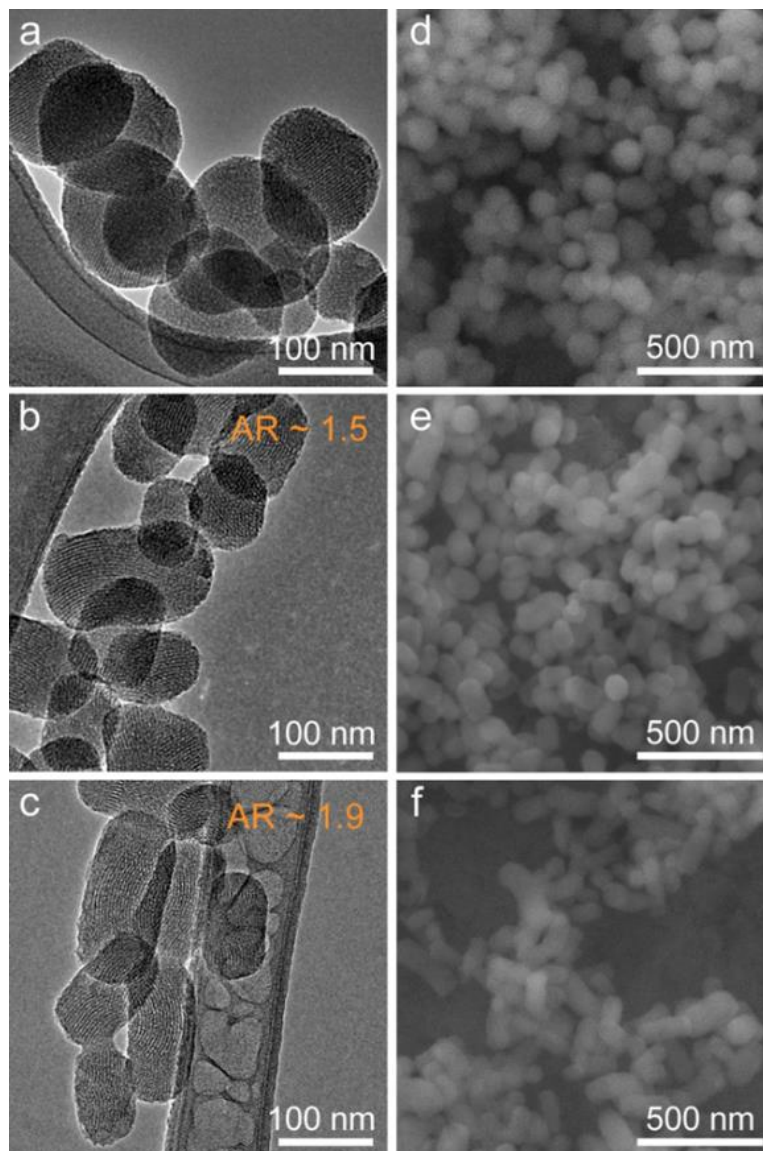
Figure 5.2: TEM (left panel) and SEM (right panel) of MSNs prepared using different amounts of RB. (a, d) No RB, (b, e) 5 mg RB and (c, f) 10 mg RB. In the presence of RB, rod-shaped MSNs are formed and with the increasing RB amount longer rods can be obtained.

Further increasing the RB amount (20 mg), however, result in a mixture of polydisperse spheres and very long helical rods with aspects ratios even larger than 10 (Figure 5.3).
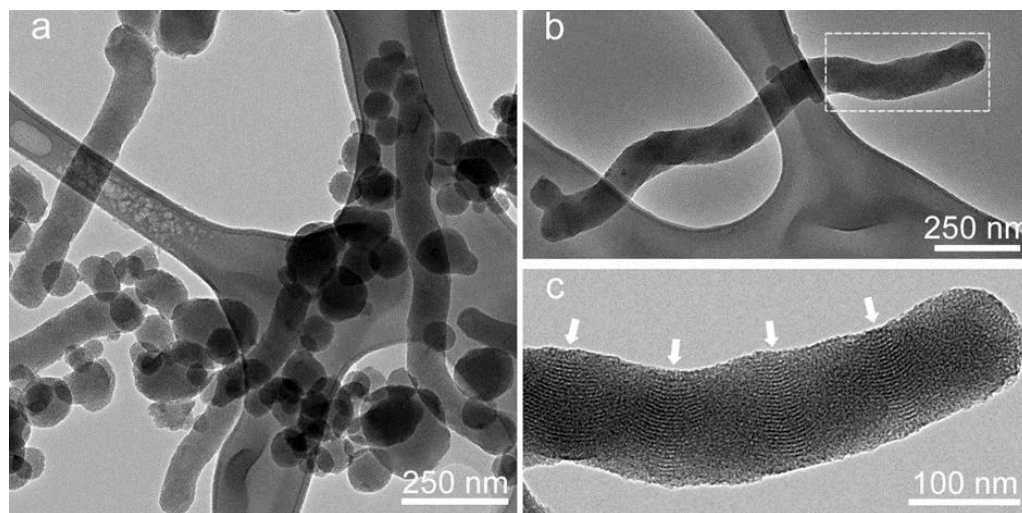
Figure 5.3: TEM images of MSNs prepared using 20 mg of RB. (a) Low magnification image showing the polydispersity of the particles. (b) TEM image of a helical nanorod with large aspect ratio. (c) Close-up image of the helical nanorod shown in (b). White arrows indicate the helical porous structure of the nanorod.

Preparation of rod-shaped MSNs using additional organosilane monomers [138-140] or surfactants [141-143] have been previously reported. The change in the particle morphology is believed to be due to the interactions between surfactant micelles and additional monomers or surfactants which changes the morphology of surfactant micelle assembly and accordingly the final shape of MSNs. To our knowledge, this work is the first example of using a simple molecule like a commercial dye (RB) as a co-structure directing agent to prepare rod-shaped MSNs. It is important to note that, besides from co-structure directing agent based methods, other methods are also available to prepare rod-shaped MSNs utilizing different surfactants [144] or simply different experimental conditions [145, 146]. Nevertheless, this study reports an alternative and simple method prepare rod-shaped MSNs. Also, we believe that interactions of large molecules such as dyes and drugs with the surfactant micelles deserves a particular interest because using this simple strategy preparation of MSNs

with many distinct morphologies may be possible. In fact, recently Du *et al.*, [147] reported the formation of large-pore MSNs in the presence of ibuprofen drug.

5.4 Synthesis and Characterization of Core/Shell MSNs

Mesoporous core/solid silica shell particles are prepared in a one-pot reaction. Following the polymerization tetraethyl orthosilicate (TEOS) monomer around CTAB micelles to form initial MSNs, excess TEOS monomer was added to prepare solid shells around the particles. Figure 5.4 shows the TEM images of core/shell nanospheres and nanorods which were prepared using different amounts of TEOS in the second addition. Uniform solid silica shells around the particles reflect clear contrast difference from the porous cores. Figure 5.4a,b show the nanospheres prepared using 1 and 3 mL of additional TEOS which have 8 and 12 nm thick very uniform shells, respectively. Similarly, 8 nm thick uniform silica shell was observed around the nanorods (Figure 5.4c) when 1 mL TEOS was used in the second step showing that the shell thickness is independent from the particle morphology. Figure 5.4d demonstrates the effect of second TEOS addition amount on the silica shell thickness of nanospheres. We observed that between 0.5 and 2 mL of TEOS addition, shell thickness gradually increased to 12 nm from 5 nm. Further increase in the TEOS amount (3 mL) did not change shell thickness significantly indicating that shell thickness growth is self-limiting.
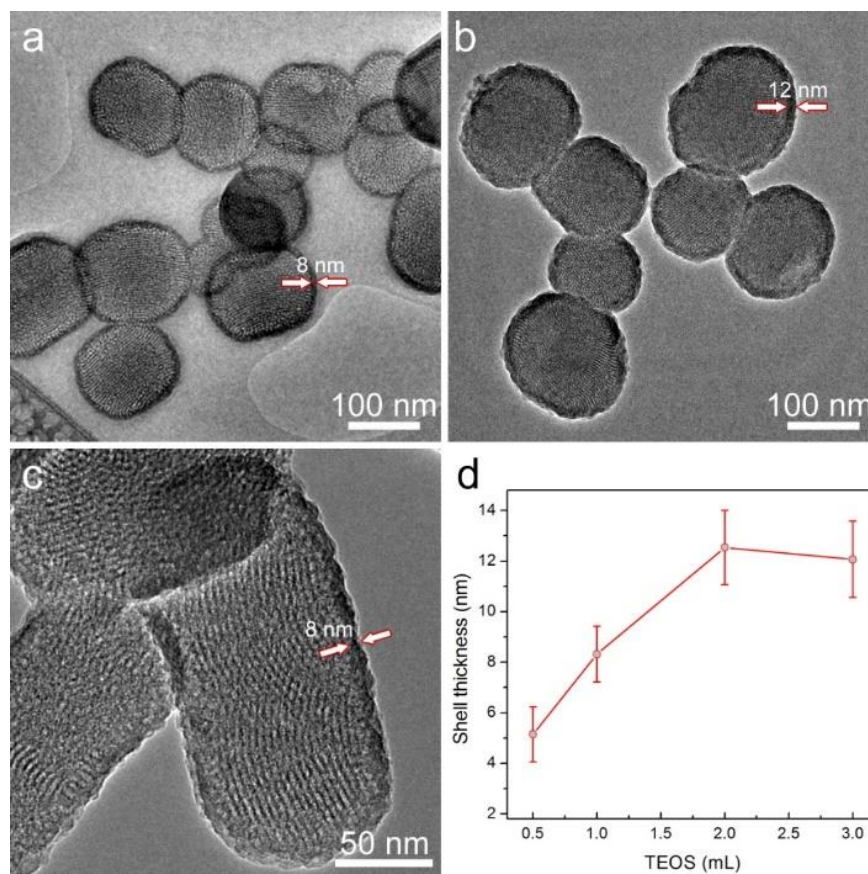
Figure 5.4: Morphology and shell thickness of core/shell MSNs. (a-c) TEM images of spherical MSNs prepared using 1 mL of additional TEOS (a), spherical MSNs prepared using 3 mL of additional TEOS (b), rod-shaped MSNs prepared using 1 mL of additional TEOS (c). Arrows indicates the shells of the particles. (d) Shell thickness of spherical particles depending on the additional TEOS amount.

5.5 Selective Dissolution of Porous Cores in PBS

Porous cores of the core/shell particles were selectively dissolved by incubating the particles in PBS at 65 °C for one day (Figure 5.5). After hollowing process, the particles were calcined at 550 °C to remove the CTAB surfactant and RB molecules. The selective dissolution behavior of the core can be attributed to the higher surface area of the porous core; hydroxyl ions can attack (Figure 5.6) to the porous network from many sites and dissolve it faster compared to the dense silica shell. In addition, it is well known that inner parts of the silica nanoparticles are less condensed compared to the nanoparticle surface [134] which makes the inner parts more susceptible for

dissolution. It is believed that both cases contributed the selective dissolution of porous cores.
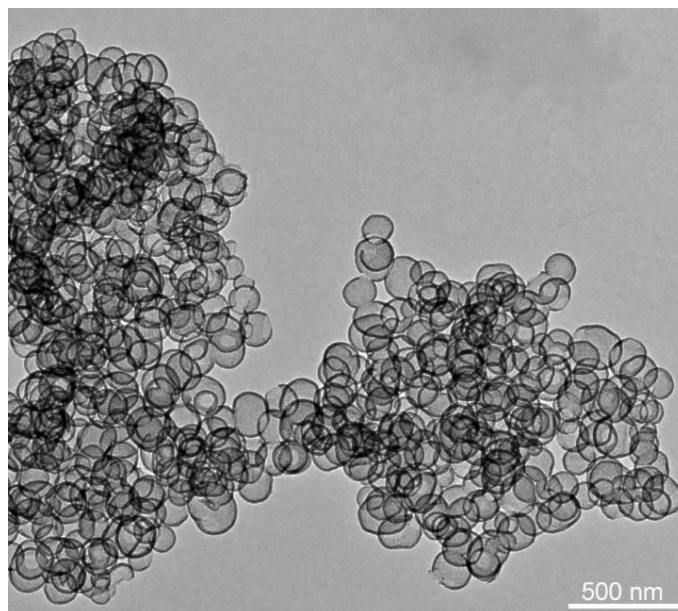
Figure 5.5: Low magnification TEM image of hollow nanospheres showing high yield of hollowing process.

Particle concentration in PBS solution was 0.5 mg/mL for nanospheres and 1 mg/mL for nanorods. We observed that partially etched particles are formed at the higher particle concentrations suggesting that an equilibrium is reached for silica dissolution. Also, the maximum concentration for complete core hollowing of nanorods are higher than that of spheres. This may be due to the difference in the condensation rate of core silica network between nanospheres and nanorods. Note that nanorods are synthesized in the presence of RB which can be encapsulated to the silica network during polymerization and decrease condensation rate.
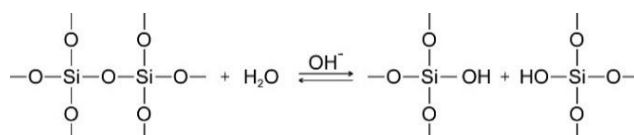
Figure 5.6: Mechanism of hydroxide ion catalyst silica dissolution and regrowth.

Figure 5.7 shows the TEM images of fabricated hollow nanospheres (prepared using 1 mL of additional TEOS) and nanorods (prepared using 10 mg of RB and 1 mL of additional TEOS). There is clear contrast difference between interior and exterior parts of the particles indicating core dissolution after PBS incubation. The efficiency of hollowing process is almost 100% (Figure 5.5). Importantly, the shell thickness remained almost intact after the hollowing process; around 8-9 nm, for both nanospheres and nanorods which suggests that only cores of the particles dissolved.
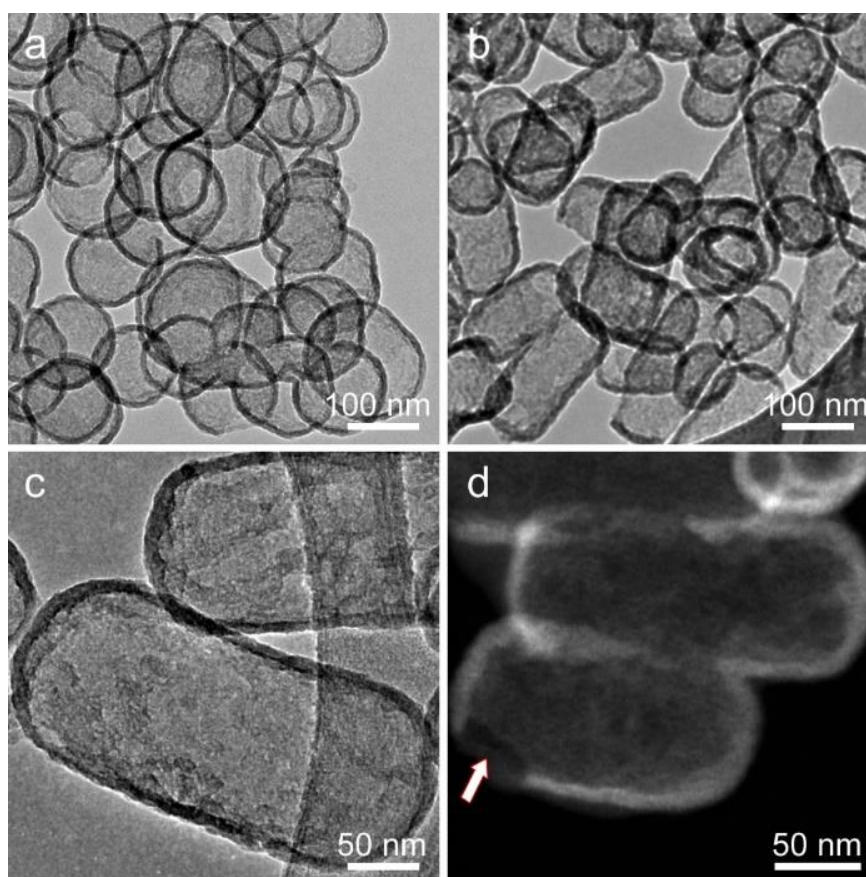
Figure 5.7: TEM images of hollow particles. (a) Hollow nanospheres prepared using core/shell particles with 8 nm shell thickness, (b) hollow nanorods prepared using core/shell particles with 8 nm shell thickness. Shell thickness of hollow particles remained same after hollowing process, indicating that cores were completely dissolved. (c) Close-up TEM image of nanorods. (d) High magnification STEM image of hollow nanorods that shows the mesoporous shells of particles. Arrow indicates a crack formed on the hollow nanorod shell during core dissolution and calcination processes.

To our surprise, shells of the particles contains mesopores after dissolution which can be clearly seen from Figure 5.7c and d. Mesoporosity of the shells was further confirmed using N_2 adsorption-desorption technique (see below). The mesopores can be formed during silica dissolution process in the presence of surfactant molecules [128]. It is well known that dissolution of silica is reversible (Figure 5.6) and therefore dissolved silica species can spontaneously regrown [131]. For our case, in the presence of residual CTAB (leaking from dissolved cores of the particles) dissolved silica can regrown around CTAB micelles to produce mesoporous shell. Another reason of the mesopores can be the residual CTAB molecules which are absorbed to the shell silica network during the synthesis of particles. These residual CTAB molecules can contribute the pore formation during dissolution, regrowth and calcination processes [128]. Besides, we observed cracks on the some of the particles after calcination process (Figure 5.7d). Nevertheless, according to the TEM images most of the particles were crack-free.

Pore structure, volume, and size and specific surface area of rod-shaped particles were characterized using N_2 adsorption-desorption and XRD techniques. Figure 5.8a shows the N_2 adsorption-desorption curves of nanorods (rMSN), core/shell nanorods (rMSN-ts), and hollow nanorods (h-rMSN). rMSN and rMSN-ts revealed type-IV nitrogen sorption curve with a sharp capillary condensation step in nitrogen adsorption amount at relative pressures P/P_0 between 0.2 and 0.4 indicating the presence of mesopores with narrow size distribution [115, 133]. On the other hand, this step disappeared for h-rMSN reflecting the dissolution of ordered mesoporous core. Corresponding pore size distributions of the particles, which were obtained from N_2 adsorption-desorption curves using DFT method, are given in Figure 5.8b. rMSN and rMSN-ts revealed similar narrow pore size distribution with micropores (1.4 and 1.5 nm, respectively) and mesopores (2.9 nm and 3 nm, respectively). The presence of micropores in the shell provides accessibility of PBS to the mesoporous core and also allows removal of dissolution products to outside of the particle [132]. The pore size distribution of h-rMSN, on the other hand, was wide between 1.5 and 7 nm which may be due to the random nature of the silica dissolution and regrowth process and pore widening during core dissolution and calcination processes. Also, second wide peak was observed in the h-rMSN pore size distribution between 13 and 22 nm which may

be correspond to the cracks formed on the shell during dissolution and calcination processes.
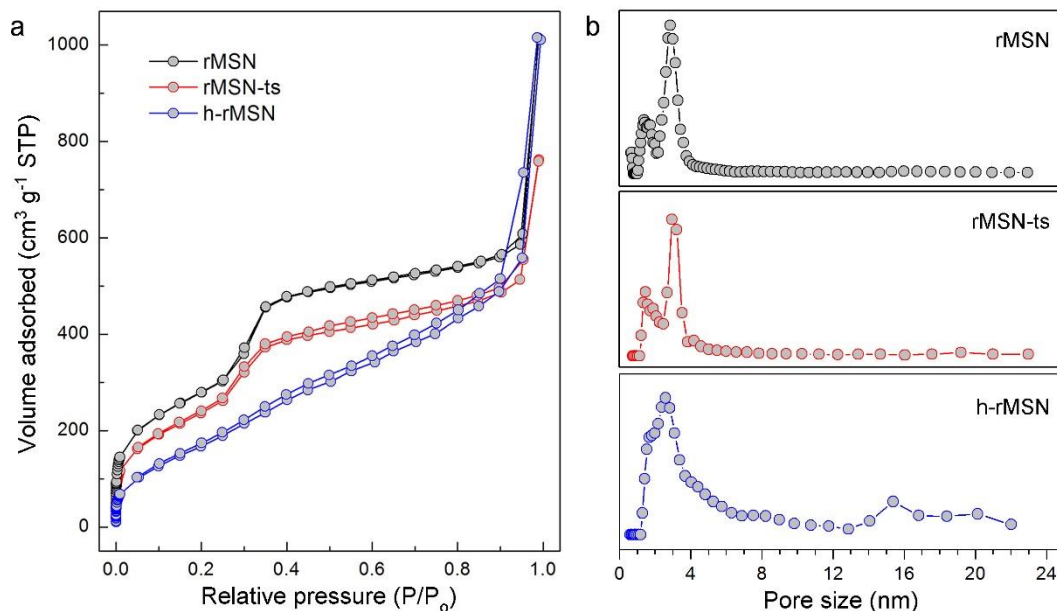
Figure 5.8: (a) N_2 adsorption and desorption curves of rod-shaped particles. (b) Pore size distribution of particles calculated using the N_2 adsorption and desorption curves. rMSN and rMSN-ts showed narrow pore size distribution, on the other hand, h-rMSN have broad pore size distribution. (rMSN; rod-shaped MSNs, rMSN-ts; rod-shaped core/shell MSNs, and h-rMSN; rod-shaped hollow MSNs)

Surface area and pore volume of the particles were calculated using BET and DFT methods, respectively. Surface area of rMSN is 1008 m^2/g and it is reduced to 862 m^2/g after coating the particles with solid silica shell (rMSN-ts). Surface area further reduced to 598 m^2/g after core dissolution (h-rMSN) due to loss of highly ordered and mesoporous cores. Pore volume of rMSN is 1 cm^3/g and it is again slightly reduced (0.87 cm^3/g) after silica coating. As expected, pore volume increases more than two fold (1.94 cm^3/g) after etching the core of the particles.

Figure 5.9 shows the XRD spectra of the rod-shaped particles. rMSN and rMSN-ts, exhibited characteristic diffraction peaks, (100), (110), and (200), of the highly ordered hexagonal pore structure of MCM-41 type mesoporous materials; whereas no order was observed for h-rMSN. Based on TEM, N_2 adsorption-desorption and XRD

observations, it can be concluded that shells of hollow particles contains non-ordered mesopores with large pore size distribution.
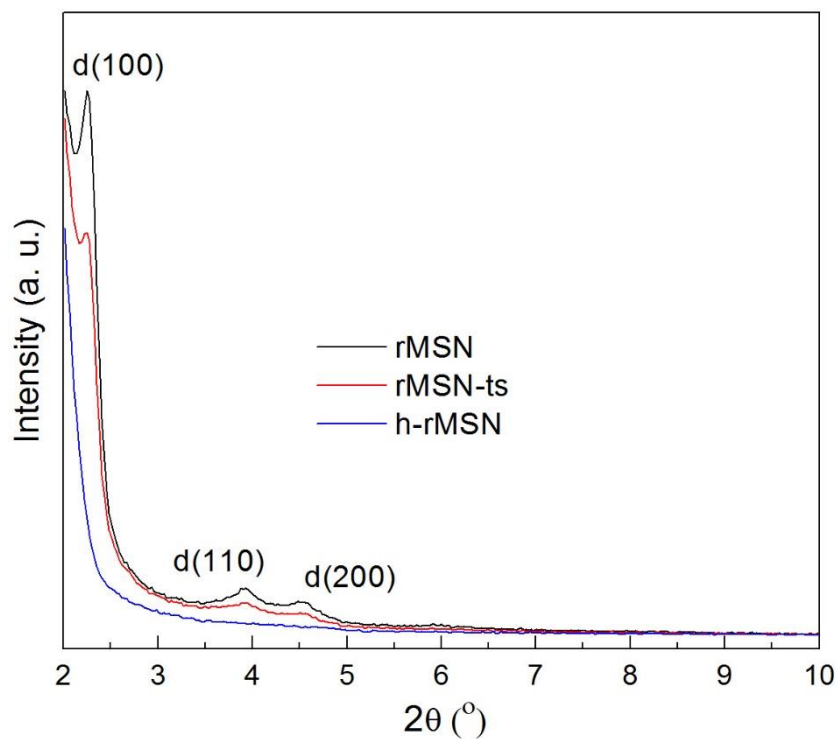
Figure 5.9: XRD spectra of rod-shaped particles. rMSN and rMSN-ts, demonstrated characteristic diffraction peaks, (100), (110), and (200), of the highly ordered hexagonal pore structure of MCM-41 type mesoporous materials. On the other hand, pore order disappeared after core dissolution (h-rMSN).

Using the porosity difference based selective dissolution method, it is possible to prepare particles with different morphologies. For instance, Figure 5.10 shows the TEM images of the partially hollowed nanospheres. These particles contain a few large pores in their cores. Also, it is still possible to observe ordered mesopores in the non-dissolved parts (Figure 5.10b). To prepare the half-etched particles we increased the particle concentration to 5 mg/mL and we kept the dissolution time and temperature constant. Note that reaction is spontaneously quenched at this particle concentration; further increasing the reaction time does not change the particle morphology. Therefore, it is possible to partially dissolve the cores of core/shell particles simply changing the particle concentration in the PBS solution.
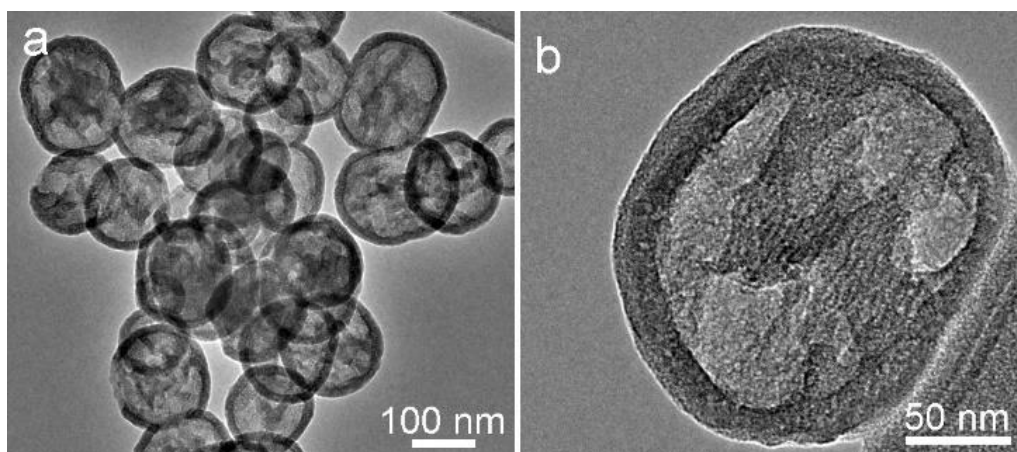
Figure 5.10: TEM images of partially hollowed spherical particles (a) low magnification and (b) high magnification. Partially hollowed particles contain a few large pores in their cores and it is still possible to observe ordered mesopores in the non-dissolved parts.

5.6 Possible Mechanism of Selective Dissolution Process

In order to investigate the selective dissolution mechanism, we collected samples at different time intervals during the incubation of rMSN-ts in PBS at 65 °C (particle concentration is 1 mg/mL). However, we noticed that at this temperature core dissolution is very fast; cores of the particles were completely etched after 30 minutes, which prevent us from the observation of dissolution steps. To slow down the reaction we decreased the dissolution temperature to the room temperature and increased the particle concentration to 5 mg/mL. As expected, the core dissolution is very slow at these conditions. At the beginning of the dissolution process (after 1 day), many small pores around 10 nm was observed (Figure 5.11a). After 3 days (Figure 5.11b) pore sizes increased and it further increased after 1 week (Figure 5.11c). This indicates that core etch starts from multiple points, and these sites became wider with time and then interconnected with each other. At the end of the process all of the pores were interconnected to form the hollow core (Figure 5.11d).
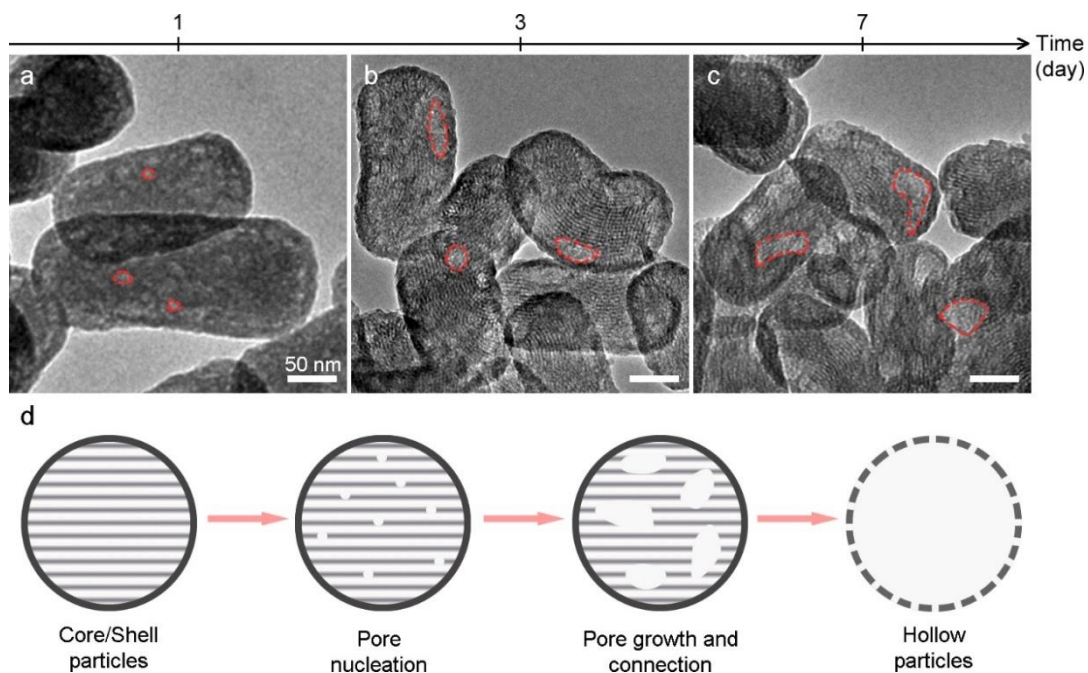
Figure 5.11: Mechanism of core dissolution process. (a-c) TEM images taken at different time intervals during the hollowing of rod-shaped MSNs at room temperature. (a) 1 day, (b) 3 days and (c) 7 days. After 1 day, many small pores around 10 nm was observed. The size of these pores increased with time. Some dissolved areas outlined in red in all TEM images. (d) Schematic representation of core dissolution process.

To explore the role of PBS in the dissolution process, we replaced the PBS with water and incubated rMSN-ts at 65 °C for one day. We observed that in water some of the cores were not fully dissolved (Figure 5.12) indicating that dissolution in water is slower than in highly salted PBS environment. In fact, it is well known that silica dissolution is faster in salted solutions, [136] which is in accordance with our observations. Nevertheless, cores of particles can be dissolved in water by decreasing the particle concentration or prolonging the incubation time.
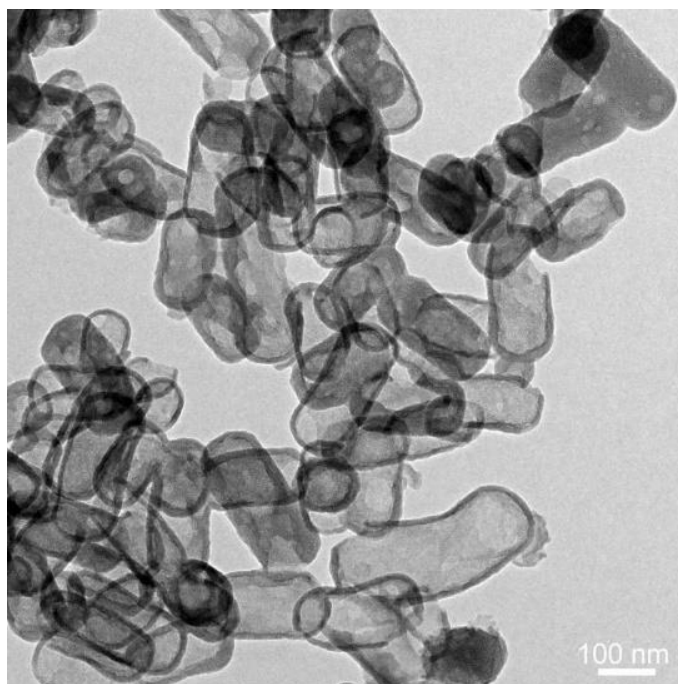
Figure 5.12: TEM images of the nanorods incubated in water at 65 °C for one day. Cores of the several particles remained completely or partially undissolved at these conditions.

We also investigated effect of calcination on the selective dissolution process. In this case, first we calcined the particles at 550 °C for 5 h in order to strengthen the silica network, then we incubated the particles in PBS at 65 °C for one day. One can expect no or partially dissolved cores for this case due to the improved condensation degree of silica after high temperature treatment [48]. On the contrary, we observed that cores of the particles dissolved similar to the non-calcined particles (Figure 5.13). However, shell thickness of the precalcined particles are almost two times thicker (14 nm) than postcalcined particles.
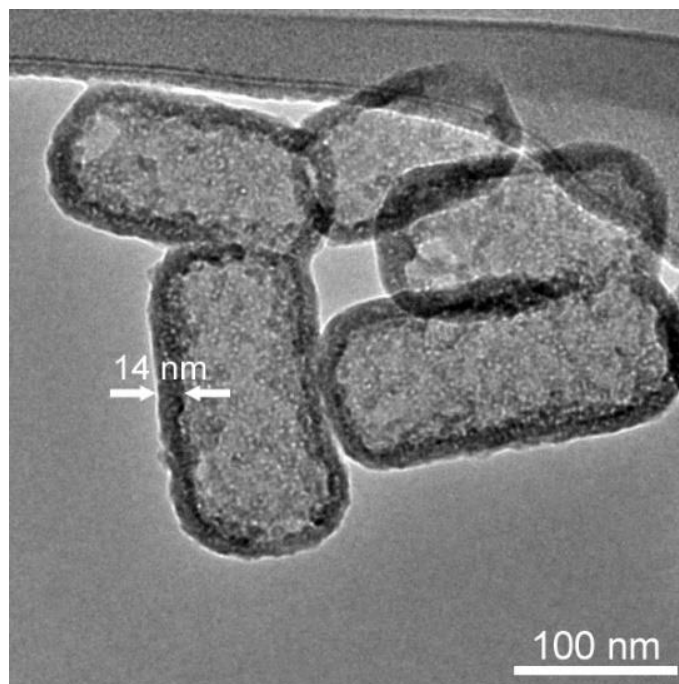
Figure 5.13: TEM images of the precalcined nanorods after core dissolution process.

5.7 Self-Luminescent Hollow MSNs

A facile fluorophore-free way to prepare luminescent silica nanoparticles is the calcination of organosilane ligand containing (*e. g.* aminopropyl) silica nanoparticles at high temperatures [148-150]. It is believed that the origin of the luminescence is the oxygen defects formed in the silica network during calcination of organosilane moieties [148]. Accordingly, we prepared self-luminescent hollow MSNs by adding aminopropyl triexhoxysilane (APTES) during the shell growth and calcined the particles at 400 °C for 3h. Note that, calcination process also removes the surfactant molecules. After calcination, we hollowed the particles in PBS at 65 °C. Inset of Figure 5.14 shows the TEM image of the resulting particles. We observed that APTES addition did not significantly affect the particle morphology. Shell thickness of the particles were around 11 nm which is in accordance with our previous observations. Figure 5.14 shows the fluorescence spectrum of the self-luminescent hollow MSNs when excited at 360 nm. The broad luminescence spectrum of particles centered around 460 nm.
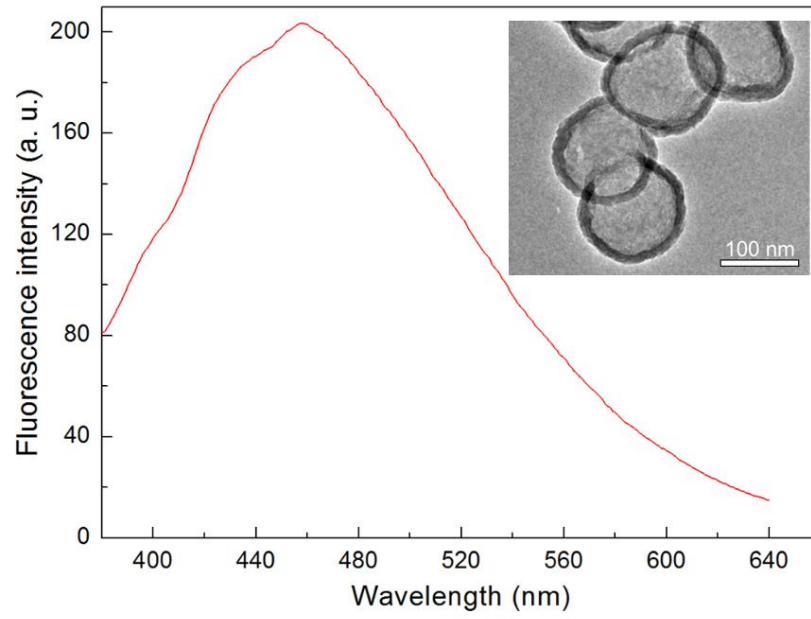
Figure 5.14: Fluorescence spectrum of self-luminescent hollow MSNs in water (excitation wavelength was 360 nm). Inset shows the TEM image of the particles.

Chapter 6

Impact of MSN Surface Functionality on Hemolytic Activity, Thrombogenicity and Non-Specific Protein Adsorption

6.1 Introduction

The extensive research on mesoporous silica nanoparticles in last decade have shown the promising potential of these materials in biomedical applications as drug and gene carriers [49, 151-154] cell markers [54, 155-157] and diagnosis and therapy agents [13, 34, 158, 159]. However, most of the research focused on synthesis and applications of these materials and only a few reports investigated *in vitro* and *in vivo* toxicity of the MSNs. *In vitro* studies [16, 160, 161] showed good biocompatibility of mesoporous silica nanoparticles with various cell lines; nevertheless, low *in vitro* cytotoxicity does not assure that MSNs are biocompatible *in vivo*. In fact, recent reports indicate possible *in vivo* cytotoxicity of silica based materials. Several groups reported that silica and mesoporous silica nanoparticles can cause lysis of red blood cells (RBCs) [17, 162-166]. In addition, it was reported that intravenous injection of mesoporous silica particles to mice can be fatal due to the obstruction in the vasculature, which may led to multiple subsequent vital organ failure [18, 22]. In another study, silica nanoparticles were observed to cause pregnancy complications in

mice [14]. These results revealed that in order to use MSNs in biological applications, their biocompatibility must be well characterized and improved to an appropriate level.

Interaction of nanoparticles with blood constituents deserves particular consideration, since initial encounters among MSNs and the organism occurs within the circulatory system. Therefore, determining the blood compatibility of MSNs is the primary screening for their *in vivo* toxicity regarding applications that particles are delivered by intravenous injection. Nanoparticles injected into the blood may cause several adverse effects such as hemolysis and blood clot formation (thrombogenicity). Hemolysis is the disintegration of RBCs due to deformation of their cell membrane. MSNs can interact with positively charged RBC membrane electrostatically through their negatively charged surface silanol groups; therefore they can cause hemolysis [163]. Lin *et al.* [17] studied the hemolytic activity of several MSNs with diameters between 25 and 225 nm and concluded that increasing the particle size of MSNs diminished the hemolytic activity to a degree. Also, Yu *et al.* [165] demonstrated that rod shaped MSNs resulted in lower hemolytic activity than spherical ones. Nevertheless, for all cases bare MSNs cause significant hemolysis, especially at high concentrations. Blood clot formation occurs during hemostasis to stop bleeding from damaged blood vessels. Some negatively charged porous materials, such as mesoporous silica and zeolites, can accelerate the hemostasis of the blood by activation of a coagulation cascade [167-169]. Similarly, when MSNs are injected into the blood, they can induce clotting inside blood vessels, which can cause adverse effects, by partially or completely blocking the blood vessels, leading to stroke and death [170-172]. Therefore, in order to use MSNs safely in biological applications, thrombogenicity of these materials should be determined. Another blood nanoparticle interaction to be considered before intravenous injection of the MSNs is non-specific protein adsorption, because it can promote phagocytosis by making the nanoparticles visible to phagocytic cells. This results in rapid clearance of nanoparticles from blood stream before they reach the target site and decreases the efficiency of applications [173, 174].

All of the above mentioned blood compatibility issues are closely related with the surfaces of the nanoparticles. Consequently, by engineering their surfaces; hemolytic activity, thrombogenicity and non-specific protein adsorption of MSNs can be

depressed or eliminated. Although there are some reports demonstrating modification of MSN surfaces with organic molecules, in particular polyethylene glycol (PEG), can decrease hemolysis, [17, 164] thrombogenicity [24, 175] and non-specific protein adsorption, [24] to our knowledge, there is no study that systematically investigates the surface effects on blood compatibility issues of MSNs. The aim of this study is to evaluate the effects of MSN surface composition on interaction of these particles with blood constituents (Figure 6.1). Accordingly, we prepared five organosilane functionalized MSNs and an equivalent non-functionalized MSN. We also prepared Rhodamine B dye conjugated MSNs to evaluate the effect of fluorescent tagging on blood compatibility of MSNs. In addition, we prepared a PEGylated MSN in order to compare our results with a prevalent and well-characterized surface. Beside surface composition, particle size, shape and porosity can also affect the interactions of MSNs with biological systems. Therefore, in this study particle size (around 80 nm), shape (spherical) and pore structure (hexagonally ordered 2-3 nm in size) of particles were kept constant, while their surfaces were differently functionalized. We selected the particle size around 80 nm because it was reported that around this particle size cellular uptake is maximum for MSNs [176] and also, it is well known that particles with sizes larger than 100 nm are rapidly cleared from the blood by the reticuloendothelial system [17]. We selected the surface functional groups by considering two characteristics: i) all surface functional groups were selected from previously used ones in MSN synthesis for different purposes such as controlling the cargo loading and release properties [177], fluorescent tagging [178], and improving the dispersibility of particles in biological media [54], ii) we select them to obtain a library of surface functionalities that covers diverse surface properties, anionic, cationic, neutral, hydrophobic or polar. To evaluate the blood compatibility of these MSNs, we examined hemolytic activity, thrombogenicity, and non-specific protein adsorption to their surfaces in a broad concentration range. The systematic evaluation of surface effects on blood compatibility of MSNs performed in this work can provide important insights about rational design of mesoporous silica systems for biomedical applications.

This work published on the Journal of Materials Chemistry B (2013, *1,* 1909-1920) journal. Reproduced with permission from The Royal Society of Chemistry.
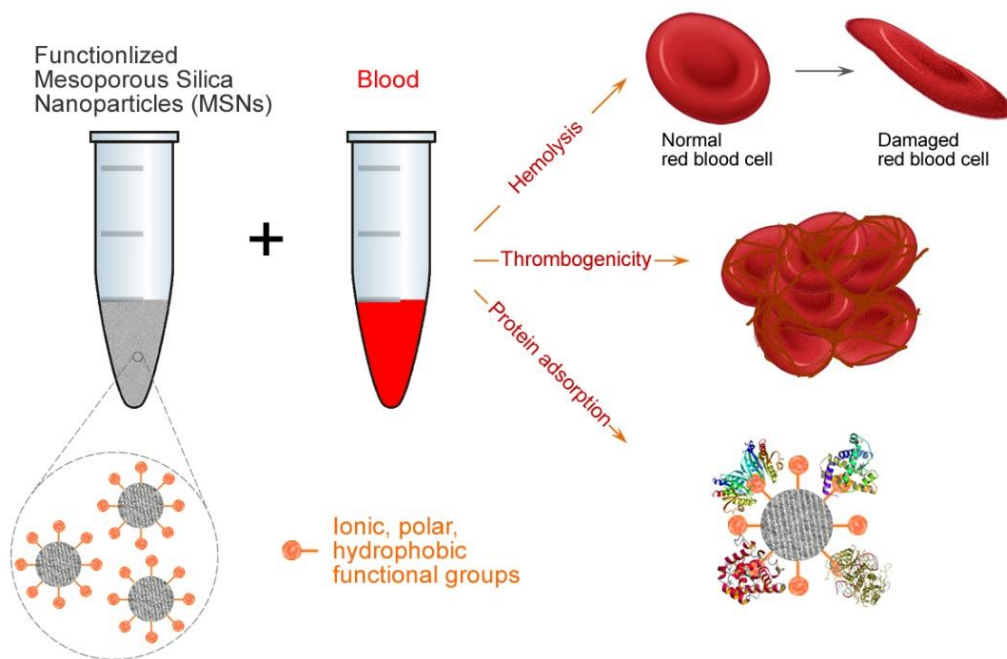
Figure 6.1: Schematic representation of certain interactions between mesoporous silica nanoparticles (MSNs) and blood constituents. Surfaces of MSNs were functionalized with ionic, polar, neutral or hydrophobic organosilane monomers to evaluate the effect of the surface chemical composition on blood compatibility of MSNs. They may cause hemolysis of red blood cells by deforming cell membrane during particle endocytosis and thrombogenicity by activation of blood coagulation cascade. Also, proteins can be non-specifically adsorbed to their surfaces which may reduce the blood circulation time of nanoparticles.

6.2 Experimental Section

Materials: Tetraetyl orthosilicate (TEOS), Aminopropyltriethoxysilane (APTES), Methyltrimethoxysilane (MTMS), Phenyltriethoxysilane (PTES), sodium hydroxide, ammonium nitrate, Rhodamine B, N-(3-Dimethylaminopropyl)-N′-ethylcarbodiimide hydrochloride (EDC) and N-Hydroxysuccinimide (NHS) were purchased from Merck (Germany), 3-(Trihydroxysilyl)propyl methylphosphonate (TSPMP), Human Serum Albumin (HSA), gamma globulins (γGs) from bovine serum, Polyethylene glycol (PEG, Mw = 10 kDa), pyridine, ethanol, hydrochloric acid (37%) (HCl), and n-hexane were purchased from Sigma-Aldrich (U.S.A.), Mercaptopropyltrimethoxysilane (MPTMS), 3-(triethoxysilyl) propylisocyanate (TESPIC), cetyltriammoniumbromide (CTAB), were purchased from ABCR (Germany), DMSO was purchased from Carlo-Erba (Italy) and all chemicals were used as purchased.

Synthesis of organosilane functionalized MSNs: All MSNs were synthesized by slightly modifying previous methods [45, 46, 101]. Briefly, 0.102 g CTAB was dissolved in 50 mL of deionized water and 0.3 mL of 2 M NaOH was added. The reaction mixture was heated to 70 °C and 0.5 mL of TEOS was rapidly added under vigorous stirring (600 rpm). After 15 min, for A-MSN 80 μL of APTES, for P-MSN 180 μL of TSPMP (42 wt. % in water), for M-MSN 49 μL of MTMS, for Ph-MSN 85 μL of PTES and for T-MSN 66 μL of MPTMS was added to satisfy 0.15 organosilane/TEOS molar ratio. All organosilane monomers except TSPMP were first dissolved in 0.5 mL of ethanol and this solution was added dropwise. TSPMP was directly added. The reaction mixture was further stirred for 105 min. Also a non-functionalized MSN was prepared without the addition of any organosilane monomers. Finally, particles were collected by centrifugation at 8500 rpm for 15 min and washed with ethanol twice. To extract CTAB, MSNs were dispersed in 50 mL of 20 g/L ammonium nitrate solution in ethanol and stirred vigorously at 60 °C for 30 min. This treatment was repeated twice and the particles were washed with ethanol afterwards. The washed particles were added to 50 mL of 5 g/L HCl solution in ethanol and stirred vigorously at 60 °C for 30 min. Then, particles were collected by centrifugation, washed with ethanol twice, and dispersed in 50 mL of ethanol.

Synthesis of Rhodamine B tagged MSN: To prepare R-MSN, 2 mg of RB dye was dissolved in 1 mL of DMSO and 9.3 μL of APTES was added. To this solution 3 mg EDC and 2 mg NHS was added and the reaction mixture was stirred at 200 rpm for 24 h at room temperature [178]. Then, dye solution was added to the reaction mixture immediately after TEOS addition, whereas other reaction parameters were kept the same as with the MSN case.

Synthesis of PEGylated MSN: PEG (Mw = 10 kDa) was coupled with TESPIC through addition reaction between hydroxyl groups of PEG and isocyanate groups of TESPIC to prepare PEG-silane monomer [24]. Before reaction, 100 mg PEG was dried at 90 °C in a vacuum oven for 18 h. The dried PEG was dissolved in 30 mL of dry pyridine under argon atmosphere by vigorous stirring at 70 °C for 6 h. Then, 2.63 mL of TESPIC was added to the reaction mixture and stirred for further 24 h. Pyridine was removed by rotary evaporation and a yellowish product was obtained. The raw product was washed twice with n-hexane. Then, the product was dissolved in ethanol at 35 °C

(at room temperature the product is poorly soluble in ethanol) and precipitated at 4 °C overnight. Finally, PEG-silane monomer precipitate was dissolved in 30 mL ethanol and stored at 4 °C.

To graft the PEG-silane to the MSN surface, 20 mg MSN was suspended in 24 mL of acidic (pH = 4) ethanol/water mixture (volume ratio, 1:2) and 1.5 mL of PEG-silane monomer solution was added to this solution under stirring at 600 rpm. After 24 h, the product was precipitated by centrifugation at 8500 rpm for 15 min and washed with water twice.

Hemolysis assay: Hemolysis experiments were performed according to previous reports [17, 164]. EDTA stabilized human blood samples were freshly obtained from volunteers at Bilkent University Health Center (Ankara, Turkey). First, 3 mL of blood was centrifuged at 1600 rpm for 5 min and blood plasma and surface layer was removed. Remaining RBC pellet was washed five times with 6 mL of PBS solution and RBCs were diluted in 25 mL of PBS solution. Then, 0.8 mL of MSNs solutions in PBS at different concentrations were added to 0.2 mL of RBC suspension. Also, positive and negative control samples were prepared by adding 0.8 mL of water and PBS, respectively to 0.2 mL of RBC solution. Then, samples were incubated at room temperature for 2 h. The samples were slightly shaken once for every 30 min to resuspend the RBCs and MSNs. After 2h, samples were centrifuged at 1600 rpm and 100 µL of supernatants was transferred to a 96-well plate. Absorbance of hemoglobin in supernatants was measured with a microplate reader at 570 nm. Also, absorbance at 655 nm was recorded as reference. Percent hemolysis values were calculated from three separate experiments. A Student's t-test was applied to all data sets and the difference between them accepted to be statistically significant when $p < 0.05$.

Coagulation assay: Samples for PT and aPTT were prepared according to a previous method [51]. Briefly, 40 µL of particles in PBS mixed with 360 µL of freshly prepared plasma from citrated blood samples, to give final particle concentrations of 0.1 or 1 mg/mL, and incubated for 5 min at 37 °C. Then particles were centrifuged and 50 µL portions of supernatants were used to measure PT and aPTT values using a semi-automatic blood coagulation analyzer (Tokra Medikal, Ankara, Turkey). Control samples were prepared using 40 µL PBS. All PT and aPTT values were calculated from at least three separate measurements.

Non-specific protein adsorption: Non-specific protein adsorption of MSNs were determined by mixing 0.5 mL of 0.6 mg/mL protein solution in phosphate buffer with 0.5 mL of MSN solution in PBS at 2 mg/mL for HSA and 1 mg/mL for γGs [24]. All samples were shaken for 2 h at 37 °C and then particles were precipitated by centrifugation at 8500 rpm for 15 min. The absorbance of proteins in the supernatants at 280 nm was recorded using a UV-Vis spectrophotometer. The adsorbed protein percentages were calculated using a calibration curve. Protein adsorption percentages were calculated from three separate experiments.

Characterization: Transmission electron microscopy (TEM) images were taken using a Tecnai G2 F30 (FEI) microscope. X-ray powder diffraction (XRD) spectra were taken using an X'pert Pro (Panalytical). Thermal gravimetric analyses (TGA) were performed with Q500, (TA Instruments). FTIR spectra of MSNs were collected by using a Fourier transform infrared spectrometer (FTIR, Vertex 70, Bruker). Zeta potentials of MSNs were measured with Zetasizer Nanoseries (Malvern Instruments). Optical absorption measurements of released hemoglobin were carried out using a Microplate reader (Spectramax M5, Molecular Devices). Optical absorption measurements of proteins were carried out using a UV-Vis-NIR Spectrophotometer (Carry 5000, Varian). Fluorescence spectrum of R-MSN was recorded with an Eclipse spectrophotometer (Varian).

6.3 Synthesis and Characterization of Surface Functionalized MSNs

Organosilane functionalized mesoporous silica nanoparticles were synthesized via sequential condensation of Tetraetyl orthosilicate (TEOS) and organosilane monomers in the presence of surfactant Cetyltriammoniumbromide (CTAB) in basic conditions. Five different organosilane monomers were selected to obtain MSNs with diverse surface properties (Table 6.1). Positively charged aminopropyl, negatively charged methylphosphonate, hydrophobic methyl and phenyl, and polar mercaptopropyl functionalized mesoporous silica nanoparticles were synthesized and named as A-MSN, P-MSN, M-MSN, Ph-MSN and T-MSN, respectively. All MSNs were

synthesized using 0.15 organosilane monomer/TEOS molar ratio and organosilane monomers were added 15 min after the TEOS addition to form organosilane rich surfaces [45]. Also, non-functionalized mesoporous silica nanoparticles (MSN) were prepared without addition of any organosilane monomer. In addition, we prepared fluorescently tagged MSNs using Rhodamine B (RB) dye, to evaluate the effect of fluorescent tagging on blood compatibility of MSNs. In order to attach the RB to silica network, we first conjugated it with APTES in the presence of EDC/NHS. Then TEOS and dye solution was polymerized in basic CTAB solution. All parameters were same with MSN synthesis except RB-APTES conjugate addition.

Sample	Surface Functionality	Method	Organosilane Monomer mol (%)[a]	Size (TEM) (nm)	d_{100}[b] (nm)	TGA Weight Loss (%)[c]	Organic Content mol (%)[d]
MSN	-OH	Co-condensation	0	78±15	4.18	7.0	0
A-MSN	$-(CH_2)_3-NH_2$	Co-condensation	15	75±14	4.18	15.4	8.7
P-MSN	$-(CH_2)_3-P(CH_3)O_3^-$	Co-condensation	15	81±12	4.13	10.3	1.6
M-MSN	$-CH_3$	Co-condensation	15	76±13	4.08	8.8	8.0
Ph-MSN	$-C_6H_5$	Co-condensation	15	83±11	4.13	16.3	8.5
T-MSN	$-(CH_2)_3-SH$	Co-condensation	15	82±15	4.06	15.4	7.8
R-MSN	$-(CH_2)_3-RB$	Co-condensation	n/a	62±12	4.3	11.5	n/a
PEG-MSN	$-[OC_2H_4]_n-OH$	Grafting	n/a	80±13	n/a	17.5	0.076

[a]Ratio to TEOS. [b]Interplanar spacing. [c]At 800 °C. [d]From TGA results.

Table 6.1: Physical properties of mesoporous silica nanoparticles.

PEGylated nanoparticles, as well as MSNs, have been studied by several groups and they were well-characterized in terms of hemolytic activity, thrombogenicity and non-specific protein adsorption [24, 175]. Therefore, in this study we also prepared a PEGylated MSN (PEG-MSN) as control. The PEG-MSN was synthesized according to a previous report [24]. In brief, PEG (molecular weight = 10 kDa) was grafted to the MSN surface after conjugation with TESPIC.

Figure 6.2a-d shows the TEM images of MSN (Figure 6.2a,b) and P-MSN (Figure 6.2c,d). The particle size distributions were calculated based on TEM images and given as insets in Figure 6.2a,c. Particle diameters of all MSNs (calculated from TEM images) are summarized in Table 6.1. All MSN are spherical and they have similar particle sizes around 80 nm with the exception of R-MSN, average particle diameter of R-MSN is 62 ± 12 nm, and they are fairly monodisperse. Also, after PEGylation a

thin organic layer is observed around MSN from the TEM image of PEG-MSN (Figure 6.3) and the particle size is slightly increased to 80 nm from 78 nm (Table 6.1).
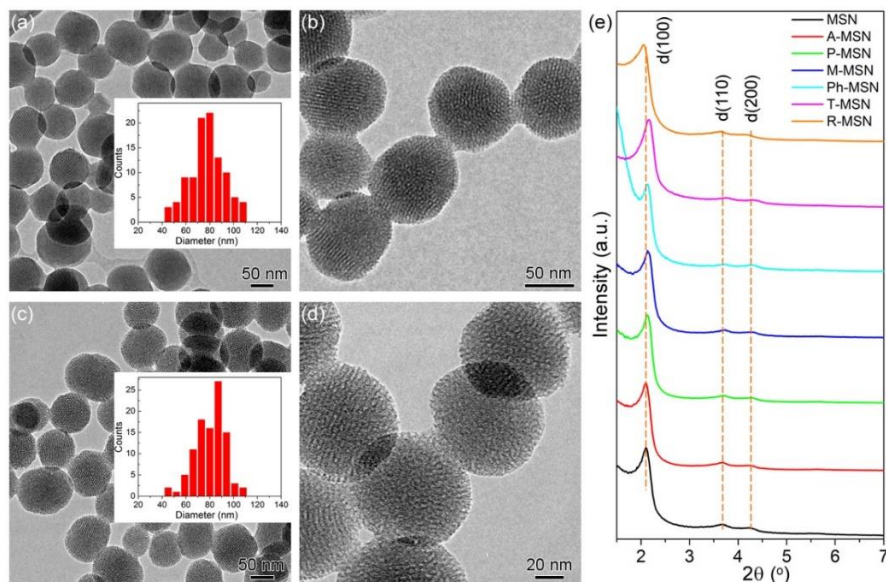
Figure 6.2: TEM images of (a,b) MSN and (c,d) P-MSN. The uniform size distribution and mesoporous structure of the particles can be clearly observed from TEM images. The insets in (a,c) shows the particle size distribution of MSN and P-MSN, respectively. (e) XRD spectra of all MSNs.

Mesoporous structure of the particles can be clearly observed from the TEM images and pore sizes were found to be around 2-3 nm. Pore structure of the particles was further investigated by XRD (Figure 6.2e). All particles exhibited characteristic diffraction peaks, (100), (110), and (200), of highly ordered hexagonal pore structure of MCM-41 type mesoporous materials. The interplanar d(100) spacing of all MSNs are given in Table 6.1. The d(100) values of particles are very close to each other (except R-MSN which is slightly higher than others) indicating that functionalization with organosilane monomers did not significantly affect the pore structure of MSNs. For R-MSN, observed decrease in particle size and increase in d(100) spacing are resulted from the interaction of bulky RB molecules with the CTAB micelles [179]. Nevertheless, R-MSN exhibits comparable particle size and pore structure with other particles.
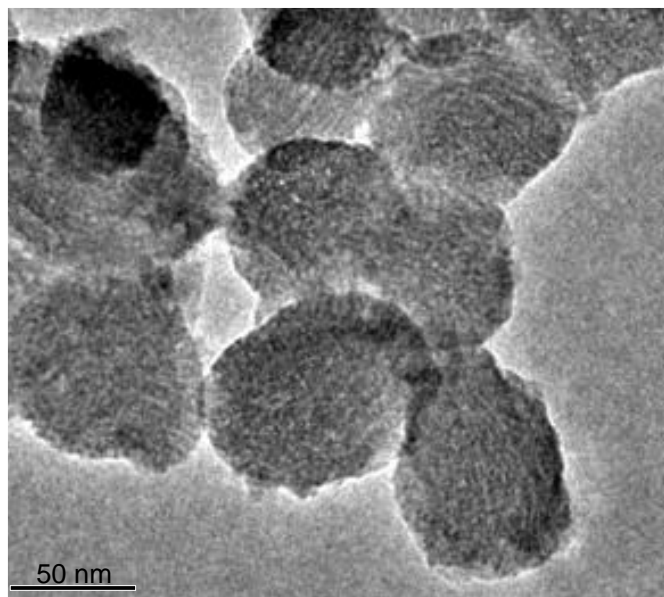
Figure 6.3: TEM image of PEG-MSN. Thin organic layer formed around the particles can be observed from the TEM image.

Functionalization of MSNs with organosilane monomers was verified by TGA and FTIR. The TGA spectra of all particles are given in Figure 6.4. The weight loss at 800 °C is between 8.8% and 16.3% for organosilane functionalized MSNs and 7% for bare MSN. The difference in weight loss between MSN and functionalized MSNs can be addressed to decomposable organosilane groups. Also, for PEG-MSN a large weight loss of 17.5% was observed. Based on TGA results, the molar organic content of functionalized MSNs were calculated and given in Table 6.1. For R-MSN it is impossible to calculate exact molar content of conjugated RB molecules because of the excess APTES monomer used during synthesis which can also bind to the silica network. Therefore, to further prove the successful RB conjugation we give the fluorescence spectrum of R-MSN (Figure 6.5), which demonstrates the bright fluorescence of R-MSN originated from RB dye. The organic contents of other particles are variable although they were synthesized in same conditions. For all MSNs except P-MSN, highly functionalized MSNs (7.8 to 8.7 mol %) were achieved. On the other hand, for P-MSN organic molar content is only 1.6%. The diversity of the organic content values can be attributed to difference in the reactivity of organosilane monomers in synthesis solution. Also, for PEG-MSN 0.076 mol % grafting of PEG molecules to the MSN surface was calculated according to the TGA results.
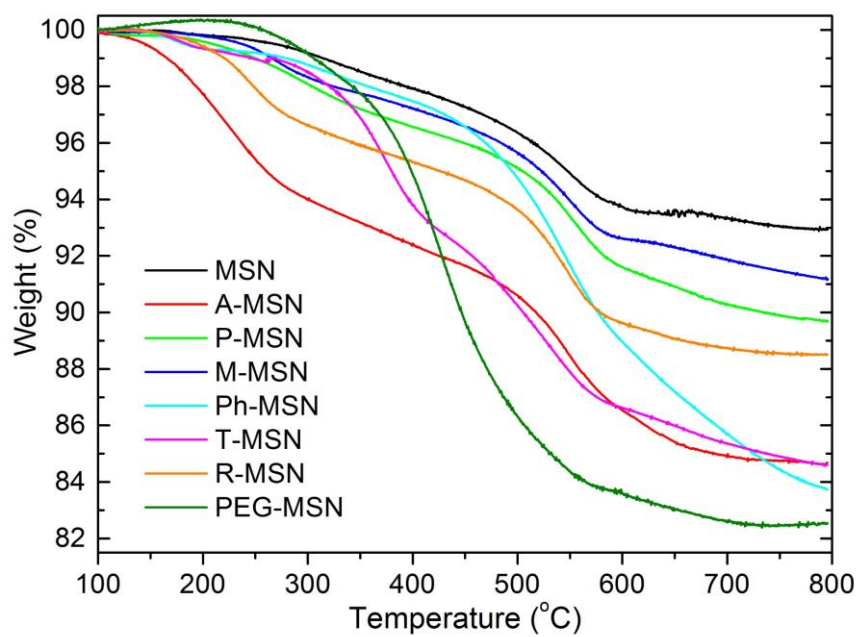
Figure 6.4: Thermo gravimetric analysis spectra of all MSNs.
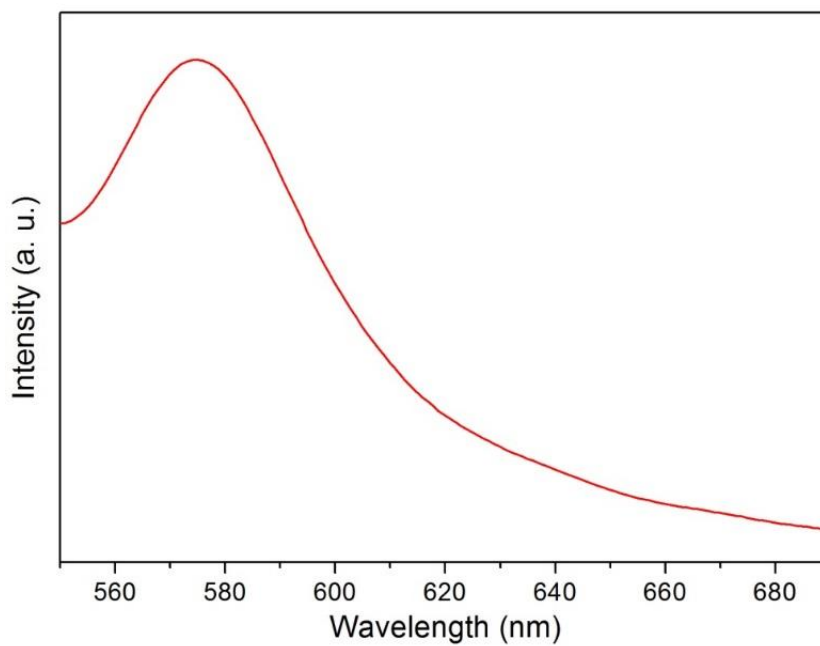
Figure 6.5: Fluorescence spectrum of R-MSN. The bright fluorescence of Rhodamine B dye can be clearly seen.

FTIR spectra of particles are given in Figure 6.6. The -CH absorption peak around 3000 cm^{-1} was observed for all functionalized particles indicating the presence of organic groups. Also, same peak was observed in bare MSNs spectrum which may be because of residual CTAB. Yet, the -CH absorption peak of bare MSNs was weaker than that of functionalized MSNs. Furthermore, some additional peaks were observed for functionalized MSNs. For example, for Ph-MSN the absorption peaks of aromatic ring at 700 and 740 cm^{-1} and for PEG-MSN the absorption peaks of C-H bonds at 1350 and 1465 cm^{-1} are clearly observable.
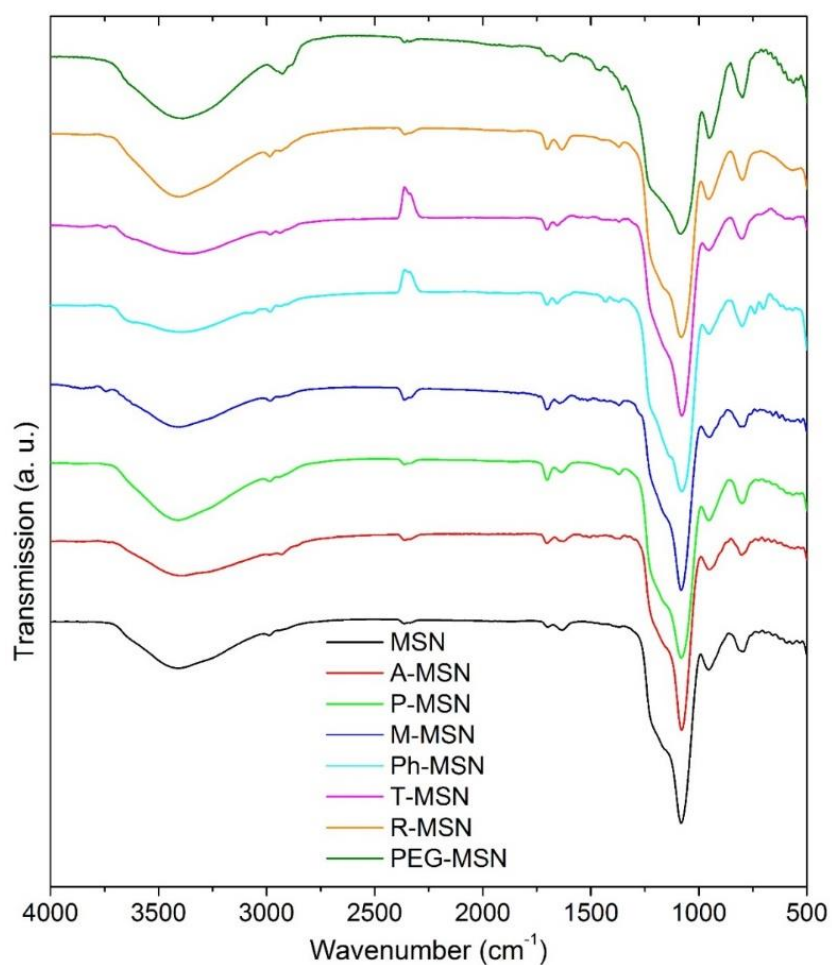
Figure 6.6: FT-IR absorption spectra of all MSNs. The C-H absorption peak around 3000 cm^{-1} is more distinct for functionalized MSNs.

The zeta potentials of MSNs in PBS solution were measured in order to characterize their surface properties (Table 6.2). The surface of bare MSN is highly negative; zeta potential is -22.4 mV, because of negatively charged silanol groups. Aminopropyl functionalized A-MSN exhibits positive surface charge (0.6 mV). The positive zeta potential is because of the replacement of silanol groups with positively charged aminopropyl groups. Also, positively charged RB conjugation increased the zeta potential of MSN to -9.77 mV. Surface modification with negatively charged methylphosphonate does not significantly affect the zeta potential (-21.7 mV) of the MSNs due to having the same charge with silanol groups. Also, for particles with uncharged functional groups (M-MSN, Ph-MSN, T-MSN, and PEG-MSN) zeta potential becomes less negative due to the replacement of silanol groups with uncharged groups.

Sample	Zeta potential (mV) in PBS at pH 7.4
MSN	-22.4
A-MSN	0.6
P-MSN	-21.7
M-MSN	-15.9
Ph-MSN	-20.4
T-MSN	-21.3
R-MSN	-9.77
PEG-MSN	-18.9

Table 6.2: Zeta potentials of mesoporous silica nanoparticles.

6.4 Hemolytic activity of Surface Functionalized MSNs

A hemolysis assay was used to determine the toxicity of MSNs on RBCs. 0.2 mL of isolated RBCs were mixed with 0.8 mL of nanoparticles in PBS to give desired. MSN concentration, at a range of 0.05 to 1 mg/mL, and incubated at room temperature for 2 hours. Also, positive and negative control samples were prepared by adding 0.8 mL of water and PBS, respectively to RBCs. For every 30 min precipitated cells and particles were resuspended by gentle shaking. Hemolytic activity of MSNs was determined by measuring the absorption peak of hemoglobin at 570 nm which was released to the solution from hemolyzed cells.

Hemolysis results for all MSNs are given in Figure 6.7. The highest hemolytic activity was observed for bare MSNs (5.5% at 0.1 mg/mL and 46.5% at 1 mg/mL). On the other hand, all MSNs functionalized with organic groups were demonstrated to have reduced or no hemolytic activity (Figure 6.7a). Also, photographs showing precipitated RBCs at the end of hemolysis experiment are given in Figure 6.7b. The red color of released hemoglobin from damaged cells is clearly observable for MSN, M-MSN, and Ph-MSN. For A-MSN, P-MSN, T-MSN, and PEG-MSN the supernatants are almost colorless at all concentrations. The functionalization of MSNs with charged or polar groups (A-MSN, P-MSN, T-MSN and R-MSN) can almost completely prevent the hemolytic activity. We observed 1.1%, 2.0% and 2.2% hemolysis percentages for P-MSN, T-MSN and R-MSN, respectively at 1 mg/mL and for all other cases there were no detectable hemolysis for these three MSNs. Also, surface modification with PEG significantly reduced the hemolytic activity of MSN (1.1% at 1 mg/mL) as previosuly reported [24]. Surface modifications with hydrophobic methyl and phenyl groups did not completely prevent the hemolytic activity but significantly reduced it. Ph-MSN did not exhibit any hemolytic activity up to 0.25 mg/mL; however, after that concentration the hemolysis percentage dramatically increased. M-MSN exhibited hemolytic activity for all concentrations, yet it was lower than hemolytic activity of MSNs for all cases.

It was reported that hemolysis assays may give false negative results because of adsorption of hemoglobin on particle surfaces [180] and false positive results because of the toxicity of residual CTAB surfactant [17]. The adsorption of hemoglobin on particle surfaces can cause the removal of hemoglobin from the solution during centrifugation; therefore, lower hemolysis percentages than their actual values might be calculated. To investigate the adsorption of hemoglobin on MSN surfaces, we incubated MSN and A-MSN with positive control sample (all RBCs are lysed with deionized water and all hemoglobin is released) for two hours (final particle concentration is 1 mg/mL) and absorbance of hemoglobin at 570 nm was measured after precipitating MSNs with centrifugation. There is no significant difference between MSN and A-MSN treated and control samples. Thus, it can be said that only a small percentage of total proteins in the solution adsorbed on the surface of nanoparticles. The possible hemolysis due to toxicity of residual CTAB was

investigated by treating the RBCs with the supernatant of 1mg/mL MSN solution for two hours. The supernatant did not cause any hemolysis. Therefore, we verified that adsorption of hemoglobin by MSNs or toxicity of residual CTAB effects does not interfere with the hemolysis assay used in this study.
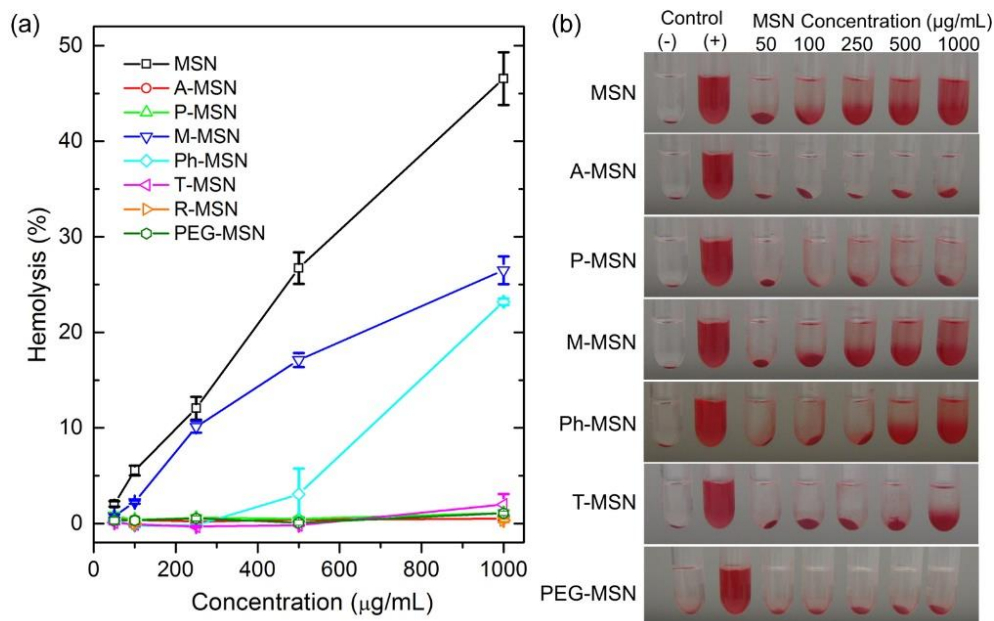
Figure 6.7: (a) Hemolysis percentages of all MSNs at different concentrations between 0.05 and 1g/mL, which were incubated with RBCs for 2 h. Data generated from three independent experiments. All functionalized MSNs demonstrated lower hemolytic activity compared to bare MSN at all concentrations. Furthermore, for A-MSN, P-MSN, T-MSN, R-MSN and PEG-MSN almost no hemolytic activity was detected. (b) Photographs of RBCs threated with all MSNs at different concentrations. The released hemoglobin from the damaged cells in the supernatant can be seen from the photographs. (-) and (+) controls are the RBCs in PBS and water, respectively. Student's t test analyses revealed the statistical significance of the data (p<0.0001).

We also examined the effect of surface functional group density on hemolysis by aminopropyl functionalized particles prepared using APTES to TEOS molar percentages between 2.5% and 15%. The MSNs were named as A_x-MSN; where x is the APTES to TEOS molar percentage. All aminopropyl functionalized MSNs are listed in Table 6.3. The organic content of the MSNs were determined using TGA method. The weight loss of MSNs gradually increases with increasing APTES amount as expected. Based on TGA results, organic contents of the A-MSNs were calculated

and given in Table 6.3. The zeta potentials of the particles were also given in Table 6.3. As the APTES ratio decreases the zeta potential of the particles becomes more negative because of reduction in the number of positively charged surface aminopropyl groups.

Sample	TGA Weight Loss (%)[a]	Organic Content mol (%)[b]	Zeta potential (mV)
A_{15}-MSN	15.4	8.7	0.6
A_{10}-MSN	14.2	7.6	-3.1
A_5-MSN	13.1	6.4	-8.1
$A_{2.5}$-MSN	11.6	4.8	-10.5

[a]At 800 °C. [b]From TGA results

Table 6.3: Organic contents and zeta potentials aminopropyl functionalized MSNs.

Hemolysis caused by aminopropyl modified MSNs at 0.1 and 1 mg/mL particle concentrations are given in Figure 6.8. The hemolytic activity of the MSNs significantly reduced even at low amounts of (2.5%) aminopropyl functionalization. We observed 2.2% hemolysis only when the cells incubated with A2.5-MSNs at 1 mg/mL. At same concentration bare MSN particles induced 46.5% hemolysis. For all other cases there was no detectable hemolysis for A-MSNs.
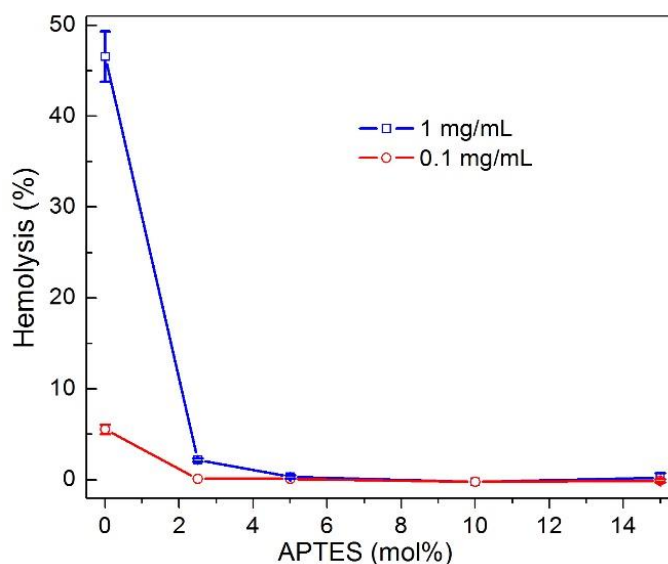
Figure 6.8: Hemolytic activity of MSNs functionalized with APTES between 2.5 to 15 molar % with respect to TEOS. Student's t test analyses revealed the statistical significance of the data ($p < 0.0001$).

Lastly, we showed that high hemolytic activity of the MSN can be reduced by interacting particles with human serum albumin (HSA) before the hemolysis experiment. 2.5 mg/mL of MSNs in PBS were incubated with different amounts of HSA for 1 h. The HSA concentration was varied between 0.01 mg/mL and 1 mg/mL. The hemolysis results of MSNs pre-interacted with HSA at 1 mg/mL particle concentration, (Figure 6.9) revealed a gradual decrease in the hemolytic activity of MSNs with increasing HSA concentration. At 1 mg/mL HSA concentration we observed a hemolytic activity of only 1%.
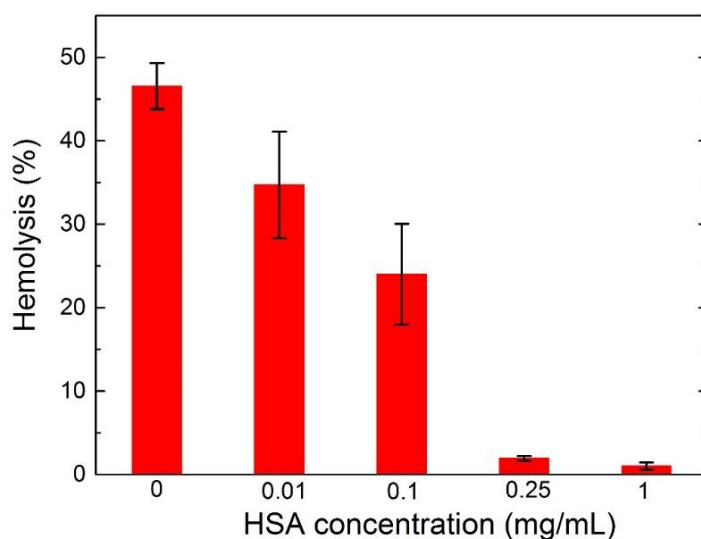
Figure 6.9: Hemolysis results of HSA coated MSNs. With increasing HSA concentration reduced hemolytic activity was observed.

6.5 Effect of Surface Functionalized MSNs on Blood Coagulation

To study the thrombogenicity of the MSNs, we measured the PT and aPTT of nanoparticles at two different particle concentrations, 0.1 mg/mL and 1 mg/mL. PT is used to investigate extrinsic coagulation pathways and aPTT is used to investigate intrinsic coagulation pathways. Also, both methods are used to evaluate the common coagulation pathways [51]. Figure 6.10 shows the PT and aPTT results of MSNs. The

PT and aPTT results revealed that none of the functionalized or bare particles result in a significant activation of common, intrinsic or extrinsic pathways of coagulation.
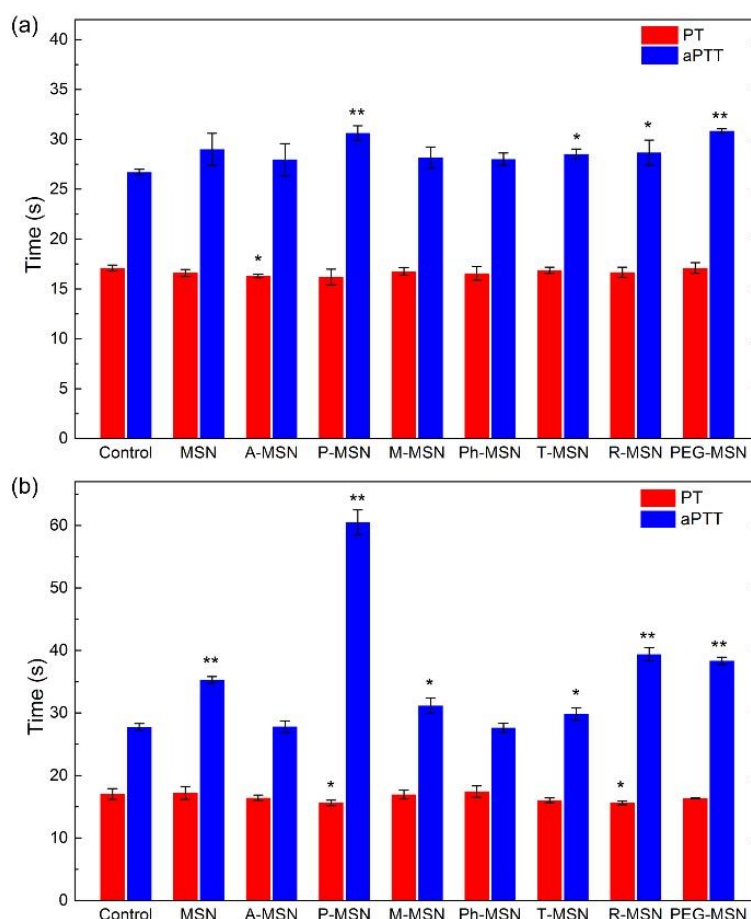
Figure 6.10: (a) 0.1 mg/mL particle concentration. All PT and aPTT values are within their normal range. (b) 1 mg/mL particle concentration. All PT values are within their normal range; however, aPTT values for R-MSN and especially P-MSN is higher than normal value, which indicates that these particles inhibit the intrinsic pathways of coagulation at this concentration. Data were generated from at least three independent experiments. According to Student's t test, *p<0.05 and ** p<0.0001.

Administration of MSNs to the blood serum slightly reduced the PT compared to control at both concentrations; however all values were within the expected range (*i. e.* ratio between PT values of MSN treated serum and control serum is between 0.82 and 1.15). Also, we did not observe any alteration in the aPTT of MSNs at 0.1 mg/mL. All aPTT values were in their normal range, which is between 25 and 36 s. However, at 1 mg/mL we observed significantly prolonged coagulation times for MSN, P-MSN,

R-MSN and PEG-MSN. In addition, aPTT of P-MSN is significantly higher than upper limit of the normal values which is 60.5 ± 2 s. In other words, P-MSN showed moderate anticoagulation behavior at 1 mg/mL concentration by inhibiting the intrinsic pathways of coagulation [181].

6.6 Non-Specific Protein Adsorption onto Surface Functionalized MSNs

We studied non-specific protein adsorption on surfaces of MSNs using HSA and γGs which are the mostly abundant proteins in the human blood (HSA is 60% and Gs is 18% percent of the total serum proteins) [24]. Also, γGs adsorption to nanoparticle surfaces is particularly important because these proteins can mark the foreign particles and make them visible to mononuclear phagocyte system (opsonization) which leads rapid clearance of nanoparticles from blood [182]. Particles in PBS were mixed with protein solution in phosphate buffer (pH 7.4) to give final concentration of 0.3 mg/mL proteins. The solutions were shaken at 37 °C for 2 hours and the nanoparticles were precipitated by centrifugation. The percentage of adsorbed proteins on MSNs was calculated by monitoring the absorption band of proteins at 280 nm before and after interacting with MSNs.

Figure 6.11 shows the amount of adsorbed proteins on nanoparticle surfaces compared to MSN. Also, adsorbed protein amounts are listed in Table 6.4. PEGylation significantly reduced the non-specific protein adsorption to the MSN surface, as previously reported [24]. Interestingly, protein adsorption of A-MSN and especially P-MSN are significantly lower than MSN for both HSA and γGs. Modification of MSN surface with small methyl groups did not significantly affect the protein adsorption properties. On the other hand, phenyl and mercaptopropyl modification largely increases the HSA and γGs adsorption to the MSN surfaces. Lastly, positively charged and hydrophobic RB modification resulted in a slight increase in HSA adsorption but significant decrease in γGs adsorption.
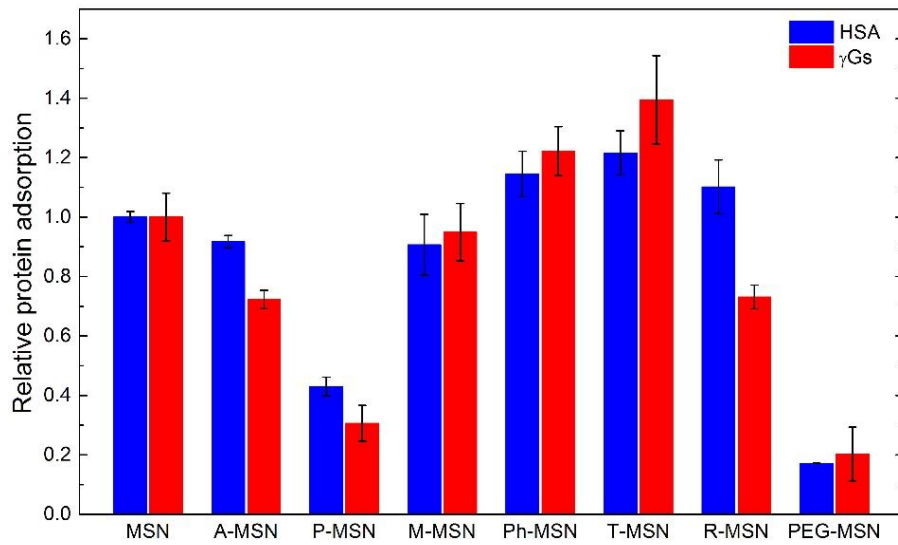
Figure 6.11: Protein adsorption percentages of nanoparticles. Data were generated from three independent experiments.

	Adsorbed protein (nmol/mg MSN)	
Sample	**HSA**	**γGs**
MSN	6.98 ± 0.12	1.28 ± 0.1
A-MSN	6.4 ± 0.14	0.92 ± 0.04
P-MSN	3.0 ± 0.2	0.39 ± 0.08
M-MSN	6.32 ± 0.66	1.22 ± 0.12
Ph-MSN	8.0 ± 0.5	1.56 ± 0.1
T-MSN	8.5 ± 0.48	1.78 ± 0.18
R-MSN	7.7 ± 0.58	0.94 ± 0.05
PEG-MSN	1.2 ± 0.004	0.26 ± 0.12

Table 6.4: Protein adsorption amounts of MSNs.

6.7 Discussion on Blood Compatibility of MSNs

Blood compatibility is probably the most critical issue regarding administration of MSNs as drug or biomolecule carriers and theranostic agents, not only because their interactions with blood constituents in circulatory system can result in significant toxicity to organisms, but also cell membrane-nanoparticle interactions are quite similar for all cell types. Surface composition of MSNs is one of the predominating factors determining these interactions, which fundamentals have not been elaborately comprehended yet. In this context, we systematically studied blood compatibility of mesoporous silica nanoparticles possessing ionic, hydrophobic or polar surface

functional groups, in terms of their hemolytic activity, thrombogenicity and non-specific protein adsorption.

There are some reports [24, 161, 164] that investigate surface effects on interactions of MSNs with biological systems in terms of cellular uptake, cytotoxicity, hemolytic activity and non-specific protein adsorption. However, previous reports generally categorized the surfaces simply as positive (aminopropyl modified), negative (bare) and neutral (PEGylated). On the other hand, our research demonstrates that interactions between MSN surface and biological systems are much more complicated than that and cannot be evaluated on the basis of only surface charge. For instance, bare MSN and P-MSN both demonstrates highly negative surface charge; but their hemolytic activity, thrombogenicity and non-specific protein adsorption properties are all completely different.

Recently, Slowing *et al.* [164] observed that hemolytic activity of MSNs can be prevented by modifying the surface with some ionic surface functional groups, such as aminopropyl and carboxylic acid. On the contrary, Yu *et al.* [166] reported that aminopropyl modification increases the hemolytic activity of silica nanoparticles. Also, there is a disagreement in the origin of the hemolytic activity of silica nanoparticles. Slowing *et al.* [164] claimed that the hemolytic activity of silica nanoparticles is related with the surface silanol groups; on the other hand, Yu *et al.* [166] concluded that it is related with the zeta potential of the surface. Therefore, to clarify these points and understand the surface effects on hemolytic activity elaborately, in this study we used a large library of surface functional groups with different characteristics (*i. e.* hydrophobic, aromatic, polar, neutral, positively charged and negatively charged). Our results (Figure 6.7) indicate that there is no correlation between net surface charge (zeta potential) and hemolytic activity of MSNs (in the studied zeta potential range, between -22 and 1 mV); instead it is very specific to number of accessible surface silanol groups regarding the RBC membrane. We observed that hemolytic activity of MSNs can be prevented almost completely in the studied concentration region, by modifying the MSN surfaces with bulky -compared to other functional groups- aminopropyl, methylphosphonate propyl, mercaptopropyl, RB and PEG moieties. The improved compatibility of these MSNs with RBCs is mainly resulted from reduced number of accessible surface silanol groups by steric

96

hindrance of the bulky functional groups. Also, A-MSN, T-MSN, R-MSN and PEG-MSN are not expected to electrostatically interact with positively charged trimethyl-ammonium head groups of the cell membrane lipids since their functional groups are positively charged or neutral at pH 7.4 [183]. In addition, we observed that even a small amount of positively charged and bulky aminopropyl functionalization can dramatically reduce the hemolytic activity of MSNs (Figure 6.8) by preventing the interaction of silanol groups with cell membranes. Furthermore, the silanol specificity of hemolytic activity of silica particles was also shown by coating the particles with HSA. The HSA corona formed around the particles blocks the surface silanol groups and results in a significant decrease in the hemolytic activity [184].

Interestingly, negatively charged P-MSN (zeta potential is -21.7 mV, which is very close to that of bare MSN) also did not cause significant hemolysis although electrostatic interaction between methylphosphonate and positively charged RBC membrane could be expected. The energy released from the binding of the MSN on the RBC membrane and the free energy required for bending of the RBC membrane around MSNs are two competitive parameters that determine the interaction among MSNs and RBCs. If energy released thorough binding is greater than energy required for bending, endocytosis of MSNs is occurred [183, 185]. The released energy during binding of P-MSN to the RBC membrane is expected to be less than the released energy during MSN binding, because methylphosphonate is a softer ligand than silanol, which may not meet the energy required for excessive membrane bending needed for endocytosis of particles. It can be concluded that P-MSN did not cause any significant hemolysis because of its low binding affinity to RBC membrane.

Also, small methyl and phenyl functional groups can decrease the hemolytic activity of MSNs to a degree. One reason of lower hemolytic activity of these particles relative to the bare MSNs may be the replacement of some surface silanol groups with metyl and phenyl groups. In addition, methyl and phenyl groups can also hinder the interaction among silanol groups and RBC membrane however; they might be not bulky enough to prevent the interaction completely.

It has been reported that dry mesoporous silica materials can be used to increase the rate of hemostasis by activating coagulation pathways due to their high absorption capacities [169]. However, PT and aPTT results revealed that MSNs prepared in this

97

work did not activated extrinsic, intrinsic or common coagulation pathways up to a concentration of 1 mg/mL. This guarantees that particles do not have any thrombogenic activity in the studied concentration region. The observed low coagulant behavior of MSNs can be explained by the already PBS filled pores of these materials, which significantly diminish the absorption capacity of particles compared to their dry state [51, 175]. Also, it should be noted that, the highest concentration used for thrombogenicity experiments in this study, 1 mg/mL, was roughly equal to a particle dose of 100 mg/kg [18], which is a sufficient dose for intravenous applications of MSNs [186].

Surprisingly, we observed significantly prolonged aPTT value for P-MSN at 1 mg/mL, which indicate that P-MSN can inhibit the intrinsic coagulation pathways, but it doesn't have any significant effect on extrinsic coagulation pathways. Mechanisms causing the anticoagulant behavior of P-MSN are beyond the extent of this study, but definitely further experiments are required.

As in hemolytic activity experiments, there is no correlation between surface charge of particles and their thrombogenicity. Negatively charged P-MSN showed significant anticoagulant behavior at 1 mg/mL concentration; however bare MSN did not show any anticoagulant behavior. Also, P-MSN and R-MSN were modified with negatively and positively charged functional groups, respectively, but both showed prolonged aPTT.

Protein surface is heterogeneous and contains charged, polar and hydrophobic moieties. Due to their various surface groups they can easily adsorb onto the surfaces via many interactions such as ionic and hydrophobic interactions and hydrogen bonding. Consequently, when nanoparticles are injected into the blood their surface is rapidly covered with a layer of blood proteins called as protein corona [173, 187-189]. For many biological applications, the non-specific protein adsorption on the nanoparticle surfaces is undesirable because it increases the uptake of nanoparticles by immune cells, which reduce the blood circulation times. For effective use of nanoparticles in biological applications non-specific protein adsorption must be prevented or reduced to an appropriate level [171].

We observed significantly lower protein adsorption for A-MSN, P-MSN and PEG-MSN than bare MSN. Although ionic aminopropyl and methylphosphonate propyl

groups are expected to interact with proteins mainly through hydrogen bonding and ionic interactions, as silanol groups of MSN, the lower protein adsorption of A-MSN and P-MSN may arise from the steric repulsion of flexible propyl chains of their functional groups [24]. For M-MSN there is no statistically significant difference from MSN in adsorbed protein amounts which is because of the methyl groups are not large enough to prevent interaction of silanol groups with proteins. On the other hand phenyl and mercaptopropyl modification largely increase the protein adsorption for both HSA and γGs. The higher adsorption capacity of Ph-MSN and T-MSN can be attributed to their more complex surface structures, which can provide additional interactions; such as hydrophobic and polar interactions, for protein binding. For R-MSN increased HSA adsorption and reduced γGs adsorption compared to MSN was observed. The high HSA adsorption of R-MSN can be attributed to its higher surface area than other particles due to its smaller particle size. However, R-MSN still adsorbs less γGs compared to MSN.

PEGylated surfaces are for long known as protein resistant due to their hydrophilic and flexible nature [190]. Accordingly, Wang *et al.* [49] and He *et al.* [24] showed that protein adsorption on MSN surface can be significantly reduced by grafting their surfaces with PEGylated coatings. Similarly, in this work 83% reduction in γGs and 80% reduction in HSA adsorption was observed for PEG-MSN. Surprisingly, here we observed comparable results (70% decrease for γGs and 57% decrease for HSA) that can be achieved by modifying the MSN surface with a small organosilane ligand; methylphosphonate propyl using a facile one-pot method.

Chapter 7

Fluorescent Dopamine Sensing Based on *in Situ* Formation of Visible Light Emitting Polydopamine Nanoparticles

7.1 Introduction

Dopamine (DA), a catecholamine neurotransmitter, regulates many biological processes in central nervous, hormonal, and cardiovascular systems [191, 192]. Abnormal DA concentrations in biological fluids (*e. g.* urine, blood plasma and extracellular fluid of the central nervous system) can be indicator of several diseases such as schizophrenia and Huntington's and Parkinson's diseases [193-195]. In this regard, sensitive and selective measurement of DA levels is important for diagnosis of these diseases and monitoring of patients [196]. Common DA detection methods utilize electrochemical analysis, [197-199] chromatography coupled with spectroscopy [200, 201] (*e. g.* HPLC-fluorescence and GC-MS) and fluorescent [202-206] or colorimetric probes [191, 207] (*e. g.* organic dyes, quantum dots and gold nanoparticles). These methods, however, have some limitations. For instance, interference from uric acid (UA) and ascorbic acid (AA) largely limits selectivity of electrochemical methods. Chromatographic methods on the other hand, are time consuming, labor intensive and expensive with complicated procedures. Similarly,

synthesis of fluorescent or colorimetric probes for DA detection involves complicated and time consuming procedures.

A straightforward, cost-effective and rapid alternative for DA detection is measuring the optical absorption of oxidation product of dopamine under alkaline conditions [208-212]. These assays use only a common base (*e. g.* NaOH) or other oxidants (*e. g.* enzymes) as reagent and DA concentration is determined by simply measuring the optical absorption of resulting brownish oxidation product. Unfortunately, the method demonstrates a poor sensitivity around a few μM. In these oxidation studies, the product is assumed as quinone derivative of dopamine [208]. However, recent studies demonstrated that under alkaline conditions the quinone product is unstable and rapidly polymerized by covalent attachment and aggregation [213-215]. The resulting polymer is commonly referred as polydopamine (PDA) which is structurally very similar to the natural eumelanin polymers [216]. Although, fluorescence property of eumelanins is known for more than 40 years and there is an ongoing research to understand the interesting optical properties of these materials; [217-219] the fluorescence of PDA is largely unexplored. To our knowledge, only very recently Zhang *et al.*, [220] reported that purified PDA nanoparticles are fluorescent and can be used for cellular imaging.

Here, we explored the intrinsic emission properties of PDA nanoparticles which were synthesized by oxidizing DA under different conditions, and demonstrated that it can be used as turn-on type fluorescent reporter of DA existence. The introduced method is based on monitoring the visible light emission of *in situ* synthesized PDA nanoparticles and it is capable to detect very low DA concentrations (detection limit is 40 nM). Note that, reached detection limit is 20 to 750 fold better than the methods that measure the absorption of oxidization solution of DA. Initially, we studied the fluorescence property of PDA synthesized under different basic conditions. We observed that the emission spectrum of PDA is very dependent on time, and base type and its concentration. Then, under optimized conditions, we performed DA sensing experiments. Finally we showed that the method is very selective to DA and no interference from AA or UA is observed.

This work published on the Analytical Chemistry journal. Reproduced with permission from The American Chemical Society.

7.2 Experimental Section

Materials: Dopamine, ascorbic acid, glucose, urea, sucrose, aspartic acid, alanine, glycine, lysine, hydrochloric acid (37%) were purchased from Sigma-Aldrich (U.S.A.), sodium hydroxide was purchased from Merck (Germany). All chemicals were used as purchased.

Oxidization of dopamine: 1.8 mL of freshly prepared dopamine (100 µM) solutions in phosphate buffered saline (PBS) (2 mM, pH 7.4) were oxidized by dropwise addition of 200 µL of Tris base (final concentration in the solution is 10 mM) or NaOH (final concentration in the solutions are 0.5 mM, 10 mM and 20 mM) stock solutions. Time dependent evaluation of UV-Vis or fluorescence spectra of the solutions were *in situ* recorded using UV-Vis absorption (Cary 5000, Varian) and fluorescence (Eclipse, Varian) spectrophotometers, respectively.

Characterization of polydopamine nanoparticles: 5.4 mL of dopamine solutions (100 µM) in PBS was polymerized using 0.6 mL of NaOH (final concentration in the solution is 20 mM) for 3 h. Then the particles were purified using membrane dialysis. 2 µL of purified particles dripped on a Transmission electron microscopy (TEM) grid and morphology of the particles were investigated using a TEM (Tecnai G2 F30, FEI). For dynamic light scattering (DLS) measurements 100 µM of dopamine polymerized in PBS for 3 h. Then particles filtered with 1 µm syringe filter and their size distribution measured with Zetasizer Nanoseries (Malvern Instruments).

Stopping the oxidization reaction: In order to stop polymerization reaction excess acid can be added to the polymerization solution. For instance, 2 mL of dopamine oxidization solution in which final concentrations of dopamine and NaOH are 100 µM and 20 mM, respectively, is stopped using 42 µL of 1 M HCl.

Sensitivity and selectivity experiments: Freshly prepared dopamine stock solutions were diluted in PBS to give final volume of 1.8 mL and concentrations ranging from 0.1 to 20 µM. Polymerization reactions were initiated using 200 µL of NaOH (final concentration is 20 mM). After 30 min, reactions were stopped using 42 µL of 1 M HCl and solutions were further incubated for 10 min. Fluorescence spectra of solution were recorded (excitation wavelength is 370 nm). For selectivity experiments concentration of all interfering chemicals (ascorbic acid, uric acid, urea, glucose,

sucrose, aspartic acid, lysine, alanine and glycine) was 0.1 mM and other parameters were same with the sensitivity experiments. All experiments were performed in triplicate.

Absorption based assay: The samples were prepared using the same experimental parameters with the fluorescence assay. Absorption of DA oxidization solutions (DA concentration were between 0.5 and 20 µM) at 360 nm were recorded using a UV-Vis absorption (Cary 100, Varian) spectrophotometer.

7.3 Synthesis and Characterization of Fluorescent Polydopamine Nanoparticles

Under alkaline conditions DA is spontaneously oxidized to its quinone derivative and then auto-polymerized to form PDA (Figure 7.1) [213, 214].
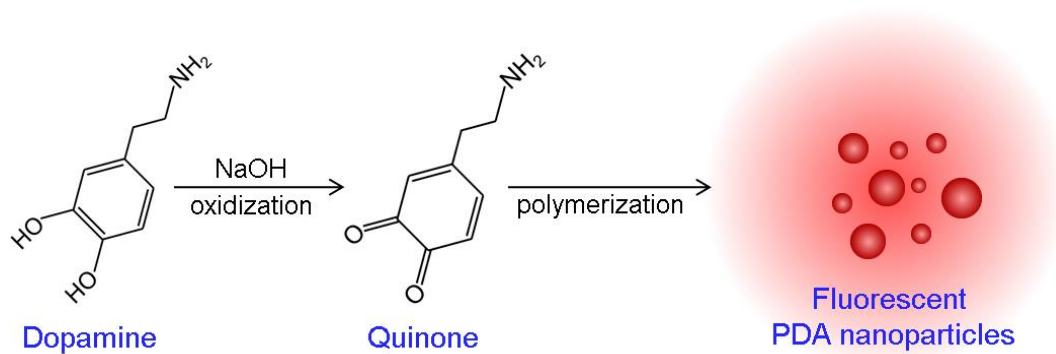
Figure 7.1: Schematic representation of fluorescent PDA nanoparticle formation.

Polymerization of DA solution (1 mM) in PBS (pH 7.4) was *in situ* investigated using UV-Vis spectroscopy for 3 h (Figure 7.2). After NaOH addition (final concentration is 20 mM), a peak around 350 nm appeared which indicates the quinone formation [214] and its intensity gradually increased for 3 h. The broad peak around 470 nm shows the intramolecular cyclization of the quinone derivative [214] which is an intermediate product in the polymerization of DA (Figure 7.2, inset) [213]. After 10 min this broad peak disappeared and absorption at all wavelengths between 400 and 700 nm increased gradually which shows the formation of PDA [214].
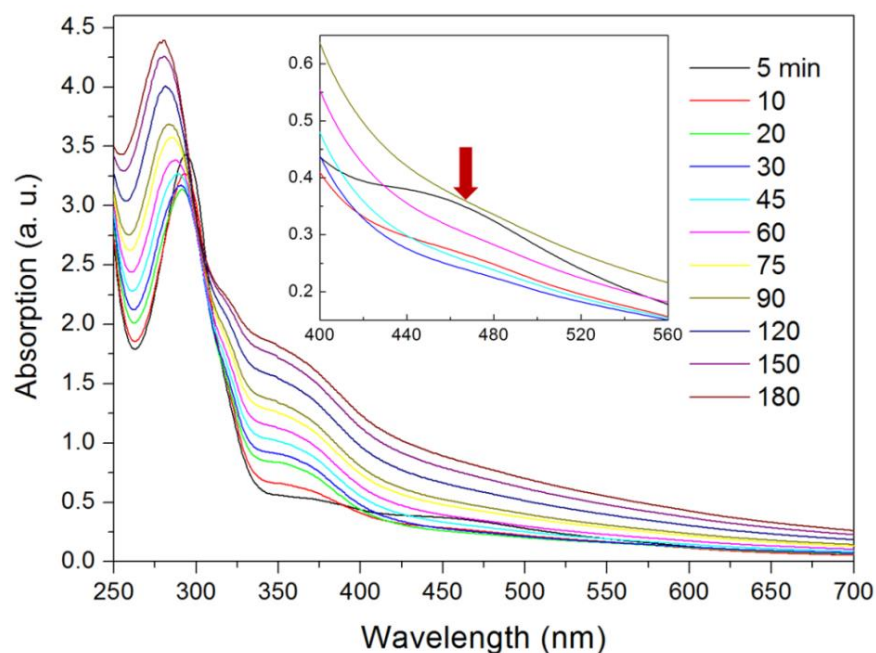
Figure 7.2: Time dependent UV-Vis absorption spectra of 1 mM DA solution. Oxidization is started using 20 mM (final concentration) NaOH. The broad band increase in the absorption indicates PDA formation. Inset shows the peak formed around 470 nm at the first stages of polymerization.

In order to characterize the PDA nanoparticles formed after 3 h of oxidization reaction, we polymerized 100 μM DA using 20 mM NaOH. Particle size distribution of PDA nanoparticles is given in Figure 7.3 which shows the broad size distribution of particles with diameters ranging from a few nanometers to hundreds of nanometers. Figure 7.3 inset shows the TEM image of 3 h oxidized PDA particles. PDA nanoparticles were irregular in shape and have broad particle size distribution which is in accordance with DLS results.
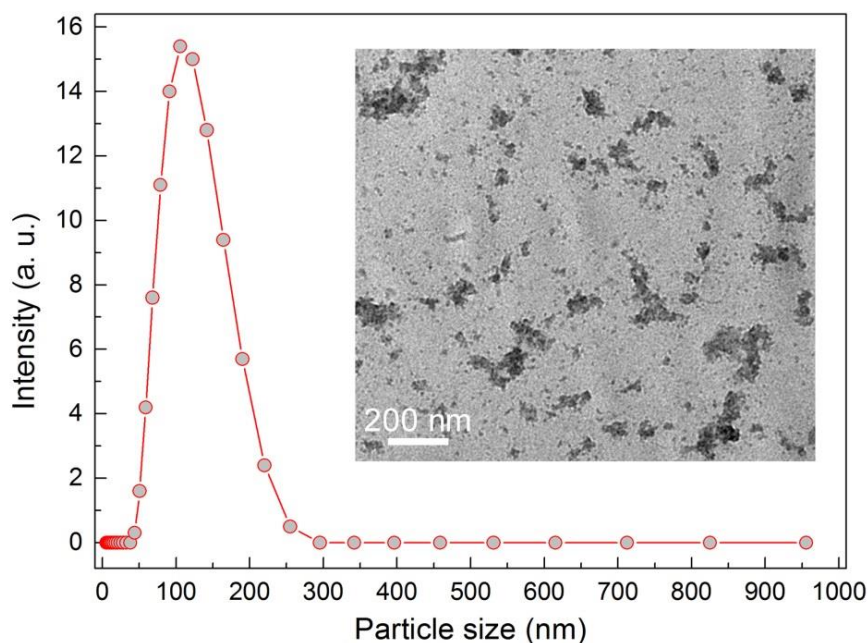
Figure 7.3: Particle size distribution of PDA nanoparticles. Graph shows the particle size distribution of PDA nanoparticles which were prepared after oxidization of 100 μM DA solution for 3 h in the presence of 20 mM NaOH. Inset shows the TEM images of the purified DA oxidization solution showing the polydisperse and irregularly shaped PDA nanoparticles.

The resulting PDA nanoparticles are intrinsically fluorescent (will be discussed in detail below). Initially, we explored the effect of different oxidation conditions on the fluorescence of oxidation product of DA (*i. e.* PDA nanoparticles) in order to determine optimum experimental conditions for DA sensing. We compared two bases that are commonly applied in DA oxidization; [208, 213] Tris base and NaOH at same pH and molarity. We measured the *in situ* fluorescence of 100 μM DA which is oxidized under different basic conditions, for 1 h and compared the fluorescence intensities at 510 nm at different time intervals. The results are presented in Figure 7.4 and Figure 7.5. At same pH value (9.6) Tris is more effective than NaOH in terms of generating fluorescent PDA nanoparticles. On the other hand, at same molarity (10 mM), NaOH is almost two times more effective than Tris base. Also, we explored fluorescence of polymerization solution at different NaOH concentrations and we selected 20 mM as optimal for the sensing experiments. Therefore, we used 20 mM NaOH to oxidize DA in the rest of the study.
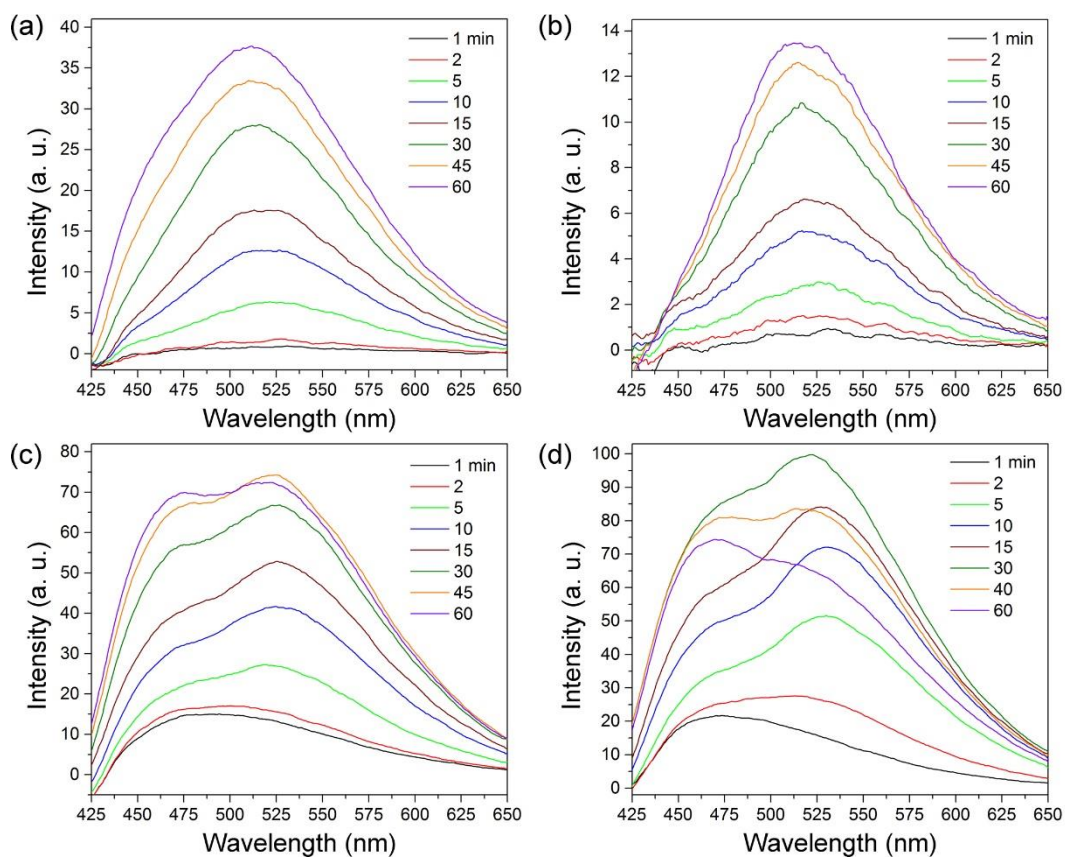
Figure 7.4: *In situ* fluorescence measurements of 100 μM DA solutions which were oxidized at different conditions. (a) 10 mM Tris (pH 9.6), (b) 0.5 mM NaOH (pH 9.6), (c) 10 mM NaOH and (d) 20 mM NaOH.
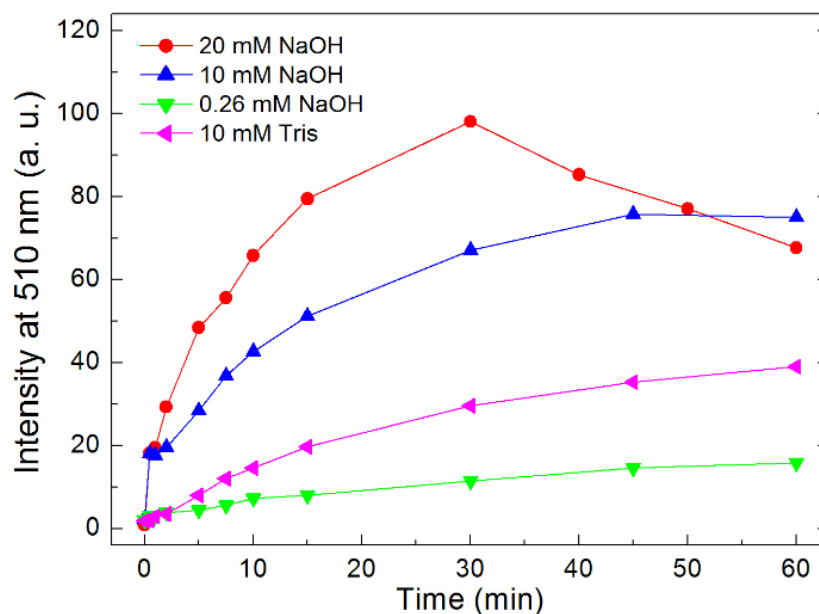
Figure 7.5: Time dependent fluorescence intensity at 510 nm of 100 µM DA solutions which were oxidized at different basic conditions.

The fluorescence spectra of synthesized PDA nanoparticles after 3 h of oxidization, which were prepared using 100 µM DA, is given in Figure 7.6a. We observed that fluorescence behavior of the resulting PDA nanoparticles is very similar with eumelanin polymers in which fluorescence spectrum is excitation wavelength dependent and can be tuned in the whole visible spectra [218]. With the increasing excitation wavelength, emission maximum of the PDA nanoparticle solution shifts to the longer wavelengths (Figure 7.6b). Also, emission intensity is excitation wavelength dependent; it initially enhances with increasing wavelengths and then started to decrease gradually. The maximum emission intensities were recorded between the excitation wavelengths of 350 and 400 nm. Therefore, we selected 370 nm as the excitation wavelength for DA sensing experiments.

Figure 7.6c shows the fluorescence spectra of 100 µM DA solution recorded at different time intervals up to 6 h. After NaOH addition, two emission peaks immediately formed at around 470 and 530 nm, respectively. In the first 30 min, intensities of the both peaks gradually increased. Interestingly, after 30 min the intensity of the peak around 530 nm started to decrease and it completely disappeared in 2 h. The peak intensity around 470 nm, on the other hand, decreased slightly

between 30 and 60 min but after this point it started to increase again. After 6 h, only an intense peak around 470 nm was observed. The peak around 530 nm may correspond to an intermediate product in the polymerization reaction, which is formed and consumed in 1 h. We believe that *in situ* fluorescence measurements of DA oxidation solution can give information about the structure of PDA -which is still not completely identified [221]- however; it is beyond the scope of this study. Figure 7.6d shows the emission intensity maxima of the same solution during polymerization. In the first minutes of polymerization the fluorescence intensity sharply increased and after about 30 min it started to decrease and after 90 min it began to raise again. Accordingly, we selected 30 min as incubation time for sensing experiments.
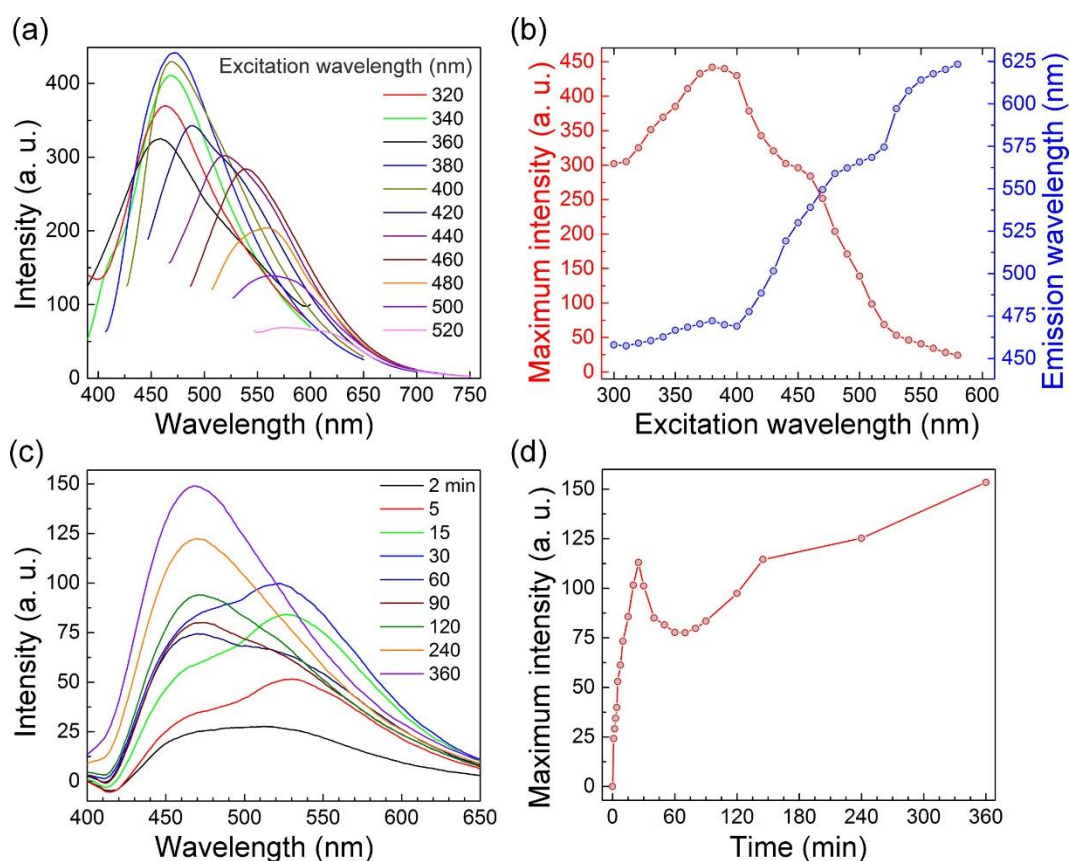
Figure 7.6: *In situ* fluorescence measurements of 100 µM DA solutions which were oxidized at different conditions. (a) 10 mM Tris (pH 9.6), (b) 0.5 mM NaOH (pH 9.6), (c) 10 mM NaOH and (d) 20 mM NaOH.

7.3 Controlling the Polymerization of Polydopamine Nanoparticles

Time dependent fluorescence spectrum of DA oxidization solution can be a source of error in the analytical measurements. To overcome this problem and obtain stable emission characteristic over time, we added excess HCl to DA solutions after a certain time of oxidization and stop the polymerization reaction by making the solution acidic. Figure 7.7a shows the fluorescence spectra of a DA oxidation solution (100 μM) before and after HCl addition. In the first 15 min, emission intensity increases gradually as expected. After HCl addition the fluorescence spectrum of the solution shifted to shorter wavelengths and becomes very stable over time. In Figure 7.7b, the emission intensity at 510 nm was plotted as a function of time. After HCl addition intensity at 510 nm increased slightly and then it was almost constant for at least 45 min.
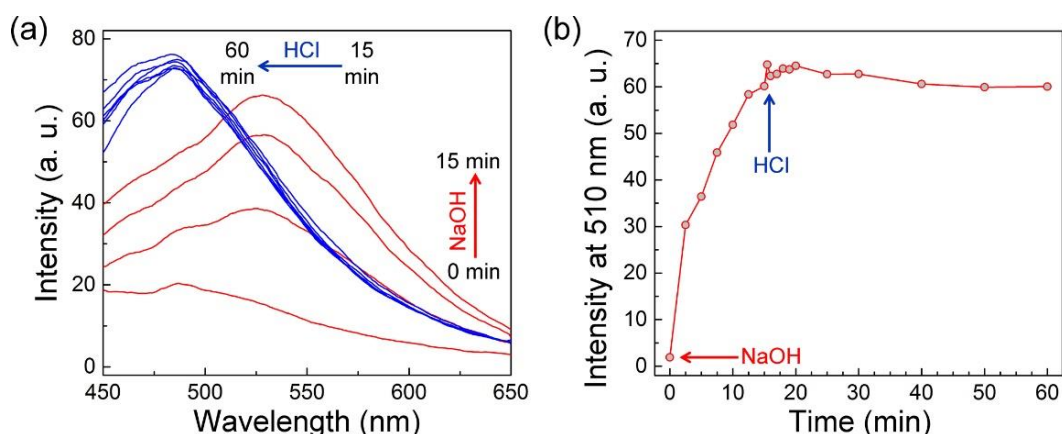
Figure 7.7: Stopping the polymerization reaction of DA using HCl. (a) Fluores-cence spectra of 100 μM DA, which is oxidized using 20 mM NaOH and after 15 min excess HCl was added. (b) Fluorescence intensity at 510 nm change with time before and after HCl addition.

7.4 Sensitive and Selective Dopamine Sensing

In order to evaluate the performance of the assay, we tested different concentrations of DA between 0.1 and 20 μM with the assay. First, oxidation of dopamine solutions at different concentrations in PBS was initiated using NaOH (20 mM) and after 30 min

excess HCl was added to stop the reaction. Then, fluorescence spectra of the DA solutions were recorded (Figure 7.8a). As expected with the increasing DA concentration, fluorescence of the solution becomes brighter. Figure 7.8b shows the fluorescence intensities at 510 nm as a function of DA concentration. We observed that the response of the assay is highly linear ($R^2 = 0.996$) in the studied concentration region. Relative standard deviations (RSD) of three separate experiments in Figure 7.8b are between 0.2% and 2.4% indicating the good reproducibility of the sensor response. Using this calibration line, we calculated limit of detection (LOD) and limit of qualification (LOQ) values of the assay as 40 nM and 120 nM, respectively. The achieved LOD and LOQ values of our fluorescence based assay is much better than absorption based methods (see Table 7.1) which typically have LOD and LOQ values above µM level. In addition, to directly compare the performance of our fluorescence assay with the absorption based method, we measured the absorption of DA solutions which were oxidized using the same conditions with fluorescence experiments. We observed that for the concentrations above 1 µM there is a statistically significant difference in the absorption value between blank and DA solutions (Figure 7.9). For the concentrations below 1 µM the absorption assay could not detect the presence of DA, which is also in accordance with the previous reports [208-212].
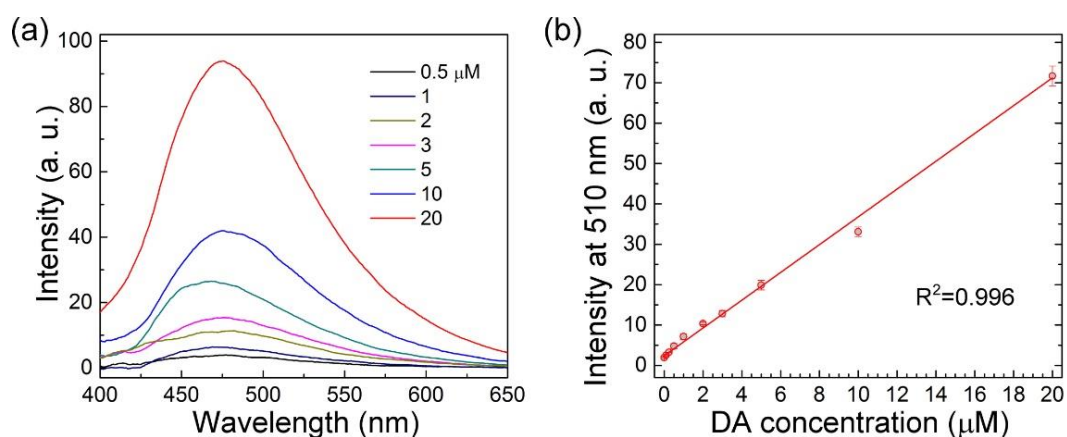
Figure 7.8: Sensitivity of the dopamine assay. (a) Fluorescence response of the assay against different concentrations of DA. (b) Assay response as a function of DA concentration which indicates the good linearity of the sensor in the studied region.

Method	Reagents	LOD (µM)	LOQ (µM)	Reference
Absorption	NaOH	0.76	2.5	1
Absorption	NaOH	7.5	-	2
Absorption	NaOH	-	3.5	3
Absorption	Enzyme	30	-	4
Absorption	Potassium ferricyanide	2.6	-	5
Fluorescence	NaOH and HCl	0.04	0.12	This study

Table 7.1: Comparison of sensitivity of the current assay with the previous dopamine oxidation based assays.
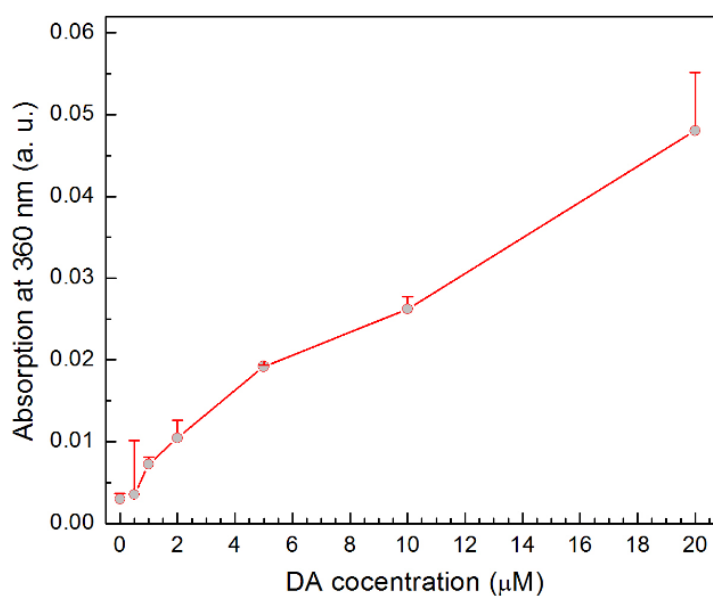
Figure 7.9: Absorption of DA oxidization solutions at 360 nm with respect to DA concentration.

Lastly, we tested the selectivity of the assay using possible interfering chemicals such as AA, UA, amino acids and sugars. The concentration of interfering substances is 100 µM. None of the tested chemicals produced fluorescence signal even at this high concentration (Figure 7.10). To further demonstrate the selectivity of the method, we measured the fluorescence of 10 µM DA oxidization solution in the presence of mixture of all of interfering chemicals that used in this study (concentration of interfering chemicals was 100 µM). Presence of these chemicals in the DA assay has

no effect on the fluorescence response (Figure 7.10). The observed excellent selectivity over DA of our assay is due to its specific response against PDA nanoparticle formation.
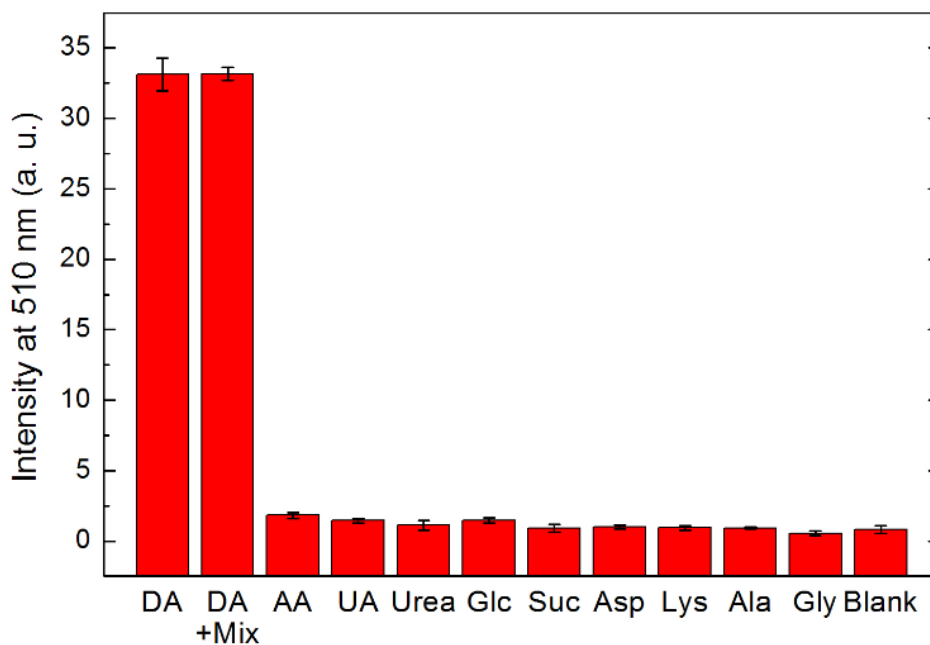
Figure 7.10: Selectivity of the dopamine assay. DA concentration is 10 μM and concentration of other substances is 100 μM. (DA: Dopamine, AA: Ascorbic acid, UA: Uric acid, Glc: Glucose, Suc: Sucrose, Asp: Aspartic acid, Lys: Lysine, Ala: Alanine, Gly: Glycine, Mix: mixture of all interfering chemicals)

Chapter 8

Conclusions

This thesis describes the design and synthesis of nanostructured materials for bioimaging and chemical sensing applications. We mainly focused on the synthesis and interface engineering of fluorescent MSNs to improve their emission intensity, dispersibility in biological environments and their compatibility with different cell lines. In addition we demonstrated their applications in cell labeling, chemotherapy, photodynamic therapy and explosive sensing. Besides from silica based nanomaterials, in this thesis we also work on the synthesis of polydopamine nanoparticles and showed that as-prepared polydopamine nanoparticle are fluorescent, to our knowledge for the first time. Furthermore, we demonstrated that fluorescence of polydopamine nanoparticles can be used for the turn-on sensing of dopamine neurotransmitter.

Surface chemistry of nanoparticles is the predominant factor that determines their solubility and colloidal stability in aqueous media, interactions with the cell membrane and their cellular uptake, preliminary interactions with analyte molecules and toxicity to the biological organisms. Therefore, proper interface engineering prior to their administration is needed for both effective biological and chemical sensing applications. In this context, we developed a facile self-assembly method to functionalize the surface of fluorescent MSNs with PEG polymer or peptide amphiphiles. PEGylated MSNs demonstrated excellent stability in highly salted aqueous media (PBS) and good cyto-compatibility with different cell lines. Sustained drug release from polymer capped MSNs was also demonstrated using an anticancer drug. In addition, fluorescent nanoparticles can be simply prepared by loading

fluorescent molecules into the pores of MSNs and then capping them with PEG polymer using the self-assembly approach. Peptide modified fluorescent MSNs, on the other hand, showed remarkable increase cellular uptake with good cyto-compatibility which make them excellent candidates for cell-labeling applications.

Surfactant assisted loading of fluorescent molecules inside the pores of MSNs during their synthesis was proved to be an effective and simple way to prepare ultrabright fluorescent hybrid nanoparticles. Using this method wide range of hydrophobic and hydrophilic molecules can be encapsulated to the pores of MSNs without the need of any covalent conjugation step. The major drawback of this method in biological applications is the extreme cytotoxicity of surfactant molecules which leaks from pores of the particles. To suppress the leakage of surfactant molecules and accordingly reduce their cytotoxicity, we capped the ultrabright MSNs with a dense silica layer. The resulting core/shell particles showed improved cyto-compatibility with several cell lines which make them more suitable for bioimaging application than uncapped particles. Furthermore, we demonstrated that core/shell ultrabright nanoparticles are suitable for synergetic chemo- and photodynamic- therapy of cancer. In another application of surfactant assisted encapsulation method, we prepared pyrene confined MSNs with bright, visible and stable pyrene excimer emission and utilized them for trace explosive sensing in aqueous media.

Hollow luminescent nanoparticles may be promising for simultaneous diagnosis and drug delivery applications due to their intrinsic luminescence and high pore volume. In the context of this thesis, we proposed a simple method to prepare hollow mesoporous silica nanoparticles with intrinsic luminescence. The method is based on selective dissolution of porous cores of solid silica shell/porous silica core nanoparticles in mild conditions (PBS or water). Shells of resulting luminescent hollow particles contains both small and large mesopores which makes the particles very suitable for adsorption and desorption of wide range of molecules such as drugs, proteins and DNA. In addition, we proposed a mechanism for selective dissolution of porous cores of the core/shell nanoparticles.

Although numerous mesoporous and/or hollow silica nanoparticle drug carriers and theranostic agents with various surface functionalities have been designed in the last decade, their biocompatibility remains a matter of intensive debate. Therefore, we

systematically evaluated interactions of a series of MSNs possessing different surface functional groups (ionic, polar, neutral, and hydrophobic) with blood constituents, in terms of their hemolytic activity, thrombogenicity, and adsorption of blood proteins on their surfaces. Demonstration of the surface functionalization having crucial impact on blood compatibility might serve as a guideline for further investigations related to design of mesoporous silica systems for biomedical applications, and shed light on research towards the ultimate goal of developing smart theranostic systems.

Lastly, we developed a facile assay for chemical sensing of dopamine, which is based on measuring the fluorescence signal of the oxidation product of the dopamine (polydopamine nanoparticles). Under optimized experimental conditions, we achieved a dopamine detection limit of as low as 40 nM with excellent selectivity. Compared with other DA detection methods, our assay is extremely simple and low cost, which make the method very promising for detection of DA deficiency related diseases.

In summary, the outcomes of the present work may provide useful information for design of new generation multifunctional fluorescent nanoparticles with good biocompatibility. Further, *in vivo* studies is necessary before their real-life applications. In addition, we believe that dopamine sensing experiments in real-samples may be an important follow up work of this thesis in terms of commercialization of the demonstrated fluorescent dopamine assay.

Bibliography

[1]   T. L. Doane, and C. Burda, "The unique role of nanoparticles in nanomedicine: imaging, drug delivery and therapy," *Chem. Soc. Rev.,* vol. 41, no. 7, pp. 2885-2911, 2012.

[2]   K. M. Wang, X. X. He, X. H. Yang, and H. Shi, "Functionalized Silica Nanoparticles: A Platform for Fluorescence Imaging at the Cell and Small Animal Levels," *Acc. Chem. Res.,* vol. 46, no. 7, pp. 1367-1376, 2013.

[3]   Q. Liu, Q. F. Zhou, and G. B. Jiang, "Nanomaterials for analysis and monitoring of emerging chemical pollutants," *Trac-Trend. Anal. Chem.,* vol. 58, pp. 10-22, 2014.

[4]   B. Fadeel, and A. E. Garcia-Bennett, "Better safe than sorry: Understanding the toxicological properties of inorganic nanoparticles manufactured for biomedical applications," *Adv. Drug Delivery Rev.,* vol. 62, no. 3, pp. 362-374, 2010.

[5]   B. Korzeniowska, R. Nooney, D. Wencel, and C. McDonagh, "Silica nanoparticles for cell imaging and intracellular sensing," *Nanotechnology,* vol. 24, no. 44, pp. 20, 2013.

[6]   P. Wu, and X. P. Yan, "Doped quantum dots for chemo/biosensing and bioimaging," *Chem. Soc. Rev.,* vol. 42, no. 12, pp. 5489-5521, 2013.

[7]   L. Shang, S. J. Dong, and G. U. Nienhaus, "Ultra-small fluorescent metal nanoclusters: Synthesis and biological applications," *Nano Today,* vol. 6, no. 4, pp. 401-418, 2011.

[8]   C. F. Wu, and D. T. Chiu, "Highly Fluorescent Semiconducting Polymer Dots for Biology and Medicine," *Angew. Chem. Int. Ed.,* vol. 52, no. 11, pp. 3086-3109, 2013.

[9] J. M. Rosenholm, C. Sahlgren, and M. Linden, "Towards multifunctional, targeted drug delivery systems using mesoporous silica nanoparticles - opportunities & challenges," *Nanoscale,* vol. 2, no. 10, pp. 1870-1883, 2010.

[10] J. Kim, Y. Piao, and T. Hyeon, "Multifunctional nanostructured materials for multimodal imaging, and simultaneous imaging and therapy," *Chem. Soc. Rev.,* vol. 38, no. 2, pp. 372-390, 2009.

[11] K. T. Yong, I. Roy, M. T. Swihart, and P. N. Prasad, "Multifunctional nanoparticles as biocompatible targeted probes for human cancer diagnosis and therapy," *J. Mater. Chem.,* vol. 19, no. 27, pp. 4655-4672, 2009.

[12] S. H. Wu, Y. Hung, and C. Y. Mou, "Mesoporous silica nanoparticles as nanocarriers," *Chem. Commun.,* vol. 47, no. 36, pp. 9972-9985, 2011.

[13] J. E. Lee, N. Lee, T. Kim, J. Kim, and T. Hyeon, "Multifunctional Mesoporous Silica Nanocomposite Nanoparticles for Theranostic Applications," *Acc. Chem. Res.,* vol. 44, no. 10, pp. 893-902, 2011.

[14] K. Yamashita, Y. Yoshioka, K. Higashisaka, K. Mimura, Y. Morishita, M. Nozaki, T. Yoshida, T. Ogura, H. Nabeshi, K. Nagano, Y. Abe, H. Kamada, Y. Monobe, T. Imazawa, H. Aoshima, K. Shishido, Y. Kawai, T. Mayumi, S. Tsunoda, N. Itoh, T. Yoshikawa, I. Yanagihara, S. Saito, and Y. Tsutsumi, "Silica and titanium dioxide nanoparticles cause pregnancy complications in mice," *Nat. Nanotech.,* vol. 6, no. 5, pp. 321-328, 2011.

[15] S. Sharifi, S. Behzadi, S. Laurent, M. L. Forrest, P. Stroeve, and M. Mahmoudi, "Toxicity of nanomaterials," *Chem. Soc. Rev.,* vol. 41, no. 6, pp. 2323-2343, 2012.

[16] Q. J. He, Z. W. Zhang, Y. Gao, J. L. Shi, and Y. P. Li, "Intracellular Localization and Cytotoxicity of Spherical Mesoporous Silica Nano- and Microparticles," *Small,* vol. 5, no. 23, pp. 2722-2729, 2009.

[17] Y. S. Lin, and C. L. Haynes, "Impacts of Mesoporous Silica Nanoparticle Size, Pore Ordering, and Pore Integrity on Hemolytic Activity," *J. Am. Chem. Soc.,* vol. 132, no. 13, pp. 4834-4842, 2010.

[18] T. Yu, K. Greish, L. D. McGill, A. Ray, and H. Ghandehari, "Influence of Geometry, Porosity, and Surface Characteristics of Silica Nanoparticles on

Acute Toxicity: Their Vasculature Effect and Tolerance Threshold," *ACS Nano,* vol. 6, no. 3, pp. 2289-2301, 2012.

[19] D. Tarn, C. E. Ashley, M. Xue, E. C. Carnes, J. I. Zink, and C. J. Brinker, "Mesoporous Silica Nanoparticle Nanocarriers: Biofunctionality and Biocompatibility," *Acc. Chem. Res.,* vol. 46, no. 3, pp. 792-801, 2013.

[20] Z. M. Tao, M. P. Morrow, T. Asefa, K. K. Sharma, C. Duncan, A. Anan, H. S. Penefsky, J. Goodisman, and A. K. Souid, "Mesoporous silica nanoparticles inhibit cellular respiration," *Nano Lett.,* vol. 8, no. 5, pp. 1517-1526, 2008.

[21] S. T. Yang, Y. Liu, Y. W. Wang, and A. N. Cao, "Biosafety and Bioapplication of Nanomaterials by Designing ProteinNanoparticle Interactions," *Small,* vol. 9, no. 9-10, pp. 1635-1653, 2013.

[22] S. P. Hudson, R. F. Padera, R. Langer, and D. S. Kohane, "The biocompatibility of mesoporous silicates," *Biomaterials,* vol. 29, no. 30, pp. 4045-4055, 2008.

[23] Y. Teow, P. V. Asharani, M. P. Hande, and S. Valiyaveettil, "Health impact and safety of engineered nanomaterials," *Chem. Commun.,* vol. 47, no. 25, pp. 7025-7038, 2011.

[24] Q. J. He, J. M. Zhang, J. L. Shi, Z. Y. Zhu, L. X. Zhang, W. B. Bu, L. M. Guo, and Y. Chen, "The effect of PEGylation of mesoporous silica nanoparticles on nonspecific binding of serum proteins and cellular responses," *Biomaterials,* vol. 31, no. 6, pp. 1085-1092, 2010.

[25] H. Meng, M. Xue, T. Xia, Z. X. Ji, D. Y. Tarn, J. I. Zink, and A. E. Nel, "Use of Size and a Copolymer Design Feature To Improve the Biodistribution and the Enhanced Permeability and Retention Effect of Doxorubicin-Loaded Mesoporous Silica Nanoparticles in a Murine Xenograft Tumor Model," *ACS Nano,* vol. 5, no. 5, pp. 4131-4144, 2011.

[26] J. T. Sun, Z. Q. Yu, C. Y. Hong, and C. Y. Pan, "Biocompatible Zwitterionic Sulfobetaine Copolymer-Coated Mesoporous Silica Nanoparticles for Temperature-Responsive Drug Release," *Macromol. Rapid Comm.,* vol. 33, no. 9, pp. 811-818, 2012.

[27] H. X. Wu, G. Liu, S. J. Zhang, J. L. Shi, L. X. Zhang, Y. Chen, F. Chen, and H. R. Chen, "Biocompatibility, MR imaging and targeted drug delivery of a rattle-type magnetic mesoporous silica nanosphere system conjugated with PEG and

cancer-cell-specific ligands," *J. Mater. Chem.,* vol. 21, no. 9, pp. 3037-3045, 2011.

[28] C. P. Tsai, C. Y. Chen, Y. Hung, F. H. Chang, and C. Y. Mou, "Monoclonal antibody-functionalized mesoporous silica nanoparticles (MSN) for selective targeting breast cancer cells," *J. Mater. Chem.,* vol. 19, no. 32, pp. 5737-5743, 2009.

[29] L. Z. He, Y. Y. Huang, H. L. Zhu, G. H. Pang, W. J. Zheng, Y. S. Wong, and T. F. Chen, "Cancer-Targeted Monodisperse Mesoporous Silica Nanoparticles as Carrier of Ruthenium Polypyridyl Complexes to Enhance Theranostic Effects," *Adv. Funct. Mater.,* vol. 24, no. 19, pp. 2754-2763, 2014.

[30] S. Sulek, B. Mammadov, D. I. Mahcicek, H. Sozeri, E. Atalar, A. B. Tekinay, and M. O. Guler, "Peptide functionalized superparamagnetic iron oxide nanoparticles as MRI contrast agents," *J. Mater. Chem.,* vol. 21, no. 39, pp. 15157-15162, 2011.

[31] R. M. Levine, C. M. Scott, and E. Kokkoli, "Peptide functionalized nanoparticles for nonviral gene delivery," *Soft Matter,* vol. 9, no. 4, pp. 985-1004, 2013.

[32] D. P. Ferris, J. Lu, C. Gothard, R. Yanes, C. R. Thomas, J. C. Olsen, J. F. Stoddart, F. Tamanoi, and J. I. Zink, "Synthesis of Biomolecule-Modified Mesoporous Silica Nanoparticles for Targeted Hydrophobic Drug Delivery to Cancer Cells," *Small,* vol. 7, no. 13, pp. 1816-1826, 2011.

[33] K. Epler, D. Padilla, G. Phillips, P. Crowder, R. Castillo, D. Wilkinson, B. Wilkinson, C. Burgard, R. Kalinich, J. Townson, B. Chackerian, C. Willman, D. Peabody, W. Wharton, C. J. Brinker, C. Ashley, and E. Carnes, "Delivery of Ricin Toxin A-Chain by Peptide-Targeted Mesoporous Silica Nanoparticle-Supported Lipid Bilayers," *Adv. Healthcare Mater.,* vol. 1, no. 3, pp. 348-353, 2012.

[34] S. H. Cheng, C. H. Lee, M. C. Chen, J. S. Souris, F. G. Tseng, C. S. Yang, C. Y. Mou, C. T. Chen, and L. W. Lo, "Tri-functionalization of mesoporous silica nanoparticles for comprehensive cancer theranostics-the trio of imaging, targeting and therapy," *J. Mater. Chem.,* vol. 20, no. 29, pp. 6149-6157, 2010.

[35] Y. Wang, W. Shi, W. S. Song, L. Wang, X. G. Liu, J. Chen, and R. Q. Huang, "Tumor cell targeted delivery by specific peptide-modified mesoporous silica nanoparticles," *J. Mater. Chem.,* vol. 22, no. 29, pp. 14608-14616, 2012.

[36] L. M. Pan, Q. J. He, J. N. Liu, Y. Chen, M. Ma, L. L. Zhang, and J. L. Shi, "Nuclear-Targeted Drug Delivery of TAT Peptide-Conjugated Monodisperse Mesoporous Silica Nanoparticles," *J. Am. Chem. Soc.,* vol. 134, no. 13, pp. 5722-5725, 2012.

[37] X. Li, Y. J. Chen, M. Q. Wang, Y. J. Ma, W. L. Xia, and H. C. Gu, "A mesoporous silica nanoparticle - PEI - Fusogenic peptide system for siRNA delivery in cancer therapy," *Biomaterials,* vol. 34, no. 4, pp. 1391-1401, 2013.

[38] I. L. Medintz, T. Pons, J. B. Delehanty, K. Susumu, F. M. Brunel, P. E. Dawson, and H. Mattoussi, "Intracellular delivery of quantum dot-protein cargos mediated by cell penetrating peptides," *Bioconjugate Chem.,* vol. 19, no. 9, pp. 1785-1795, 2008.

[39] C. Coll, L. Mondragon, R. Martinez-Manez, F. Sancenon, M. D. Marcos, J. Soto, P. Amoros, and E. Perez-Paya, "Enzyme-Mediated Controlled Release Systems by Anchoring Peptide Sequences on Mesoporous Silica Supports," *Angew. Chem. Int. Ed.,* vol. 50, no. 9, pp. 2138-2140, 2011.

[40] M. Oishi, A. Tamura, T. Nakamura, and Y. Nagasaki, "A Smart Nanoprobe Based On Fluorescence-Quenching PEGylated Nanogels Containing Gold Nanoparticles for Monitoring the Response to Cancer Therapy," *Adv. Funct. Mater.,* vol. 19, no. 6, pp. 827-834, 2009.

[41] D. W. Deng, D. Y. Zhang, Y. Li, S. Achilefu, and Y. Q. Gu, "Gold nanoparticles based molecular beacons for in vitro and in vivo detection of the matriptase expression on tumor," *Biosens. Bioelectron.,* vol. 49, pp. 216-221, 2013.

[42] I. M. Rio-Echevarria, F. Selvestrel, D. Segat, G. Guarino, R. Tavano, V. Causin, E. Reddi, E. Papini, and F. Mancin, "Highly PEGylated silica nanoparticles: "ready to use" stealth functional nanocarriers," *J. Mater. Chem.,* vol. 20, no. 14, pp. 2780-2787, 2010.

[43] Z. N. Wu, C. R. Guo, S. Liang, H. Zhang, L. P. Wang, H. C. Sun, and B. Yang, "A pluronic F127 coating strategy to produce stable up-conversion

NaYF$_4$:Yb,Er(Tm) nanoparticles in culture media for bioimaging," *J. Mater. Chem.,* vol. 22, no. 35, pp. 18596-18602, 2012.

[44] B. Baudin, A. Bruneel, N. Bosselut, and M. Vaubourdolle, "A protocol for isolation and culture of human umbilical vein endothelial cells," *Nat. Protoc.,* vol. 2, no. 3, pp. 481-485, 2007.

[45] V. Cauda, A. Schlossbauer, J. Kecht, A. Zurner, and T. Bein, "Multiple Core-Shell Functionalized Colloidal Mesoporous Silica Nanoparticles," *J. Am. Chem. Soc.,* vol. 131, no. 32, pp. 11361-11370, 2009.

[46] A. Yildirim, H. Budunoglu, B. Daglar, H. Deniz, and M. Bayindir, "One-Pot Preparation of Fluorinated Mesoporous Silica Nanoparticles for Liquid Marble Formation and Superhydrophobic Surfaces," *ACS Appl. Mater. Interfaces,* vol. 3, no. 6, pp. 1804-1808, 2011.

[47] S. Febvay, D. M. Marini, A. M. Belcher, and D. E. Clapham, "Targeted Cytosolic Delivery of Cell-Impermeable Compounds by Nanoparticle-Mediated, Light-Triggered Endosome Disruption," *Nano Lett.,* vol. 10, no. 6, pp. 2211-2219, 2010.

[48] L. T. Zhuravlev, "Concentration of Hydroxyl-Groups on the Surface of Amorphous Silicas," *Langmuir,* vol. 3, no. 3, pp. 316-318, 1987.

[49] L. S. Wang, L. C. Wu, S. Y. Lu, L. L. Chang, I. T. Teng, C. M. Yang, and J. A. A. Ho, "Biofunctionalized Phospholipid-Capped Mesoporous Silica Nanoshuttles for Targeted Drug Delivery: Improved Water Suspensibility and Decreased Nonspecific Protein Binding," *ACS Nano,* vol. 4, no. 8, pp. 4371-4379, 2010.

[50] A. Yildirim, E. Ozgur, and M. Bayindir, "Impact of mesoporous silica nanoparticle surface functionality on hemolytic activity, thrombogenicity and non-specific protein adsorption," *J. Mater. Chem. B,* vol. 1, no. 14, pp. 1909-1920, 2013.

[51] Q. J. He, J. M. Zhang, F. Chen, L. M. Guo, Z. Y. Zhu, and J. L. Shi, "An anti-ROS/hepatic fibrosis drug delivery system based on salvianolic acid B loaded mesoporous silica nanoparticles," *Biomaterials,* vol. 31, no. 30, pp. 7785-7796, 2010.

[52] Y. Gao, Y. Chen, X. F. Ji, X. Y. He, Q. Yin, Z. W. Zhang, J. L. Shi, and Y. P. Li, "Controlled Intracellular Release of Doxorubicin in Multidrug-Resistant Cancer Cells by Tuning the Shell-Pore Sizes of Mesoporous Silica Nanoparticles," *ACS Nano,* vol. 5, no. 12, pp. 9788-9798, 2011.

[53] A. Yildirim, G. B. Demirel, R. Erdem, B. Senturk, T. Tekinay, and M. Bayindir, "Pluronic polymer capped biocompatible mesoporous silica nanocarriers," *Chem. Commun.,* vol. 49, no. 84, pp. 9782-9784, 2013.

[54] M. Liong, J. Lu, M. Kovochich, T. Xia, S. G. Ruehm, A. E. Nel, F. Tamanoi, and J. I. Zink, "Multifunctional inorganic nanoparticles for imaging, targeting, and drug delivery," *ACS Nano,* vol. 2, no. 5, pp. 889-896, 2008.

[55] M. Kar, P. S. Vijayakumar, B. L. V. Prasad, and S. Sen Gupta, "Synthesis and Characterization of Poly-L-lysine-Grafted Silica Nanoparticles Synthesized via NCA Polymerization and Click Chemistry," *Langmuir,* vol. 26, no. 8, pp. 5772-5781, 2010.

[56] D. Kim, S. Finkenstaedt-Quinn, K. R. Hurley, J. T. Buchman, and C. L. Haynes, "On-chip evaluation of platelet adhesion and aggregation upon exposure to mesoporous silica nanoparticles," *Analyst,* vol. 139, no. 5, pp. 906-913, 2014.

[57] L. A. Chen, J. M. McCrate, J. C. M. Lee, and H. Li, "The role of surface charge on the uptake and biocompatibility of hydroxyapatite nanoparticles with osteoblast cells," *Nanotechnology,* vol. 22, no. 10, pp. 10, 2011.

[58] E. B. Cho, D. O. Volkov, and I. Sokolov, "Ultrabright Fluorescent Mesoporous Silica Nanoparticles," *Small,* vol. 6, no. 20, pp. 2314-2319, 2010.

[59] E. B. Cho, D. O. Volkov, and I. Sokolov, "Ultrabright Fluorescent Silica Mesoporous Silica Nanoparticles: Control of Particle Size and Dye Loading," *Adv. Funct. Mater.,* vol. 21, no. 16, pp. 3129-3135, 2011.

[60] S. Palantavida, N. V. Guz, and I. Sokolov, "Functionalized Ultrabright Fluorescent Mesoporous Silica Nanoparticles," *Part. Part. Syst. Char.,* vol. 30, no. 9, pp. 804-811, 2013.

[61] S. Palantavida, N. V. Guz, C. D. Woodworth, and I. Sokolov, "Ultrabright fluorescent mesoporous silica nanoparticles for prescreening of cervical cancer," *Nanomedicine,* vol. 9, no. 8, pp. 1255-1262, 2013.

[62] I. Sokolov, Y. Y. Kievsky, and J. M. Kaszpurenko, "Self-assembly of ultrabright fluorescent silica particles," *Small,* vol. 3, no. 3, pp. 419-423, 2007.

[63] I. Sokolov, and S. Naik, "Novel fluorescent silica nanoparticles: Towards ultrabright silica nanoparticles," *Small,* vol. 4, no. 7, pp. 934-939, 2008.

[64] L. Tao, C. J. Song, Y. J. Sun, X. H. Li, Y. Y. Li, B. Q. Jin, Z. J. Zhang, and K. Yang, "A fluorescent and chemiluminescent difunctional mesoporous silica nanoparticle as a label for the ultrasensitive detection of cancer cells," *Anal. Chim. Acta,* vol. 761, pp. 194-200, 2013.

[65] C. H. Tsai, J. L. Vivero-Escoto, Slowing, II, I. J. Fang, B. G. Trewyn, and V. S. Y. Lin, "Surfactant-assisted controlled release of hydrophobic drugs using anionic surfactant templated mesoporous silica nanoparticles," *Biomaterials,* vol. 32, no. 26, pp. 6234-6244, 2011.

[66] Q. J. He, J. L. Shi, F. Chen, M. Zhu, and L. X. Zhang, "An anticancer drug delivery system based on surfactant-templated mesoporous silica nanoparticles," *Biomaterials,* vol. 31, no. 12, pp. 3335-3346, 2010.

[67] N. Vlachy, D. Touraud, J. Heilmann, and W. Kunz, "Determining the cytotoxicity of catanionic surfactant mixtures on HeLa cells," *Colloid. Surface. B,* vol. 70, no. 2, pp. 278-280, 2009.

[68] B. K. Wang, J. H. Wang, Q. Liu, H. Huang, M. Chen, K. Y. Li, C. Z. Li, X. F. Yu, and P. K. Chu, "Rose-bengal-conjugated gold nanorods for in vivo photodynamic and photothermal oral cancer therapies," *Biomaterials,* vol. 35, no. 6, pp. 1954-1966, 2014.

[69] J. Hawari, S. Beaudet, A. Halasz, S. Thiboutot, and G. Ampleman, "Microbial degradation of explosives: biotransformation versus mineralization," *Appl. Microbiol. Biot.,* vol. 54, no. 5, pp. 605-618, 2000.

[70] N. Hannink, S. J. Rosser, C. E. French, A. Basran, J. A. H. Murray, S. Nicklin, and N. C. Bruce, "Phytodetoxification of TNT by transgenic plants expressing a bacterial nitroreductase," *Nat. Biotechnol.,* vol. 19, no. 12, pp. 1168-1172, 2001.

[71] M. E. Germain, and M. J. Knapp, "Optical explosives detection: from color changes to fluorescence turn-on," *Chem. Soc. Rev.,* vol. 38, no. 9, pp. 2543-2555, 2009.

[72] Y. Salinas, R. Martinez-Manez, M. D. Marcos, F. Sancenon, A. M. Costero, M. Parra, and S. Gil, "Optical chemosensors and reagents to detect explosives," *Chem. Soc. Rev.,* vol. 41, no. 3, pp. 1261-1296, 2012.

[73] S. Singh, "Sensors - An effective approach for the detection of explosives," *J. Hazard. Mater.,* vol. 144, no. 1-2, pp. 15-28, 2007.

[74] J. S. Caygill, F. Davis, and S. P. J. Higson, "Current trends in explosive detection techniques," *Talanta,* vol. 88, pp. 14-29, 2012.

[75] D. S. Moore, "Instrumentation for trace detection of high explosives," *Rev. Sci. Instrum.,* vol. 75, no. 8, pp. 2499-2512, 2004.

[76] S. J. Toal, and W. C. Trogler, "Polymer sensors for nitroaromatic explosives detection," *J. Mater. Chem.,* vol. 16, no. 28, pp. 2871-2883, 2006.

[77] K. Zhang, H. B. Zhou, Q. S. Mei, S. H. Wang, G. J. Guan, R. Y. Liu, J. Zhang, and Z. P. Zhang, "Instant Visual Detection of Trinitrotoluene Particulates on Various Surfaces by Ratiometric Fluorescence of Dual-Emission Quantum Dots Hybrid," *J. Am. Chem. Soc.,* vol. 133, no. 22, pp. 8424-8427, 2011.

[78] R. Freeman, T. Finder, L. Bahshi, R. Gill, and I. Willner, "Functionalized CdSe/ZnS QDs for the Detection of Nitroaromatic or RDX Explosives," *Adv. Mater.,* vol. 24, no. 48, pp. 6416-6421, 2012.

[79] S. F. Xu, H. Z. Lu, J. H. Li, X. L. Song, A. X. Wang, L. X. Chen, and S. B. Han, "Dummy Molecularly Imprinted Polymers-Capped CdTe Quantum Dots for the Fluorescent Sensing of 2,4,6-Trinitrotoluene," *ACS Appl. Mater. Interfaces,* vol. 5, no. 16, pp. 8146-8154, 2013.

[80] D. D. Li, J. Z. Liu, R. T. K. Kwok, Z. Q. Liang, B. Z. Tang, and J. H. Yu, "Supersensitive detection of explosives by recyclable AIE luminogen-functionalized mesoporous materials," *Chem. Commun.,* vol. 48, no. 57, pp. 7167-7169, 2012.

[81] A. Rana, and P. K. Panda, "Fluorescent turn-off based sensing of nitrated explosives using porphyrins and their Zn(II)-derivatives," *RSC Adv.,* vol. 2, no. 32, pp. 12164-12168, 2012.

[82] S. Shanmugaraju, S. A. Joshi, and P. S. Mukherjee, "Fluorescence and visual sensing of nitroaromatic explosives using electron rich discrete fluorophores," *J. Mater. Chem.,* vol. 21, no. 25, pp. 9130-9138, 2011.

[83] H. M. Li, Y. X. Zhu, J. Y. Zhang, Z. G. Chi, L. P. Chen, and C. Y. Su, "Luminescent metal-organic gels with tetraphenylethylene moieties: porosity and aggregation-induced emission," *RSC Adv.,* vol. 3, no. 37, pp. 16340-16344, 2013.

[84] B. Gole, A. K. Bar, and P. S. Mukherjee, "Fluorescent metal-organic framework for selective sensing of nitroaromatic explosives," *Chem. Commun.,* vol. 47, no. 44, pp. 12137-12139, 2011.

[85] Y. N. Gong, L. Jiang, and T. B. Lu, "A highly stable dynamic fluorescent metal-organic framework for selective sensing of nitroaromatic explosives," *Chem. Commun.,* vol. 49, no. 94, pp. 11113-11115, 2013.

[86] D. T. McQuade, A. E. Pullen, and T. M. Swager, "Conjugated polymer-based chemical sensors," *Chem. Rev.,* vol. 100, no. 7, pp. 2537-2574, 2000.

[87] A. Rose, Z. G. Zhu, C. F. Madigan, T. M. Swager, and V. Bulovic, "Sensitivity gains in chemosensing by lasing action in organic polymers," *Nature,* vol. 434, no. 7035, pp. 876-879, 2005.

[88] L. J. Feng, H. Li, Y. Qu, and C. L. Lu, "Detection of TNT based on conjugated polymer encapsulated in mesoporous silica nanoparticles through FRET," *Chem. Commun.,* vol. 48, no. 38, pp. 4633-4635, 2012.

[89] Y. Z. Liao, V. Strong, Y. Wang, X. G. Li, X. Wang, and R. B. Kaner, "Oligotriphenylene Nanofiber Sensors for Detection of Nitro-Based Explosives," *Adv. Funct. Mater.,* vol. 22, no. 4, pp. 726-735, 2012.

[90] T. M. Figueira-Duarte, and K. Mullen, "Pyrene-Based Materials for Organic Electronics," *Chem. Rev.,* vol. 111, no. 11, pp. 7260-7314, 2011.

[91] Y. Wang, A. La, Y. Ding, Y. X. Liu, and Y. Lei, "Novel Signal-Amplifying Fluorescent Nanofibers for Naked-Eye-Based Ultrasensitive Detection of Buried Explosives and Explosive Vapors," *Adv. Funct. Mater.,* vol. 22, no. 17, pp. 3547-3555, 2012.

[92] P. Beyazkilic, A. Yildirim, and M. Bayindir, "Formation of Pyrene Excimers in Mesoporous Ormosil Thin Films for Visual Detection of Nitro-explosives," *ACS Appl. Mater. Interfaces,* vol. 6, no. 7, pp. 4997-5004, 2014.

[93] G. B. Demirel, B. Daglar, and M. Bayindir, "Extremely fast and highly selective detection of nitroaromatic explosive vapours using fluorescent polymer thin films," *Chem. Commun.,* vol. 49, no. 55, pp. 6140-6142, 2013.

[94] H. Y. Du, G. He, T. H. Liu, L. P. Ding, and Y. Fang, "Preparation of pyrene-functionalized fluorescent film with a benzene ring in spacer and sensitive detection to picric acid in aqueous phase," *J. Photoch. Photobio. A,* vol. 217, no. 2-3, pp. 356-362, 2011.

[95] T. H. Liu, L. P. Ding, K. R. Zhao, W. L. Wang, and Y. Fang, "Single-layer assembly of pyrene end-capped terthiophene and its sensing performances to nitroaromatic explosives," *J. Mater. Chem.,* vol. 22, no. 3, pp. 1069-1077, 2012.

[96] G. He, N. Yan, J. Y. Yang, H. Y. Wang, L. P. Ding, S. W. Yin, and Y. Fang, "Pyrene-Containing Conjugated Polymer-Based Fluorescent Films for Highly Sensitive and Selective Sensing of TNT in Aqueous Medium," *Macromolecules,* vol. 44, no. 12, pp. 4759-4766, 2011.

[97] Y. Wang, A. La, C. Bruckner, and Y. Lei, "FRET- and PET-based sensing in a single material: expanding the dynamic range of an ultra-sensitive nitroaromatic explosives assay," *Chem. Commun.,* vol. 48, no. 79, pp. 9903-9905, 2012.

[98] A. Vu, J. Phillips, P. Buhlmann, and A. Stein, "Quenching Performance of Surfactant-Containing and Surfactant-Free Fluorophore-Doped Mesoporous Silica Films for Nitroaromatic Compound Detection," *Chem. Mater.,* vol. 25, no. 5, pp. 711-722, 2013.

[99] K. Sarkar, Y. Salinas, I. Campos, R. Martinez-Manez, M. D. Marcos, F. Sancenon, and P. Amoros, "Organic-Inorganic Hybrid Mesoporous Materials as Regenerable Sensing Systems for the Recognition of Nitroaromatic Explosives," *ChemPlusChem,* vol. 78, no. 7, pp. 684-694, 2013.

[100] W. Chen, N. B. Zuckerman, J. P. Konopelski, and S. W. Chen, "Pyrene-Functionalized Ruthenium Nanoparticles as Effective Chemosensors for Nitroaromatic Derivatives," *Anal. Chem.,* vol. 82, no. 2, pp. 461-465, 2010.

[101] Q. Cai, Z. S. Luo, W. Q. Pang, Y. W. Fan, X. H. Chen, and F. Z. Cui, "Dilute solution routes to various controllable morphologies of MCM-41 silica with a basic medium," *Chem. Mater.,* vol. 13, no. 2, pp. 258-263, Feb, 2001.

[102] K. Suzuki, K. Ikari, and H. Imai, "Synthesis of silica nanoparticles having a well-ordered mesostructure using a double surfactant system," *J. Am. Chem. Soc.,* vol. 126, no. 2, pp. 462-463, 2004.

[103] F. M. Winnik, "Photophysics of Preassociated Pyrenes in Aqueous Polymer-Solutions and in Other Organized Media," *Chem. Rev.,* vol. 93, no. 2, pp. 587-614, Mar-Apr, 1993.

[104] J. S. Yang, and T. M. Swager, "Fluorescent porous polymer films as TNT chemosensors: Electronic and structural effects," *J. Am. Chem. Soc.,* vol. 120, no. 46, pp. 11864-11873, 1998.

[105] J. Hu, M. Chen, X. S. Fang, and L. W. Wu, "Fabrication and application of inorganic hollow spheres," *Chem. Soc. Rev.,* vol. 40, no. 11, pp. 5472-5491, 2011.

[106] X. W. Lou, L. A. Archer, and Z. C. Yang, "Hollow Micro-/Nanostructures: Synthesis and Applications," *Adv. Mater.,* vol. 20, no. 21, pp. 3987-4019, 2008.

[107] J. Liu, F. Liu, K. Gao, J. S. Wu, and D. F. Xue, "Recent developments in the chemical synthesis of inorganic porous capsules," *J. Mater. Chem.,* vol. 19, no. 34, pp. 6073-6084, 2009.

[108] M. Chen, L. M. Wu, S. X. Zhou, and B. You, "A method for the fabrication of monodisperse hollow silica spheres," *Adv. Mater.,* vol. 18, no. 6, pp. 801-806, 2006.

[109] Y. Zhao, L. N. Lin, Y. Lu, S. F. Chen, L. A. Dong, and S. H. Yu, "Templating Synthesis of Preloaded Doxorubicin in Hollow Mesoporous Silica Nanospheres for Biomedical Applications," *Adv. Mater.,* vol. 22, no. 46, pp. 5255-5259, 2010.

[110] F. Caruso, R. A. Caruso, and H. Mohwald, "Nanoengineering of inorganic and hybrid hollow spheres by colloidal templating," *Science,* vol. 282, no. 5391, pp. 1111-1114, 1998.

[111] S. O. Obare, N. R. Jana, and C. J. Murphy, "Preparation of polystyrene- and silica-coated gold nanorods and their use as templates for the synthesis of hollow nanotubes," *Nano Lett.,* vol. 1, no. 11, pp. 601-603, 2001.

[112] Y. Yamada, M. Mizutani, T. Nakamura, and K. Yano, "Mesoporous Microcapsules with Decorated Inner Surface: Fabrication and Photocatalytic Activity," *Chem. Mater.,* vol. 22, no. 5, pp. 1695-1703, 2010.

[113] I. Tissot, J. P. Reymond, F. Lefebvre, and E. Bourgeat-Lami, "SiOH-functionalized polystyrene latexes. A step toward the synthesis of hollow silica nanoparticles," *Chem. Mater.,* vol. 14, no. 3, pp. 1325-1331, 2002.

[114] W. J. Zhang, C. Y. Hong, and C. Y. Pan, "Fabrication and characterization of silica nanotubes with controlled dimensions," *J. Mater. Chem. A,* vol. 2, no. 21, pp. 7819-7828, 2014.

[115] W. R. Zhao, M. D. Lang, Y. S. Li, L. Li, and J. L. Shi, "Fabrication of uniform hollow mesoporous silica spheres and ellipsoids of tunable size through a facile hard-templating route," *J. Mater. Chem.,* vol. 19, no. 18, pp. 2778-2783, 2009.

[116] J. G. Wang, Q. Xiao, H. J. Zhou, P. C. Sun, Z. Y. Yuan, B. H. Li, D. T. Ding, A. C. Shi, and T. H. Chen, "Budded, mesoporous silica hollow spheres: Hierarchical structure controlled by kinetic self-assembly," *Adv. Mater.,* vol. 18, no. 24, pp. 3284-3288, 2006.

[117] M. Mandal, and M. Kruk, "Family of Single-Micelle-Templated Organosilica Hollow Nanospheres and Nanotubes Synthesized through Adjustment of Organosilica/Surfactant Ratio," *Chem. Mater.,* vol. 24, no. 1, pp. 123-132, 2012.

[118] J. A. Li, J. Liu, D. H. Wang, R. S. Guo, X. L. Li, and W. Qi, "Interfacially Controlled Synthesis of Hollow Mesoporous Silica Spheres with Radially Oriented Pore Structures," *Langmuir,* vol. 26, no. 14, pp. 12267-12272, 2010.

[119] H. Djojoputro, X. F. Zhou, S. Z. Qiao, L. Z. Wang, C. Z. Yu, and G. Q. Lu, "Periodic mesoporous organosilica hollow spheres with tunable wall thickness," *J. Am. Chem. Soc.,* vol. 128, no. 19, pp. 6320-6321, 2006.

[120] K. A. Dahlberg, and J. W. Schwank, "Synthesis of Ni@SiO_2 Nanotube Particles in a Water-in-Oil Microemulsion Template," *Chem. Mater.,* vol. 24, no. 14, pp. 2635-2644, 2012.

[121] Y. J. Zhao, J. L. Zhang, W. Li, C. X. Zhang, and B. X. Han, "Synthesis of uniform hollow silica spheres with ordered mesoporous shells in a CO_2 induced nanoemulsion," *Chem. Commun.*, no. 17, pp. 2365-2367, 2009.

[122] Q. Sun, P. Magusin, B. Mezari, P. Panine, R. A. van Santen, and N. Sommerdijk, "The formation of gigantic hollow silica spheres from an EO(76)-PO(29)EO(76)/butanol/ethanol/H_2O quaternary system," *J. Mater. Chem.,* vol. 15, no. 2, pp. 256-259, 2005.

[123] S. H. Wu, Y. Hung, and C. Y. Mou, "Compartmentalized Hollow Silica Nanospheres Templated from Nanoemulsions," *Chem. Mater.,* vol. 25, no. 3, pp. 352-364, 2013.

[124] Q. Zhang, T. R. Zhang, J. P. Ge, and Y. D. Yin, "Permeable silica shell through surface-protected etching," *Nano Lett.,* vol. 8, no. 9, pp. 2867-2871, 2008.

[125] N. Ren, B. Wang, Y. H. Yang, Y. H. Zhang, W. L. Yang, Y. H. Yue, Z. Gao, and Y. Tang, "General method for the fabrication of hollow microcapsules with adjustable shell compositions," *Chem. Mater.,* vol. 17, no. 10, pp. 2582-2587, 2005.

[126] M. S. Islam, W. S. Choi, and H. J. Lee, "Controlled Etching of Internal and External Structures of SiO_2 Nanoparticles Using Hydrogen Bond of Polyelectrolytes," *ACS Appl. Mater. Interfaces,* vol. 6, no. 12, pp. 9563-9571, 2014.

[127] Y. Chen, H. R. Chen, L. M. Guo, Q. J. He, F. Chen, J. Zhou, J. W. Feng, and J. L. Shi, "Hollow/Rattle-Type Mesoporous Nanostructures by a Structural Difference-Based Selective Etching Strategy," *ACS Nano,* vol. 4, no. 1, pp. 529-539, 2010.

[128] X. L. Fang, C. Chen, Z. H. Liu, P. X. Liu, and N. F. Zheng, "A cationic surfactant assisted selective etching strategy to hollow mesoporous silica spheres," *Nanoscale,* vol. 3, no. 4, pp. 1632-1639, 2011.

[129] D. Chen, L. L. Li, F. Q. Tang, and S. O. Qi, "Facile and Scalable Synthesis of Tailored Silica "Nanorattle" Structures," *Adv. Mater.,* vol. 21, no. 37, pp. 3804-3807, 2009.

[130] Y. Chen, C. Chu, Y. C. Zhou, Y. F. Ru, H. R. Chen, F. Chen, Q. J. He, Y. L. Zhang, L. L. Zhang, and J. L. Shi, "Reversible Pore-Structure Evolution in Hollow Silica Nanocapsules: Large Pores for siRNA Delivery and Nanoparticle Collecting," *Small,* vol. 7, no. 20, pp. 2935-2944, 2011.

[131] S. J. Park, and Y. J. Kim, "Size-Dependent Shape Evolution of Silica Nanoparticles into Hollow Structures," *Langmuir,* vol. 24, no. 21, pp. 12134-12137, 2008.

[132] Z. G. Teng, X. D. Su, Y. Y. Zheng, J. Sun, G. T. Chen, C. C. Tian, J. D. Wang, H. Li, Y. N. Zhao, and G. M. Lu, "Mesoporous Silica Hollow Spheres with

Ordered Radial Mesochannels by a Spontaneous Self-Transformation Approach," *Chem. Mater.,* vol. 25, no. 1, pp. 98-105, 2013.

[133] Z. G. Teng, S. J. Wang, X. D. Su, G. T. Chen, Y. Liu, Z. M. Luo, W. Luo, Y. X. Tang, H. X. Ju, D. Y. Zhao, and G. M. Lu, "Facile Synthesis of Yolk-Shell Structured Inorganic-Organic Hybrid Spheres with Ordered Radial Mesochannels," *Adv. Mater.,* vol. 26, no. 22, pp. 3741-3747, 2014.

[134] Y. J. Wong, L. F. Zhu, W. S. Teo, Y. W. Tan, Y. H. Yang, C. Wang, and H. Y. Chen, "Revisiting the Stober Method: In homogeneity in Silica Shells," *J. Am. Chem. Soc.,* vol. 133, no. 30, pp. 11422-11425, 2011.

[135] T. R. Zhang, J. P. Ge, Y. X. Hu, Q. Zhang, S. Aloni, and Y. D. Yin, "Formation of hollow silica colloids through a spontaneous dissolution-regrowth process," *Angew. Chem. Int. Ed.,* vol. 47, no. 31, pp. 5806-5811, 2008.

[136] Q. Y. Yu, P. P. Wang, S. Hu, J. F. Hui, J. Zhuang, and X. Wang, "Hydrothermal Synthesis of Hollow Silica Spheres under Acidic Conditions," *Langmuir,* vol. 27, no. 11, pp. 7185-7191, 2011.

[137] X. L. Huang, X. Teng, D. Chen, F. Q. Tang, and J. Q. He, "The effect of the shape of mesoporous silica nanoparticles on cellular uptake and cell function," *Biomaterials,* vol. 31, no. 3, pp. 438-448, 2010.

[138] S. Huh, J. W. Wiench, J. C. Yoo, M. Pruski, and V. S. Y. Lin, "Organic functionalization and morphology control of mesoporous silicas via a co-condensation synthesis method," *Chem. Mater.,* vol. 15, no. 22, pp. 4247-4256, 2003.

[139] X. W. Wu, and C. M. Crudden, "Chiral Hybrid Mesoporous Silicas: Assembly of Uniform Hollow Nanospheres and Helical Nanotubes with Tunable Diameters," *Chem. Mater.,* vol. 24, no. 20, pp. 3839-3846, 2012.

[140] L. F. Bi, Y. Li, S. B. Wang, Z. Y. Zhu, Y. X. Chen, Y. L. Chen, B. Z. Li, and Y. G. Yang, "Preparation and characterization of twisted periodic mesoporous ethenylene-silica nanorods," *J. Sol-Gel Sci. Tech.,* vol. 53, no. 3, pp. 619-625, 2010.

[141] S. Yang, L. Z. Zhao, C. Z. Yu, X. F. Zhou, J. W. Tang, P. Yuan, D. Y. Chen, and D. Y. Zhao, "On the origin of helical mesostructures," *J. Am. Chem. Soc.,* vol. 128, no. 32, pp. 10460-10466, 2006.

[142] P. Yuan, and X. J. Bao, "A facile and finely-controlled synthesis of versatile porous silica nanomaterials: Nanopods, helical nanorods and nanovesicles," *Mater. Lett.,* vol. 109, pp. 199-202, 2013.

[143] W. C. Huang, L. L. Chang, Y. Sakamoto, C. Y. Lin, N. C. Lai, and C. M. Yang, "Kinetically controlled formation of helical mesoporous silica nanostructures correlated to a ribbon intermediate phase," *RSC Adv.,* vol. 1, no. 2, pp. 229-237, 2011.

[144] B. G. Trewyn, C. M. Whitman, and V. S. Y. Lin, "Morphological control of room-temperature ionic liquid templated mesoporous silica nanoparticles for controlled release of antibacterial agents," *Nano Lett.,* vol. 4, no. 11, pp. 2139-2143, 2004.

[145] Y. Han, L. Zhao, and J. Y. Ying, "Entropy-driven helical mesostructure formation with achiral cationic surfactant templates," *Adv. Mater.,* vol. 19, no. 18, pp. 2454-2459, 2007.

[146] H. X. Wang, P. Van Der Voort, H. Qu, and S. Q. Liu, "A simple room-temperature synthesis of mesoporous silica rods with tunable size and porosity," *J. Nanopart. Res.,* vol. 15, no. 3, pp. 8, 2013.

[147] X. Du, and J. H. He, "Regulation role of ibuprofen toward the morphology of porous silica nanospheres during its in situ encapsulation," *J. Colloid Interface Sci.,* vol. 345, no. 2, pp. 269-277, 2010.

[148] A. M. Jakob, and T. A. Schmedake, "A novel approach to monodisperse, luminescent silica spheres," *Chem. Mater.,* vol. 18, no. 14, pp. 3173-3175, 2006.

[149] L. Wang, M. C. Estevez, M. O'Donoghue, and W. H. Tan, "Fluorophore-free luminescent organosilica nanoparticles," *Langmuir,* vol. 24, no. 5, pp. 1635-1639, 2008.

[150] C. D. S. Brites, V. T. Freitas, R. A. S. Ferreira, A. Millan, F. Palacio, and L. D. Carlos, "Metal-Free Highly Luminescent Silica Nanoparticles," *Langmuir,* vol. 28, no. 21, pp. 8190-8196, 2012.

[151] Q. J. He, and J. L. Shi, "Mesoporous silica nanoparticle based nano drug delivery systems: synthesis, controlled drug release and delivery, pharmacokinetics and biocompatibility," *J. Mater. Chem.,* vol. 21, no. 16, pp. 5845-5855, 2011.

[152] J. Lu, M. Liong, J. I. Zink, and F. Tamanoi, "Mesoporous silica nanoparticles as a delivery system for hydrophobic anticancer drugs," *Small,* vol. 3, no. 8, pp. 1341-1346, 2007.

[153] C. Y. Liu, J. Guo, W. L. Yang, J. H. Hu, C. C. Wang, and S. K. Fu, "Magnetic mesoporous silica microspheres with thermo-sensitive polymer shell for controlled drug release," *J. Mater. Chem.,* vol. 19, no. 27, pp. 4764-4770, 2009.

[154] M. H. Kim, H. K. Na, Y. K. Kim, S. R. Ryoo, H. S. Cho, K. E. Lee, H. Jeon, R. Ryoo, and D. H. Min, "Facile Synthesis of Monodispersed Mesoporous Silica Nanoparticles with Ultralarge Pores and Their Application in Gene Delivery," *ACS Nano,* vol. 5, no. 5, pp. 3568-3576, 2011.

[155] Y. S. Lin, C. P. Tsai, H. Y. Huang, C. T. Kuo, Y. Hung, D. M. Huang, Y. C. Chen, and C. Y. Mou, "Well-ordered mesoporous silica nanoparticles as cell markers," *Chem. Mater.,* vol. 17, no. 18, pp. 4570-4573, 2005.

[156] J. E. Lee, D. J. Lee, N. Lee, B. H. Kim, S. H. Choi, and T. Hyeon, "Multifunctional mesoporous silica nanocomposite nanoparticles for pH controlled drug release and dual modal imaging," *J. Mater. Chem.,* vol. 21, no. 42, pp. 16869-16872, 2011.

[157] A. M. Sauer, A. Schlossbauer, N. Ruthardt, V. Cauda, T. Bein, and C. Brauchle, "Role of Endosomal Escape for Disulfide-Based Drug Delivery from Colloidal Mesoporous Silica Evaluated by Live-Cell Imaging," *Nano Lett.,* vol. 10, no. 9, pp. 3684-3691, 2010.

[158] X. Wang, H. R. Chen, Y. Chen, M. Ma, K. Zhang, F. Q. Li, Y. Y. Zheng, D. P. Zeng, Q. Wang, and J. L. Shi, "Perfluorohexane-Encapsulated Mesoporous Silica Nanocapsules as Enhancement Agents for Highly Efficient High Intensity Focused Ultrasound (HIFU)," *Adv. Mater.,* vol. 24, no. 6, pp. 785-791, 2012.

[159] F. Wang, X. L. Chen, Z. X. Zhao, S. H. Tang, X. Q. Huang, C. H. Lin, C. B. Cai, and N. F. Zheng, "Synthesis of magnetic, fluorescent and mesoporous core-shell-structured nanoparticles for imaging, targeting and photodynamic therapy," *J. Mater. Chem.,* vol. 21, no. 30, pp. 11244-11252, 2011.

[160] M. Al Shamsi, M. T. Al Samri, S. Al-Salam, W. Conca, S. Shaban, S. Benedict, S. Tariq, A. V. Biradar, H. S. Penefsky, T. Asefa, and A. K. Souid, "Biocompatibility of Calcined Mesoporous Silica Particles with Cellular

Bioenergetics in Murine Tissues," *Chem. Res. Toxicol.,* vol. 23, no. 11, pp. 1796-1805, Nov, 2010.

[161] Z. M. Tao, B. B. Toms, J. Goodisman, and T. Asefa, "Mesoporosity and Functional Group Dependent Endocytosis and Cytotoxicity of Silica Nanomaterials," *Chem. Res. Toxicol.,* vol. 22, no. 11, pp. 1869-1880, 2009.

[162] M. A. Maurer-Jones, Y. S. Lin, and C. L. Haynes, "Functional Assessment of Metal Oxide Nanoparticle Toxicity in Immune Cells," *ACS Nano,* vol. 4, no. 6, pp. 3363-3373, 2010.

[163] Slowing, II, C. W. Wu, J. L. Vivero-Escoto, and V. S. Y. Lin, "Mesoporous Silica Nanoparticles for Reducing Hemolytic Activity Towards Mammalian Red Blood Cells," *Small,* vol. 5, no. 1, pp. 57-62, 2009.

[164] Y. N. Zhao, X. X. Sun, G. N. Zhang, B. G. Trewyn, Slowing, II, and V. S. Y. Lin, "Interaction of Mesoporous Silica Nanoparticles with Human Red Blood Cell Membranes: Size and Surface Effects," *ACS Nano,* vol. 5, no. 2, pp. 1366-1375, 2011.

[165] L. C. J. Thornassen, V. Rabolli, K. Masschaele, G. Aberto, M. Tomatis, M. Ghiazza, F. Turci, E. Breynaert, G. Martra, C. E. A. Kirschhock, J. A. Martens, D. Lison, and B. Fubini, "Model System to Study the Influence of Aggregation on the Hemolytic Potential of Silica Nanoparticles," *Chem. Res. Toxicol.,* vol. 24, no. 11, pp. 1869-1875, 2011.

[166] T. Yu, A. Malugin, and H. Ghandehari, "Impact of Silica Nanoparticle Design on Cellular Toxicity and Hemolytic Activity," *ACS Nano,* vol. 5, no. 7, pp. 5717-5728, 2011.

[167] H. B. Alam, Z. Chen, A. Jaskille, R. Querol, E. Koustova, R. Inocencio, R. Conran, A. Seufert, N. Ariaban, K. Toruno, and P. Rhee, "Application of a zeolite hemostatic agent achieves 100% survival in a lethal model of complex groin injury in swine," *J. Trauma,* vol. 56, no. 5, pp. 974-983, 2004.

[168] T. A. Ostomel, Q. H. Shi, and G. D. Stucky, "Oxide hemostatic activity," *J. Am. Chem. Soc.,* vol. 128, no. 26, pp. 8384-8385, Jul, 2006.

[169] C. L. Dai, Y. Yuan, C. S. Liu, J. Wei, H. Hong, X. S. Li, and X. H. Pan, "Degradable, antibacterial silver exchanged mesoporous silica spheres for hemorrhage control," *Biomaterials,* vol. 30, no. 29, pp. 5364-5375, 2009.

[170] M. A. Dobrovolskaia, P. Aggarwal, J. B. Hall, and S. E. McNeil, "Preclinical studies to understand nanoparticle interaction with the immune system and its potential effects on nanoparticle biodistribution," *Mol. Pharm.,* vol. 5, no. 4, pp. 487-495, 2008.

[171] M. Cavadas, A. Gonzalez-Fernandez, and R. Franco, "Pathogen-mimetic stealth nanocarriers for drug delivery: a future possibility," *Nanomedicine,* vol. 7, no. 6, pp. 730-743, Dec, 2011.

[172] J. M. Koziara, J. J. Oh, W. S. Akers, S. P. Ferraris, and R. J. Mumper, "Blood compatibility of cetyl alcohol/polysorbate-based nanoparticles," *Pharm. Res.,* vol. 22, no. 11, pp. 1821-1828, 2005.

[173] P. Aggarwal, J. B. Hall, C. B. McLeland, M. A. Dobrovolskaia, and S. E. McNeil, "Nanoparticle interaction with plasma proteins as it relates to particle biodistribution, biocompatibility and therapeutic efficacy," *Adv. Drug Delivery Rev.,* vol. 61, no. 6, pp. 428-437, 2009.

[174] D. E. Owens, and N. A. Peppas, "Opsonization, biodistribution, and pharmacokinetics of polymeric nanoparticles," *Int. J. Pharm.,* vol. 307, no. 1, pp. 93-102, 2006.

[175] H. X. Wu, S. J. Zhang, J. M. Zhang, G. Liu, J. L. Shi, L. X. Zhang, X. Z. Cui, M. L. Ruan, Q. J. He, and W. B. Bu, "A Hollow-Core, Magnetic, and Mesoporous Double-Shell Nanostructure: In Situ Decomposition/Reduction Synthesis, Bioimaging, and Drug-Delivery Properties," *Adv. Funct. Mater.,* vol. 21, no. 10, pp. 1850-1862, 2011.

[176] F. Lu, S. H. Wu, Y. Hung, and C. Y. Mou, "Size Effect on Cell Uptake in Well-Suspended, Uniform Mesoporous Silica Nanoparticles," *Small,* vol. 5, no. 12, pp. 1408-1413, 2009.

[177] B. S. Chang, J. Guo, C. Y. Liu, J. Qian, and W. L. Yang, "Surface functionalization of magnetic mesoporous silica nanoparticles for controlled drug release," *J. Mater. Chem.,* vol. 20, no. 44, pp. 9941-9947, 2010.

[178] Q. J. He, J. L. Shi, X. Z. Cui, J. J. Zhao, Y. Chen, and J. Zhou, "Rhodamine B-co-condensed spherical SBA-15 nanoparticles: facile co-condensation synthesis and excellent fluorescence features," *J. Mater. Chem.,* vol. 19, no. 21, pp. 3395-3403, 2009.

[179] C. Boissiere, M. A. U. Martines, M. Tokumoto, A. Larbot, and E. Prouzet, "Mechanisms of pore size control in MSU-X mesoporous silica," *Chem. Mater.,* vol. 15, no. 2, pp. 509-515, 2003.

[180] M. A. Dobrovoiskaia, J. D. Clogston, B. W. Neun, J. B. Hall, A. K. Patri, and S. E. McNeil, "Method for analysis of nanoparticle hemolytic properties in vitro," *Nano Lett.,* vol. 8, no. 8, pp. 2180-2187, 2008.

[181] F. Y. Tong, X. Q. Chen, L. B. Chen, P. Y. Zhu, J. F. Luan, C. Mao, J. C. Bao, and J. Shen, "Preparation, blood compatibility and anticoagulant effect of heparin-loaded polyurethane microspheres," *J. Mater. Chem. B,* vol. 1, no. 4, pp. 447-453, 2013.

[182] T. Ishida, H. Harashima, and H. Kiwada, "Interactions of liposomes with cells in vitro and in vivo: Opsonins and receptors," *Curr. Drug Metab.,* vol. 2, no. 4, pp. 397-409, 2001.

[183] Y. Roiter, M. Ornatska, A. R. Rammohan, J. Balakrishnan, D. R. Heine, and S. Minko, "Interaction of nanoparticles with lipid membrane," *Nano Lett.,* vol. 8, no. 3, pp. 941-944, 2008.

[184] J. Shi, Y. Hedberg, M. Lundin, I. O. Wallinder, H. L. Karlsson, and L. Moller, "Hemolytic properties of synthetic nano- and porous silica particles: The effect of surface properties and the protection by the plasma corona," *Acta Biomater.,* vol. 8, no. 9, pp. 3478-3490, 2012.

[185] M. Deserno, and W. M. Gelbart, "Adhesion and wrapping in colloid-vesicle complexes," *J. Phys. Chem. B,* vol. 106, no. 21, pp. 5543-5552, 2002.

[186] X. X. He, H. L. Nie, K. M. Wang, W. H. Tan, X. Wu, and P. F. Zhang, "In Vivo Study of Biodistribution and Urinary Excretion of Surface-Modified Silica Nanoparticles," *Anal. Chem.,* vol. 80, no. 24, pp. 9597-9603, 2008.

[187] T. Cedervall, I. Lynch, S. Lindman, T. Berggard, E. Thulin, H. Nilsson, K. A. Dawson, and S. Linse, "Understanding the nanoparticle-protein corona using methods to quantify exchange rates and affinities of proteins for nanoparticles," *Proc. Natl. Acad. Sci. U. S. A.,* vol. 104, no. 7, pp. 2050-2055, 2007.

[188] M. Lundqvist, J. Stigler, T. Cedervall, T. Berggard, M. B. Flanagan, I. Lynch, G. Elia, and K. Dawson, "The Evolution of the Protein Corona around Nanoparticles: A Test Study," *ACS Nano,* vol. 5, no. 9, pp. 7503-7509, 2011.

[189] E. Casals, T. Pfaller, A. Duschl, G. J. Oostingh, and V. Puntes, "Time Evolution of the Nanoparticle Protein Corona," *ACS Nano,* vol. 4, no. 7, pp. 3623-3632, 2010.

[190] S. I. Jeon, J. H. Lee, J. D. Andrade, and P. G. Degennes, "Protein surface interactions in the presence of polyethylene oxide. I. Simplified theory," *J. Colloid Interface Sci.,* vol. 142, no. 1, pp. 149-158, 1991.

[191] Y. H. Lin, C. E. Chen, C. Y. Wang, F. Pu, J. S. Ren, and X. G. Qu, "Silver nanoprobe for sensitive and selective colorimetric detection of dopamine via robust Ag-catechol interaction," *Chem. Commun.,* vol. 47, no. 4, pp. 1181-1183, 2011.

[192] X. Ji, G. Palui, T. Avellini, H. B. Na, C. Y. Yi, K. L. Knappenberger, and H. Mattoussi, "On the pH-Dependent Quenching of Quantum Dot Photoluminescence by Redox Active Dopamine," *J. Am. Chem. Soc.,* vol. 134, no. 13, pp. 6006-6017, 2012.

[193] R. M. Wightman, L. J. May, and A. C. Michael, "Detection of dopamine dynamics in the brain," *Anal. Chem.,* vol. 60, no. 13, pp. A769-&, Jul, 1988.

[194] B. R. Li, Y. J. Hsieh, Y. X. Chen, Y. T. Chung, C. Y. Pan, and Y. T. Chen, "An Ultrasensitive Nanowire-Transistor Biosensor for Detecting Dopamine Release from Living PC12 Cells under Hypoxic Stimulation," *J. Am. Chem. Soc.,* vol. 135, no. 43, pp. 16034-16037, 2013.

[195] Y. Tao, Y. H. Lin, J. S. Ren, and X. G. Qu, "A dual fluorometric and colorimetric sensor for dopamine based on BSA-stabilized Au nanoclusters," *Biosens. Bioelectron.,* vol. 42, pp. 41-46, 2013.

[196] M. Nichkova, P. M. Wynveen, D. T. Marc, H. Huisman, and G. H. Kellermann, "Validation of an ELISA for urinary dopamine: applications in monitoring treatment of dopamine-related disorders," *J. Neurochem.,* vol. 125, no. 5, pp. 724-735, 2013.

[197] F. Malem, and D. Mandler, "Self-Assembled Monolayers in Electroanalytical Chemistry - Application of Omega-Mercapto Carboxylic-Acid Monolayers for the Electrochemical Detection of Dopamine in the Presence of a High-Concentration of Ascorbic-Acid," *Anal. Chem.,* vol. 65, no. 1, pp. 37-41, 1993.

[198] T. Qian, S. S. Wu, and J. Shen, "Facilely prepared polypyrrole-reduced graphite oxide core-shell microspheres with high dispersibility for electrochemical detection of dopamine," *Chem. Commun.,* vol. 49, no. 41, pp. 4610-4612, 2013.

[199] W. C. Wu, H. W. Chang, and Y. C. Tsai, "Electrocatalytic detection of dopamine in the presence of ascorbic acid and uric acid at silicon carbide coated electrodes," *Chem. Commun.,* vol. 47, no. 22, pp. 6458-6460, 2011.

[200] H. Wang, H. Jin, and H. S. Zhang, "Determination of catecholamines as their N-hydroxy-succinimidyl-3-indolylacetate derivatives by pre-column derivatization HPLC separation and fluorescent detection," *Fresenius J. Anal. Chem.,* vol. 365, no. 8, pp. 682-684, 1999.

[201] Z. D. Peterson, D. C. Collins, C. R. Bowerbank, M. L. Lee, and S. W. Graves, "Determination of catecholamines and metanephrines in urine by capillary electrophoresis-electrospray ionization-time-of-fight mass spectrometry," *J. Chromatogr., B: Anal. Technol. Biomed. Life Sci.,* vol. 776, no. 2, pp. 221-229, 2002.

[202] Y. Mao, Y. Bao, D. X. Han, F. H. Li, and L. Niu, "Efficient one-pot synthesis of molecularly imprinted silica nanospheres embedded carbon dots for fluorescent dopamine optosensing," *Biosens. Bioelectron.,* vol. 38, no. 1, pp. 55-60, 2012.

[203] K. G. Qu, J. S. Wang, J. S. Ren, and X. G. Qu, "Carbon Dots Prepared by Hydrothermal Treatment of Dopamine as an Effective Fluorescent Sensing Platform for the Label-Free Detection of Iron(III) Ions and Dopamine," *Chem. Eur. J.,* vol. 19, no. 22, pp. 7243-7249, 2013.

[204] J. L. Chen, X. P. Yan, K. Meng, and S. F. Wang, "Graphene Oxide Based Photoinduced Charge Transfer Label-Free Near-Infrared Fluorescent Biosensor for Dopamine," *Anal. Chem.,* vol. 83, no. 22, pp. 8787-8793, 2011.

[205] Q. Xu, and J. Yoon, "Visual detection of dopamine and monitoring tyrosinase activity using a pyrocatechol violet-Sn^{4+} complex," *Chem. Commun.,* vol. 47, no. 46, pp. 12497-12499, 2011.

[206] Q. Mu, H. Xu, Y. Li, S. J. Ma, and X. H. Zhong, "Adenosine capped QDs based fluorescent sensor for detection of dopamine with high selectivity and sensitivity," *Analyst,* vol. 139, no. 1, pp. 93-98, 2014.

[207] R. Baron, M. Zayats, and I. Willner, "Dopamine-, L-DOPA-, adrenaline-, and noradrenaline-induced growth of Au nanoparticles: Assays for the detection of neurotransmitters and of tyrosinase activity," *Anal. Chem.,* vol. 77, no. 6, pp. 1566-1571, 2005.

[208] J. J. B. Nevado, J. M. L. Gallego, and P. B. Laguna, "Flow-injection spectrophotometric determination of adrenaline and dopamine with sodium hydroxide," *J. Pharm. Biomed. Anal.,* vol. 14, no. 5, pp. 571-577, 1996.

[209] J. J. Berzas, J. M. Lemus, and P. Buitrago, "Stopped-flow spectrophotometric determination of dopamine and methyldopa with sodium hydroxide," *Anal. Lett.,* vol. 30, no. 6, pp. 1109-1120, 1997.

[210] I. C. Vieira, and O. Fatibello, "Spectrophotometric determination of methyldopa and dopamine in pharmaceutical formulations using a crude extract of sweet potato root (Ipomoea batatas (L.) Lam.) as enzymatic source," *Talanta,* vol. 46, no. 4, pp. 559-564, 1998.

[211] A. Abbaspour, A. Khajehzadeh, and A. Ghaffarinejad, "A simple and cost-effective method, as an appropriate alternative for visible spectrophotometry: development of a dopamine biosensor," *Analyst,* vol. 134, no. 8, pp. 1692-1698, 2009.

[212] A. Abbaspour, H. Valizadeh, and A. Khajehzadeh, "A simple, fast and cost effective method for detection and determination of dopamine in bovine serum," *Anal. Methods,* vol. 3, no. 6, pp. 1405-1409, 2011.

[213] H. Lee, S. M. Dellatore, W. M. Miller, and P. B. Messersmith, "Mussel-inspired surface chemistry for multifunctional coatings," *Science,* vol. 318, no. 5849, pp. 426-430, Oct, 2007.

[214] Q. Wei, F. L. Zhang, J. Li, B. J. Li, and C. S. Zhao, "Oxidant-induced dopamine polymerization for multifunctional coatings," *Polym. Chem.,* vol. 1, no. 9, pp. 1430-1433, 2010.

[215] S. Hong, Y. S. Na, S. Choi, I. T. Song, W. Y. Kim, and H. Lee, "Non-Covalent Self-Assembly and Covalent Polymerization Co-Contribute to Polydopamine Formation," *Adv. Funct. Mater.,* vol. 22, no. 22, pp. 4711-4717, 2012.

[216] N. F. Della Vecchia, R. Avolio, M. Alfe, M. E. Errico, A. Napolitano, and M. d'Ischia, "Building-Block Diversity in Polydopamine Underpins a

Multifunctional Eumelanin-Type Platform Tunable Through a Quinone Control Point," *Adv. Funct. Mater.,* vol. 23, no. 10, pp. 1331-1340, 2013.

[217] P. Meredith, B. J. Powell, J. Riesz, S. P. Nighswander-Rempel, M. R. Pederson, and E. G. Moore, "Towards structure-property-function relationships for eumelanin," *Soft Matter,* vol. 2, no. 1, pp. 37-44, 2006.

[218] S. P. Nighswander-Rempel, J. Riesz, J. Gilmore, and P. Meredith, "A quantum yield map for synthetic eumelanin," *J. Chem. Phys.,* vol. 123, no. 19, pp. 6, 2005.

[219] S. Olsen, J. Riesz, I. Mahadevan, A. Coutts, J. P. Bothma, B. J. Powell, R. H. McKenzie, S. C. Smith, and P. Meredith, "Convergent proton-transfer photocycles violate mirror-image symmetry in a key melanin monomer," *J. Am. Chem. Soc.,* vol. 129, no. 21, pp. 6672-6673, 2007.

[220] X. Y. Zhang, S. Q. Wang, L. X. Xu, L. Feng, Y. Ji, L. Tao, S. X. Li, and Y. Wei, "Biocompatible polydopamine fluorescent organic nanoparticles: facile preparation and cell imaging," *Nanoscale,* vol. 4, no. 18, pp. 5581-5584, 2012.

[221] D. R. Dreyer, D. J. Miller, B. D. Freeman, D. R. Paul, and C. W. Bielawski, "Elucidating the Structure of Poly(dopamine)," *Langmuir,* vol. 28, no. 15, pp. 6428-6435, 2012.